ABSTRACT

XU, LIBAI. **Prompt Gamma-ray Imaging for Small Animals.** (Under the direction of Professor Robin P. Gardner.)

Small animal imaging is recognized as a powerful discovery tool for small animal modeling of human diseases, which is providing an important clue to complete understanding of disease mechanisms and is helping researchers develop and test new treatments. The current small animal imaging techniques include positron emission tomography (PET), single photon emission tomography (SPECT), computed tomography (CT), magnetic resonance imaging (MRI), and ultrasound (US).

A new imaging modality called prompt gamma-ray imaging (PGI) has been identified and investigated primarily by Monte Carlo simulation. Currently it is suggested for use on small animals. This new technique could greatly enhance and extend the present capabilities of PET and SPECT imaging from ingested radioisotopes to the imaging of selected non-radioactive elements, such as Gd, Cd, Hg, and B, and has the great potential to be used in Neutron Cancer Therapy to monitor neutron distribution and neutron-capture agent distribution. This approach consists of irradiating small animals in the thermal neutron beam of a nuclear reactor to produce prompt gamma rays from the elements in the sample by the radiative capture (n, γ) reaction. These prompt gamma rays are emitted in energies that are characteristic of each element and they are also produced in characteristic coincident chains. After measuring these prompt gamma rays by surrounding spectrometry array, the distribution of each element of interest in the sample is reconstructed from the mapping of

each detected signature gamma ray by either electronic collimations or mechanical collimations. In addition, the transmitted neutrons from the beam can be simultaneously used for very sensitive anatomical imaging, which provides the registration for the elemental distributions obtained from PGI.

The primary approach is to use Monte Carlo simulation methods either with the specific purpose code CEARCPG, developed at NC State University or with the general purpose codes GEANT4 or MCNP5, to predict results and investigate the feasibility of this new imaging idea. Benchmark experiments have been conducted to test the capability of the code to simulate prompt gamma rays, which are produced by following the nuclear structures of each irradiated isotope, and coincidence counting techniques, which are considered the most important improvement in neutron-related gamma-ray detection applications to reduce gamma background and improve system signal-to-noise ratios. With coincidence prompt gamma rays available, two major imaging techniques, electronic collimations and mechanic collimations, are implemented in the simulation to illustrate the feasibility of imaging elemental distribution by this new technique. The expectation maximization algorithm is employed in electronic collimation to reconstruct images. The common SPECT imaging algorithms are used in mechanical collimation to get an image. Several critical topics concerning practical applications have already been discussed, such as the radiation dose to the mouse and the detection efficiency of high-energy gamma rays.

The funding of this work is provided by the Center for Engineering Application of Radioisotopes (CEAR) at North Carolina State University (NCSU) and Nuclear Engineering Education Research.

Prompt Gamma-ray Imaging for Small Animals

By

Libai Xu

A dissertation submitted to the Graduate Faculty of
North Carolina State University
in partial fulfillment of the
requirements for the Degree of
Doctor of Philosophy

Nuclear Engineering

Raleigh, North Carolina

2006

Approved by:

Dr. Dmitriy Y. Anistratov	**Dr. Avneet Sood**
Prof. Wesley E. Snyder	**Prof. Robin P. Gardner, Chair**

BIOGRAPHY

Libai Xu was born in China on July 12, 1977. He is the second son of Mr. Wenfa Xu and Mrs. Caixing Yang.

Libai received his Bachelor's Degree in Engineering Physics in 1999 and his Master's Degree in Engineering Physics under the guidance of Prof. Yuanjing Li in 2002 from Tsinghua University, China.

In 2002, he began his graduate study in the Nuclear Engineering Department at North Carolina State University and worked as a research assistant under Prof. Gardner's advisory.

Libai married with Hui Zhi in 2002.

ACKNOWLEDGEMENTS

First of all, I would like to express my deepest appreciation to Pref. Robin P. Gardner, chairman of my Advisory Committee for his invaluable guidance and financial support throughout this work. The remaining members of his Advisory Committee, Prof. Wesley E. Snyder, Dr. Avneet Sood, and Dr. Dmitriy Y. Anistratov, are also highly appreciated for their comments and suggestion.

To all of his colleagues, the author would like to express his warmest thanks, with special thanks to Dr. Weijun Guo and Dr. Xiaogang Han.

Finally, the author dedicated this dissertation to his parents, Wenfa Xu, Caixing Yang, and his lovely wife Hui Zhi.

TABLE OF CONTENTS

List of Figures

List of tables

1. Introduction

1.1 Overview

Prompt gamma rays are emitted during a neutron capture reaction, which is the dominant neutron process in a low energy range. Once an incident neutron is absorbed by the target nucleus, a new compound nucleus is formed in an excited state, and will almost instantaneously de-excite to a stable energy level by emitting one or more prompt gamma rays. These prompt gamma rays are in energies that are characteristic of the target nucleus, and can be detected to identify elements when gamma-ray spectrometry is used. This approach is called prompt gamma-ray neutron activation analysis (PGNAA). In many cases, this new configuration also yields a radioactive nucleus, which also de-excites by emitting one or more characteristic delayed gamma rays in a rate according to the unique half-life of the radioactive nucleus. The technique of measuring these delayed gamma rays is called delayed gamma-ray neutron activation analysis (DGNAA). PGNAA and DGNAA are referred to as neutron activation analysis (NAA). DGNAA is more common in practice. Thus, when NAA is mentioned, it is always assumed that the delayed gamma-ray neutron activation analysis is taken. All of these instances are illustrated in figure 1-1 (Glascock 1984).

Since the discovery of neutron activation analysis by Hevesy and Levi in 1936, NAA has become a very sensitive analytical technique for both qualitative and quantitative elemental analysis for major, minor, and trace elements in samples from almost every

conceivable field of scientific or technical interest. Many reviews and papers have been published on NAA and its applications (Greenwood, 1979; Anderson, 1982; Lindstrom, 1994, 1997; Paul, 2000), and two extensive bibliographies have also been compiled (Gladney, 1979; Glascock, 1984).

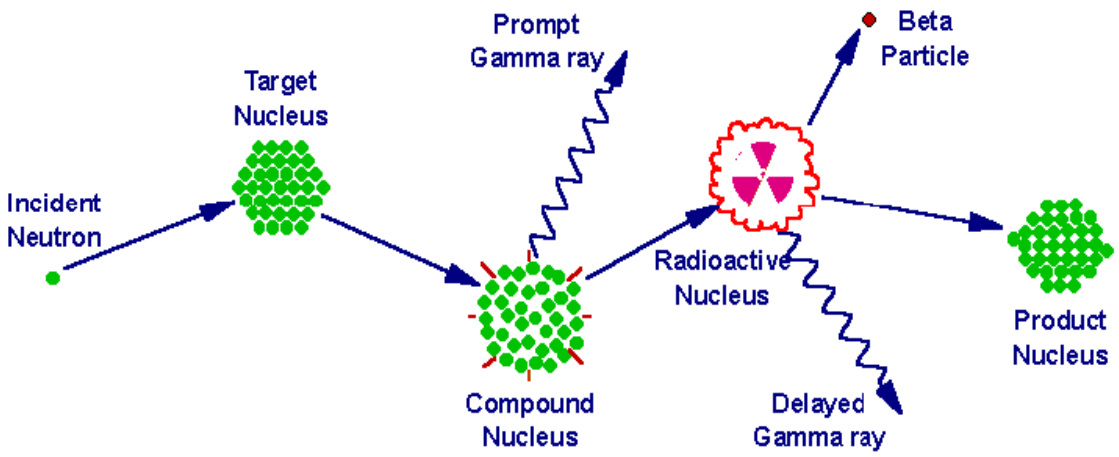

Fig. 1-1 Physics of Neutron Activation Analysis

Elemental composition of sample is obtained through neutron activation analysis. However, in certain cases, elemental distribution is also preferred. Some efforts have been taken to employ imaging techniques with NAA to get elemental distribution. Neutron induced gamma-ray emission tomography (Balogun, 1996) was implemented to capture the image of sodium distribution in a pellet of freeze-dried sea water and a section of human bone using the gamma-ray emitted by Na-24 produced in the presence of a number of other gamma-ray emitting nuclides. Prompt gamma rays from boron were detected for on-line

measurements of boron concentrations, called gamma-ray telescope (Verbakel, 1997, 2001, 2002), for boron neutron capture therapy (BNCT), where the effectiveness of NCT depended both on the distribution of the capturing agent (boron or gadolinium) and the distribution of thermal neutrons in the tissue.

Recently, small animal imaging has been recognized as a powerful discovery tool for small animal modeling of human diseases, which is providing important clues to a complete understanding of the disease mechanism and to develop and test new treatments.

In this thesis, a novel imaging approach has been proposed for small animals (mice) and investigated primarily by Monte Carlo simulation. The new approach is called prompt gamma-ray imaging or PGI (Gardner & Xu, 2003), as can be seen in figure 1-2. This approach could greatly enhance and extend the present capabilities of small animal imaging by position emission tomography (PET) and single photon emission tomography (SPECT) from ingested radioisotopes to include the imaging of selected non-radioactive elements such as Gd, Cd, Hg, and B. This approach consists of irradiating small animals in the thermal neutron beam of a nuclear reactor to produce prompt gamma rays from the elements in the sample by the radiative capture (n, γ) reaction. These prompt gamma rays are emitted in coincidence in pairs, triplets, or cascades that are more than sum to the Q value of the nuclear reaction for the element of interest. They can be detected with multiple detectors operating in the coincidence counting mode. This coincidence feature reduces the background or noise problem significantly (as in the case of PET imaging). These prompt gamma rays are also in energies ranges that are characteristic of each element, also reducing

noise levels (as is the case in SPECT imaging) when gamma-ray spectrometry is used. Therefore, they can be used for imaging by using the combined principles used in PET and SPECT imaging. Additionally, the transmitted neutrons from the source can be simultaneously used for very sensitive structure imaging, which provides the registration that is desired in PET and SPECT,and must be obtained by a separate computed tomography (CT) or magnetic resonance imaging (MRI) scanning device.

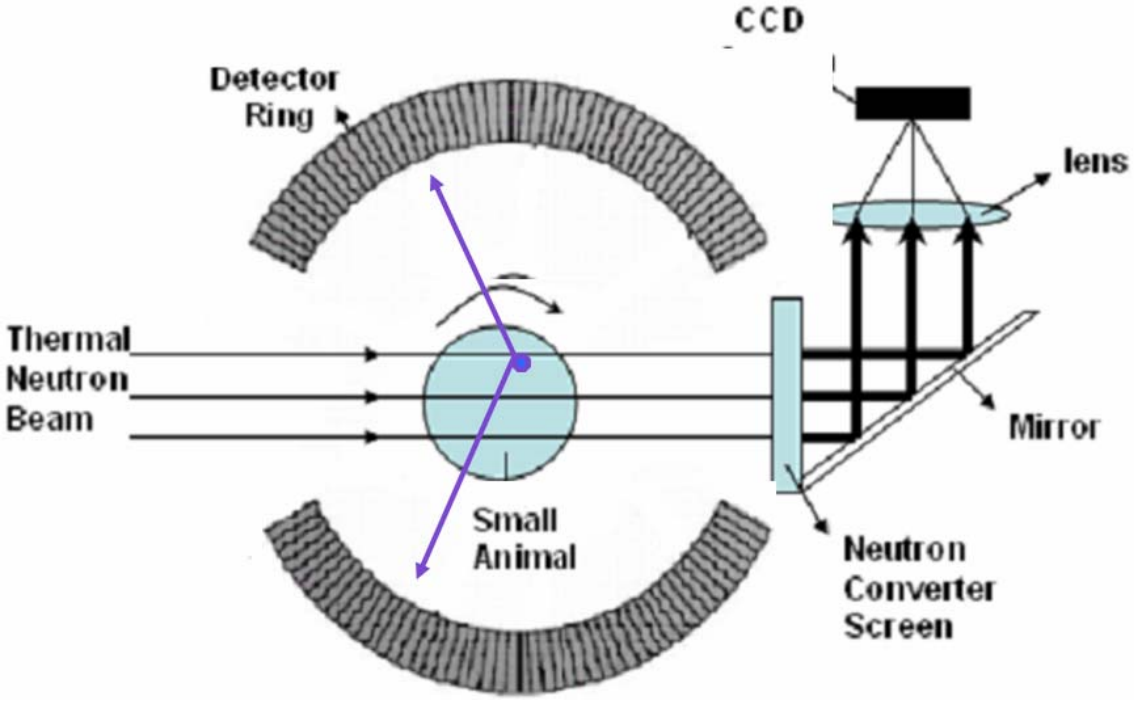

Fig. 1-2 Schematic Diagram of Prompt Gamma-ray Imaging

The primary approach will be to use Monte Carlo simulation methods either with the specific purpose code CEARCPG, developed at NC State University, or with the general purpose codes GEANT4 or MCNP5, to predict possible experimental results and investigate the feasibility of this new imaging idea. Benchmark experiments have been conducted to test

the capability of the code to simulate prompt gamma rays, which are produced by following the nuclear structures of each irradiated isotope, and that of coincidence counting techniques, which are considered the most important improvement in neutron-related gamma detection applications to reduce gamma background and improve system signal noise ratios. With coincidence prompt gamma rays available, two major imaging techniques, by using electronic collimations and mechanic collimations, are implemented in the simulation to illustrate the feasibility of imaging elemental distribution by this new technique. The expectation maximization algorithm is employed in the imaging method involving electronic collimations to reconstruct images. The common SPECT imaging algorithms are used in the imaging method involving mechanical collimations to get an image.

Several critical questions concerning practical applications are investigated and discussed, such as the radiation dose for the mouse and the detection efficiency of high-energy gamma rays.

1.2 Review of small animal imaging

Small animal imaging is becoming recognized as a powerful discovery tool for small animal modeling of human diseases, which is providing important clues to a complete understanding of disease mechanisms and is helping researchers to develop and test new treatments. Compared with the traditional experimental method of small animal modeling of human diseases, which sacrifices a large number of small animals to perform tissue or molecule analysis at multiple points, imaging techniques are totally non-invasive methods

and allow for the study of one animal for the entire process *in vivo*, which might include tumor initiation, growth, treatment, and repetition in the same animal. The traditional experimental method prevents longitudinal studies, which is an enormous disadvantage when it comes to monitoring the effects of therapy or studying developmental issues. These experiments are always time-consuming, labor intensive, and therefore quite expensive. On the contrary, imaging techniques would provide a complete set of data from every animal, greatly reducing the number of sacrificed animals, reducing the complexity and cost of the experiments, offering better control of the experiments, and improving data quality.

Five imaging modalities (Johnson & Turnbull, 1999) have been identified for use in small animal imaging. These modalities are X-ray computed tomography (XCT), magnetic resonance imaging (MRI), positron emission tomography (PET), single photon emission computed tomography (SPECT), and ultrasound (US). In XCT, a signal arises from the differences in the attenuation coefficients of X-rays' interaction with matter. PET and SPECT detect gamma rays emitted during the decay of specific radionuclides that are deliberately introduced into small animals. The activity distribution is reconstructed from the detected gamma rays. Ultrasound uses the scatter and temporal-spatial differences caused by acoustic interfaces for the detection of abnormalities in a living tissue. Magnetic resonance imaging uses the differences in the relaxivity of proton spin frequencies in water, fat, and other macromolecules within living tissues for their superb anatomic detail. All of these imaging technologies are used for both human beings and small animals. To distinguish them from the imaging techniques used for human beings, small animal imaging technologies are named with a prefix "Micro-", such as Micro-CT, Micro-PET, Micro-SPECT, and so on.

Most of these Micro systems are now commercially available. Micro-CT has a spatial resolution of less than 100μm. The major application of Micro-CT today has been in quantifying the density and architecture of bones (Genant, 1999), but there are rapidly growing applications in vascular studies (Lerman & Ritman, 1999) and in the characterization of the phenotype of transgenic (Graichen, 1998) and knockout animal models (Montero, 2000) during preclinical investigations. MR microscopy provides the advantages of excellent soft-tissue contrast and spatial resolution ranging from 50–100μm (Wehrli, 1998). MR microscopy has also been applied to the study of bones (Hipp, 1996) and cartilage (Xia, 1994), and in the determination of anatomic phenotypes in small animals (Benveniste, 2000).

Micro-PET systems can provide information on the functions of living organisms, using positron-emitting labels that attach to specific molecular targets (Kornblum, 2000). Micro-PET is practically limited in its spatial resolution to ~1.5–2 mm, owing to a combination of intrinsic factors and the finite range of the positron (Tal, 2001). Similar to Micro-PET systems, Micro-SPECT systems can also provide the functional information of living organisms, but with a higher spatial resolution of less than 1mm (Paul & Hank, 2003), which is mainly limited by the geometric effect of the collimator. Compared to Micro-PET systems, Micro-SPECT systems have a lower sensitivity, which requires more radioactivities to be injected. Several investigations have been made to improve the Micro-SPECT system's sensitivity by using multiple-pinhole and coded-aperture techniques (Chang, 1974). Ultrasound microscopy, implemented with high-frequency (40–60 MHz) transducers, can

also provide 50 μm resolution with the added benefit of real-time imaging capabilities (Foster, 2000). Ultrasound microscopy is particularly suited to the investigation of mouse embryonic development and image-guided manipulation *in vivo* (Turnbull, 1999).

Each technique described above provides unique information that is often complementary with other approaches. Generally speaking, CT, MRI, and US provide anatomical information; PET and SPECT provide functional information. Recently, a great deal of effort have been made to combine these imaging modalities, such as combining PET with CT (Wechalekar et al., 2005; Cesca et al., 2004), PET with MRI (Cho, 2005), and SPECT with CT (Pietrzyk et al., 1996; Guerra et al., 2003; Weisenberger et al., 2003), to acquire both anatomical and functional information for the same object.

PGI is a novel imaging modality for small animals, which allows researchers to get both anatomical and functional information simultaneously. The anatomical information is acquired from transmitted neutrons by neutron tomography. The functional information is acquired from detected prompt gamma rays, using GNAA and the combined principles of PET and SPECT imaging.

1.3 Review of *in vivo* neutron applications

A neutron is an electrically neutral particle, and based on its energy, it can be divided into several groups: cold neutron, thermal neutron, epithermal neutron, and fast neutron. Neutrons have been widely used in industrial applications for decades due to their special

attenuation law with matters. The advantage of neutrons over X-rays is their higher interaction probability with hydrogen and lower attenuation in several heavy elements which are “black” for X-rays (e.g., lead, bismuth, uranium). This makes neutron imaging suitable for some applications where X-ray imaging fails, even if neutron imaging is more expensive and demanding. The current applications of neutron imaging can be found in several review papers (Bayon, 1999; Mishima et al., 1999; Kardjilov, 2005). Researchers attempted to apply neutron imaging to the human body so that it would create a better soft tissue contrast (Adani & Fallone, 2000). However, the main problem with neutron imaging in relation to the human body is that the neutron attenuation coefficient with hydrogen is too high, so almost no neutrons can penetrate the human body; meanwhile, scattered neutrons from hydrogen are very intense.

Neutron-induced reactions are capable of indicating the characteristics of atoms, and are therefore widely used in elemental analysis in both industrial and medical applications. *In vivo* neutron activation analysis is the most typical neutron application method in most medical fields.

The potential of *in vivo* neutron activation analysis was first highlighted by Anderson and his colleagues (1964). They irradiated two subjects with fast neutrons for ten minutes. Fifteen minutes after irradiation, whole-body counts were taken and compared with those obtained from a phantom with a known quantity of sodium and chlorine. Then the content in the two subjects was determined relative to the phantom. After the beginning of the *in vivo* application, a lot of researchers and centers around the world became devoted to this field, and quickly extended the applications from using fast neutrons to using thermal neutrons,

from inelastic reactions to capture reactions, and from monitoring the delayed radioactive decay gamma rays to monitoring prompt gamma rays. Currently, *in vivo* neutron activation analysis has been widely applied to medical diagnosis and clinical research and has created new insight into the elemental composition of the human body.

The absolute measurement of some environmental contaminants such as Cd, Hg, and Si in human organs requires a partial body scan, while the measurements of vital constituents such as N, P, and Ca in either the entire body or a body part requires a whole body scan. Nitrogen levels are measured to analyze a patient's protein status in many nutritional disorders and diseased states (Biggin, 1972; O'Meara, 2001). Calcium, normally located in the skeleton, is measured to provide a direct examination of the total skeleton mass (Nicoll et al., 1987; Evans et al., 1979). Phosphorus is measured to provide data for the design of dialysis therapy. Total body chlorine is measured to estimate the extracellular space (Ma, 1998; Mitra et al., 1993; Beddoe, 1987). Total body carbon is measured to estimate body fat (Sutcliffe, 1990). The over exposure of manganese in the human brain, which may cause central nervous system damage, is being investigated (Arnold, 2000). Aluminum, one cause of bone disease and osteomalacia, is measured in the hand bone (Byun, 2005). Cadmium content in the liver and kidneys is also being studied (Grinyer, 2005; Franklin, 1990). The detection limit of Cd in the kidney is 1.7mg. The detection limit of Cd in the liver is 3.3ppm.

Neutron Capture Therapy is a cancer therapy modality, more specifically, brain tumors, in which most of the radiation dose absorbed by the tumor is generated on a cellular level by the reaction of a tumor selective agent with thermal neutrons (Coderre & Morris,

1999). NCT is under clinical evaluation with ^{10}B (BNCT). Boron Neutron Capture Therapy (BNCT) is based on the emission of two high linear-energy-transfer particles after thermal neutron capture in ^{10}B. These two particles, an α-particle of 1.5 Mev and a recoiling ^{7}Li-nucleus of 0.85 Mev, which are emitted in an excited state in the tissue, have a range of the order of 10μm. As their energy is almost totally deposited within one cell, they give rise to closely spaced ionizing events, resulting in the destruction of that cell. During motion, 93% of the Li-particle decays to the ground state, releasing a photon of energy 478 kev. Gadolinium is another possible agent for NCT. The current status of NCT is reviewed by Barth et al. 2005.

1.4 Review of neutron-induced gamma-ray imaging

Although neutron-induced gamma rays have been widely used in neutron activation analysis, most of these applications are focused on the quantitative analysis of elemental composition, but not on the imaging of elemental distribution. However, in certain cases, elemental distribution is required. Neutron-induced gamma-ray emission tomography (Balogun, 1996) was implemented to capture the image of the distribution of sodium in a pellet of freeze-dried sea water and a section of human bone using the gamma rays emitted by Na-24, which was produced in the presence of a number of other gamma-ray emitting nuclides. A gamma-ray telescope (Verbakel et al., 1997, 2001, 2002; Barker & Maier, 2005) was proposed to be used in boron neutron capture therapy. In BNCT, the $^{10}B(n,a)^{7}Li$ reaction is used to create a tumor-destructing field of high linear energy transfer particles. The therapy

requires a high boron concentration in the tumor and a low boron concentration in the healthy tissue. The Boron Neutron Capture Reaction is accompanied by the emission of a prompt gamma ray of energy, 478kev. These prompt gamma rays are measured by one collimated detector scanning the object's region to analyze the boron distribution; meanwhile, prompt gamma rays from hydrogen are measured to derive the neutron distribution. The preliminary results of the one-dimension distribution of boron concentration and neutron distribution have been reported. The resolution is around 1.5cm for the human brain.

2. RADIOGRAPHY AND TOMOGRAPHY

2.1 Introduction:

Radiography and tomography are referred to as imaging. X-ray imaging and neutron imaging are the most popular imaging technologies used to inspect the internal properties of objects. They have been widely used in industrial applications for decades and have proved themselves as very useful nondestructive testing techniques. For example, X-ray and neutrons imaging are used to study bulk-rock samples (Denison, 1997; Winkler, 2002) because they can provide complementary information about bulk-rock material (Vontobel, 2000). X-ray imaging is used to monitor multiphase flows in the chemical and process industry (Gehrke & Wirth, 2005). A lot of reviews and papers are available for X-ray imaging and neutron imaging. The advantage of neutrons over X-rays is their high interaction probability with hydrogen and the lower attenuation in several heavy elements, which are difficult for X-rays to penetrate (e.g., lead, bismuth, uranium). This makes neutrons suitable for some special applications where X-rays fail, even though neutron imaging is more expensive and demanding. The investigation of moisture and corrosion, the detection of explosives and adhesive connections, and the inspection of defects in nuclear fuel or in thick metallic samples are examples in which neutrons can be utilized favorably.

In addition, X-ray imaging is also widely used in medical applications for the human body and small animals to provide anatomical information, and is already being used in

clinical applications. A lot of commercial devices are available for X-ray imaging, such as ECAT from CTI/SIMENS, ADVANCE from GE, MicroCT from ImTek, Inc., etc. On the other hand, neutron imaging is seldom used for the human body and small animals. Even though neutrons have been used for the human body and small animals for decades, most of the applications are focused on the elemental composition analysis of the human body and small animals, such as PGNAA (Chettle & Fremlin, 1984), and as neutron therapy for cancer treatment, such as BNCT (Locher, 1936). None of these applications is for imaging purposes.

In 2000, Adnani and Fallone investigated the feasibility of imaging soft tissues with neutrons from a medical linac. Until now, not too much progress has been made in the neutron imaging field for the human body and small animals. The common sense answer as to why neutron imaging is not suitable for the human body or small animals is that the induced neutron dose is too high for the human body, and the neutron attenuation by human body is so severe that almost no neutrons can penetrate it, especially when the human body is irradiated by thermal neutrons. This is true for the human body; for small animals that are 1-2cm in diameter, however, the neutron attenuation is not that large, and neutrons may be capable of imaging small animals. The induced radiation dose will be discussed in chapter 6.

2.2 Fundamentals of Computed Tomography (Hiriyannaiah, 1997)

The fundamental mathematics of computed tomography was first introduced by J. Radon in 1917. His results were called Radon transforms. The basic radon transform

generates projection data $P_\theta(t)$ from a 2-D slice, $f(x,y)$, as shown in figure 2.1 . Let us consider a simple case: a parallel beam irradiating an object.

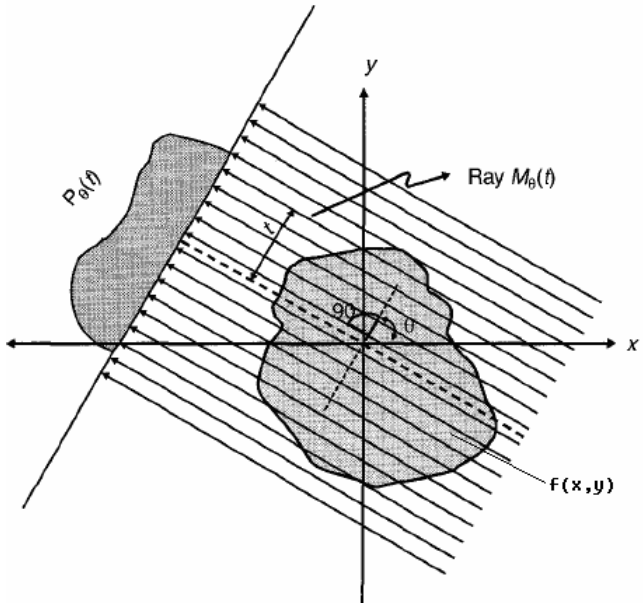

Fig. 2.1 Fundamentals of Computed Tomography (Hiriyannaiah, 1997)

The x and y coordinates are the spatial axes of the 2-D slice. The angle between the parallel beam and the x-axis is θ, which is called the projection angle, and the perpendicular distance of each ray $M_\theta(t)$ to the origin is denoted by t. Then the projection data $P_\theta(t)$ is obtained by performing line integration along each ray $M_\theta(t)$, and is donated by Eq. 2-1:

$$P_\theta(t) = \int_{M_\theta(t)} f(x,y)ds \qquad \text{Eq. (2-1)}$$

where s is along the direction of the ray and $P_\theta(t)$ is called the radon transform of the slice $f(x,y)$ at the projection angle θ . For each θ , $P_\theta(t)$ is a 1-D signal, and $\{P_\theta(t) \mid \theta \in [0,\pi)\}$ gives a complete collection of 1-D projections of the 2-D object $f(x,y)$.

Here, θ is within the range of $[0,\pi)$, since any projection $P_\theta(t)$ obtained at the angle θ higher than this will simply repeat information in $\{P_\theta(t) \mid \theta \in [0,\pi)\}$.

The parametric representation of $M_\theta(t)$ is $x\cos\theta + y\sin\theta = t$. Using the Dirac delta function, we have an alternate representation in Eq. 2-2:

$$P_\theta(t) = \iint f(x,y)\delta(x\cos\theta + y\sin\theta - t)dxdy \qquad \text{Eq. (2-2)}$$

The objective of computed tomography is to reconstruct the slice $f(x,y)$ from its projection collection $P_\theta(t)$, and $P_\theta(t)$ is usually measured by a detector array.

How can we measure the projection data in reality? Simply stated, we need a particle source that can emit a parallel beam of rays and a detector array that can record the information of particles which penetrate the object. In physics, this process is just the line integration in Eq. 2-1 and is denoted by Eq. 2-3:

$$N_d = N_s \exp(-\int_{path} \mu(x,y)ds) \qquad \text{Eq. (2-3)}$$

where N_d is the number of transmitted particles that are detected by the detector array, N_s is the number of incident particles emitted from the source, and $\mu(x,y)$ is the attenuation coefficient at position (x, y) and is what we want to reconstruct, just like $f(x,y)$ in Eq. (2-1). Eq. (2-3) is a very simple representation, since here $\mu(x,y)$ is only spatial dependent. But in

reality, it is also energy dependent $\mu(x, y, E)$; and that will complicate the problem very much.

For X-ray tomography $\mu(x, y, E)$ is the linear attenuation coefficient of X-rays with an irradiated object. For neutron tomography $\mu(x, y, E)$ is the macroscopic cross-section of neutrons with the irradiated object.

2.3 X-ray and Neutron Interactions with Matter

2.3.1 X-ray Interactions with Matter

X-rays interact with electrons outside the atomic nuclei. There are three primary interactions: a photoelectric effect, Compton scattering, and pair production. The probability of each interaction increases as the atomic number increases. The sum of these probabilities is the probability that an X-ray is absorbed or removed from the beam per unit path length, and is called linear attenuation coefficient, which is shown in Eq. 2-4:

$$\mu = \tau(photoelectric) + \sigma(compton) + \kappa(pair) \qquad \text{Eq. (2-4)}$$

Some approximations for the linear attenuation coefficient are available in practice. For example, the linear attenuation coefficient μ for X-rays of a given energy E in a material with material density ρ and an effective atomic number Z is given by the approximation relation form (Jacobs, 1995), with a and b being constants

$$\mu = \rho \left(a + \frac{bZ^{3.8}}{E^{3.2}} \right) \qquad \text{Eq. (2-5)}$$

It is seen that the linear attenuation coefficient changes continuously with the atomic number, and there is no abrupt change, as shown in figure 2-2.

2.3.2 Neutron Interactions with Matter

There are more possible interactions for neutrons than for X-rays. The main interactions for thermal neutrons include neutron scattering and radiative captures. The total probability per unit path length, similar to X-ray attenuation, is called macroscopic cross-section, as shown in Eq. 2-6:

$$\sum_{total} = \sum_{scatter} + \sum_{rad.capture} + \ldots\ldots \qquad \text{Eq. (2-6)}$$

There is no simple relation between the neutron macroscopic cross-section Σ and the atomic number Z, like Eq. (2-5) for X-rays. The neutron macroscopic cross-section changes abruptly with the atomic number, as shown in figure 2-2.

For the human body or for small animal applications, hydrogen is the most dominant element, and has a much larger Σ than other common elements in the thermal energy range, such as C, O, N, and Ca. This leads to a hydrogen concentration that is the most dominant factor in determining the total neutron macroscopic cross-section. Moreover, the thermal neutron-scattering cross-section of hydrogen is almost 100 times as large as the neutron

radiative capture cross-section. This generates a stronger scattering background in thermal neutron applications than those that are encountered in common X-ray applications.

2.3.3 A Comparison of X-rays and Thermal Neutrons (PSI website)

The difference between X-ray imaging and neutron imaging can be explained by comparing the attenuation coefficients of these two particles. The interaction cross-sections of each particle are shown in figure 2-2. It is well known that neutrons interact with the nuclei of the atoms, whereas X-rays interact with the electrons in the shell. Therefore, for X-rays, the interaction probability increases systematically with a higher atomic number, whereas there is not such a tendency for neutrons.

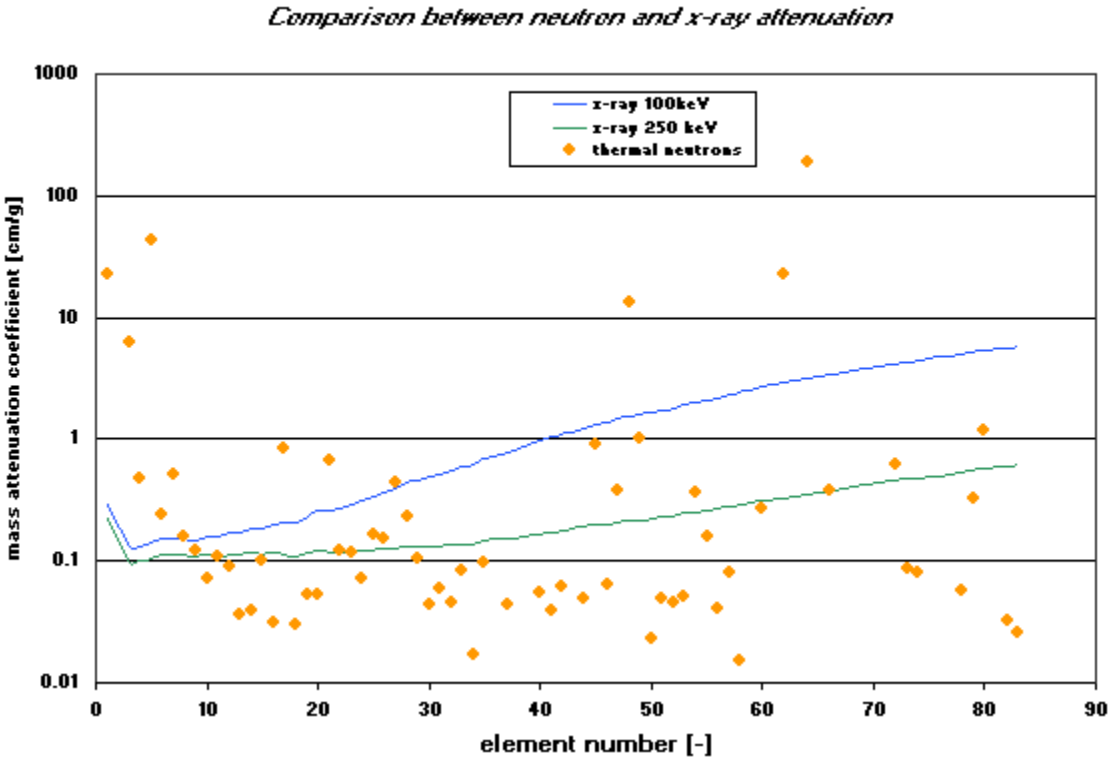

Fig. 2-2 Comparison Between X-ray and Neutron Attenuation (PSI website)

Figure 2.2 shows that hydrogen gives a much higher attenuation for neutrons compared to X-rays, but heavy elements can easily be transmitted by neutrons.

2.3.4 X-ray and Thermal Neutron Attenuation Coefficients for Several Materials

In normal X-ray CT for human body, the typical X-ray energy from x-ray machine is approximately 120keV for the human body, and 20-65keV (Chow, 2001; Alexander, 2004) for mice. In this work, 30keV X-rays are used. The neutron energy used in this work is 0.025ev. The attenuation coefficients of some materials are listed in table 2-1 for these specific X-ray and neutron energies.

Table 2-1 Attenuation Coefficients of Some Materials for X-rays and Neutrons

	X-rays *		Neutrons **
Materials	$\mu/\rho(cm^2/g)$	$\mu\ (cm^{-1})$	$\Sigma(cm^{-1})$
Air	0.3538	0.000426	0.0005
Water	0.3756	0.3756	2.208
Soft tissue	0.3790	0.3790	2.109
Lung	0.3815	0.113	0.60281
Teflon	0.4025	0.9056	0.506
Lucite	0.28	0.336	2.18
Bone	1.331	2.46	2.500
Iron	8.176	92.80	0.38
Lead	30.32	238.62	1.19

* J.H. Hubbell and S.M. Seltzer, Tables of X-Ray Mass Attenuation Coefficients and Mass Energy-Absorption Coefficients, http://physics.nist.gov/PhysRefData/XrayMassCoef/cover.html

** Sears VF, Neutron-scattering lengths and cross-sections, *Neutron News*, Vol. 3, No. 3, 1992, Http://www.ncnr.nist.gov/resources/n-lengths/list.html

Table 2-1 indicates that neutrons have a better contrast between air and soft tissue, water and soft tissue, in terms of attenuation coefficients than X-rays, but X-rays have a better contrast between soft tissue and bone than neutrons. For soft tissue, neutrons have a larger attenuation coefficient than X-rays, which means that neutrons should have a better contrast for soft tissue.

2.4 Monte Carlo Modeling

MCNP5 is used to simulate both X-ray imaging and neutron imaging for small animals. Flux image radiograph (FIR) tally is used to simulate imaging planes, and a 1% relative standard deviation is achieved for each pixel by simulating a large number of histories. Both directly transmitted flux and scattered flux are recorded.

2.4.1 Phantom Description

There are two kinds of phantoms. One is for the purpose of radiography, shown in figure 2-3; the other is for tomography, shown in figure 2-4. For each phantom, two different materials are simulated. One is using plastic material, such as Teflon for bone, and Lucite for soft tissue, which is called a plastic phantom. The other is using the real elemental components from National Institute of Standards and Technology (NIST) for soft tissue, bone, and lung, which is called a real phantom.

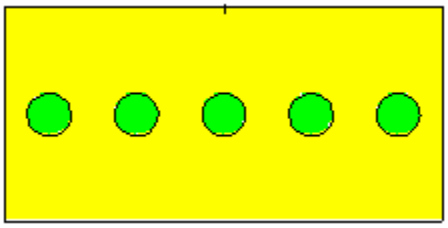

Fig. 2-3. The Phantom for Radiography

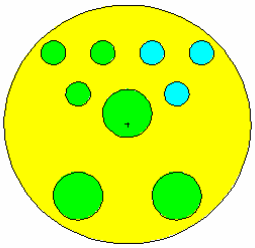

Fig. 2-4. The Phantom for Tomography

For both phantoms, the base material (the yellow region in the figures) is used to represent soft tissue. The holes in the phantoms are used to represent bone or lung. The elemental compositions of each material are listed in table 2-2. The geometric dimensions of each phantom will be described later in detail.

Table 2-2 Elemental Compositions of Each Material

Chemical Symbol	Atomic Number	Weight Fraction				
		Lucite	Teflon	Bone	Soft Tissue	Lung
H	1	0.08		0.063984	0.104472	0.10134
C	6	0.60	0.24	0.278000	0.232190	0.10238
N	7	0.32		0.027000	0.024880	0.02866
O	8			0.410016	0.630238	0.75752
F	9		0.76			
Na	11				0.001130	0.00184
Mg	12			0.002000	0.000130	0.00007
Si	14					0.00006
P	15			0.070000	0.001330	0.00080
S	16			0.002000	0.001990	0.00225
Cl	17				0.001340	0.00266
K	19				0.001990	0.00194
Ca	20			0.147000	0.000230	0.00009
Fe	26				0.000050	0.00037
Zn	30				0.000030	0.00001
Rb	37					0.00001
Density:		1.2 g/cm^3	2.2 g/cm^3	1.85 g/cm^3	1.0 g/cm^3	0.296 g/cm^3

2.4.2 Radiography Simulation

Both thermal neutrons and 30keV X-rays are simulated. The simulation geometry is the same for them, and is shown in figure 2-5. The source is a parallel-like plane source. The divergence parameter L/D is 90 (L is the length of the collimator; D is diameter of the aperture), which is set to be close to the real data in the neutron imaging facility at North Carolina State University. The phantom for radiography is used. The distance between the source plane and the phantom is 14cm. The imaging plane is placed behind the phantom at a distance of 1cm.

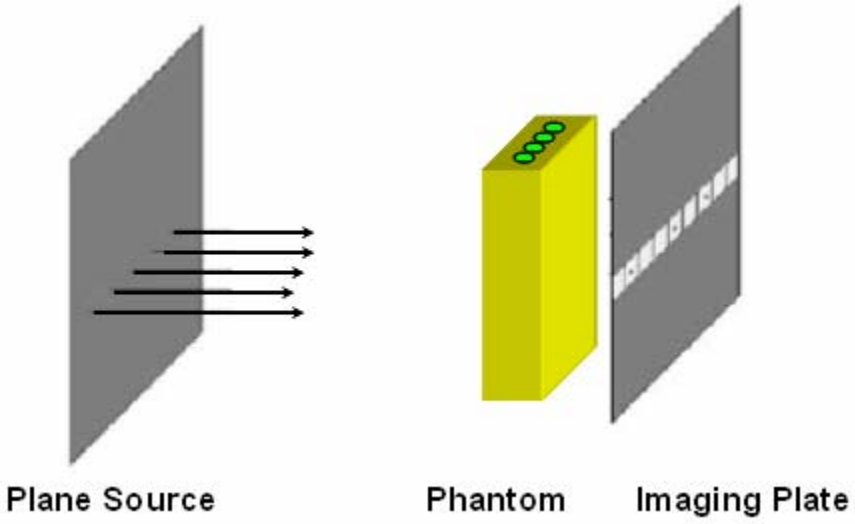

Fig. 2-5 The MCNP Simulation Geometry for Radiography

2.4.3 Tomography Simulation

Tomography simulation is similar to radiography simulation, but more projection data are required. Here the phantom for tomography is used. The MCNP simulation geometry is

the same for neutrons and X-rays, and is shown in figure 2-6. The phantom is rotated by 64 steps, from 0º to 180º, to get 64 projections. For each projection, there are 128 image pixels.

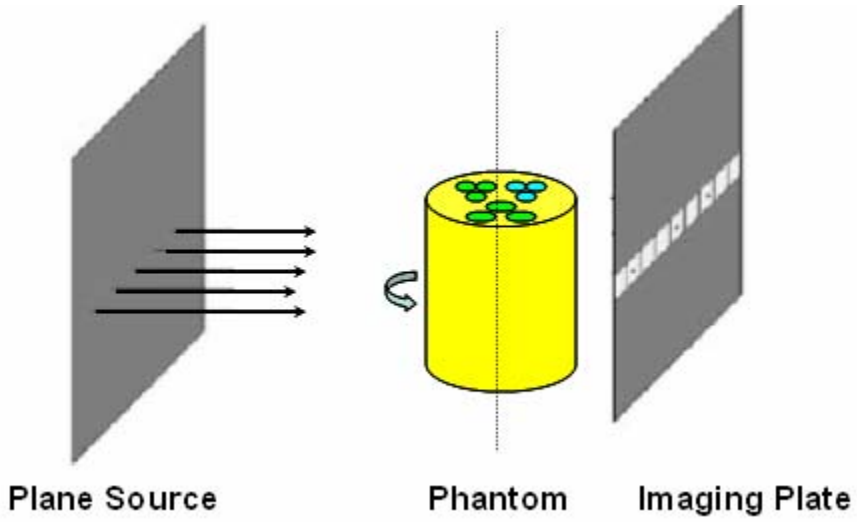

Fig. 2-6 The MCNP Simulation Geometry for Tomography

2.5 Results and Analysis:

2.5.1. Radiography Simulation Results

The phantom for radiography is used. The diameter of the hole is 1mm. The distance between the two adjacent holes is 2mm (center to center). For the plastic phantom, the yellow region is Lucite, and the green region is Teflon. For the real phantom, the yellow region is soft tissue, and the green region is bone.

2.5.1.1 30keV X-ray radiography

The transmitted X-ray flux is plotted in figure 2-7 when the real phantom is irradiated. The calculated attenuation coefficient along the parallel direction is plotted in figure 2-8. The radiography images of the real phantom are displayed in figure 2-9.

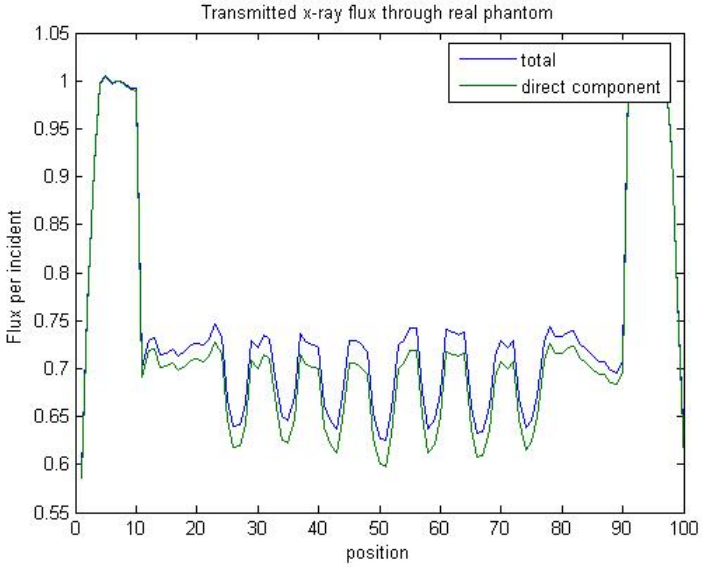

Fig. 2-7 Transmitted X-ray Flux Through the Real Phantom

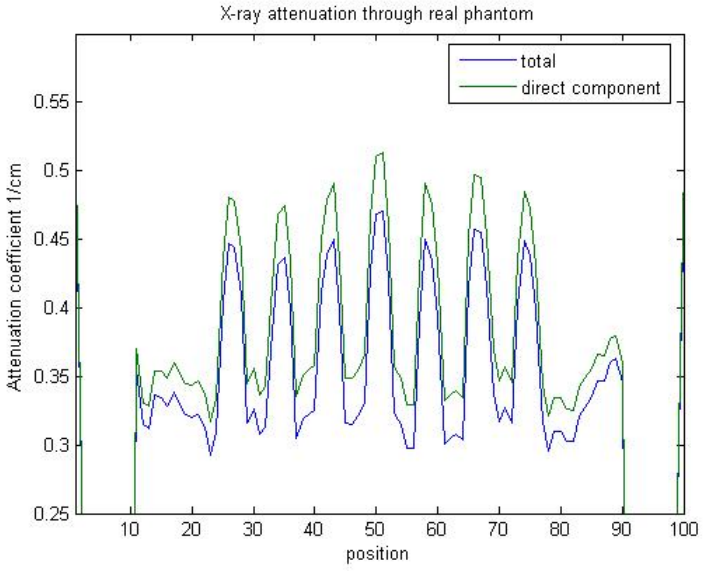

Fig. 2-8 Calculated Attenuation Coefficient for the Real Phantom

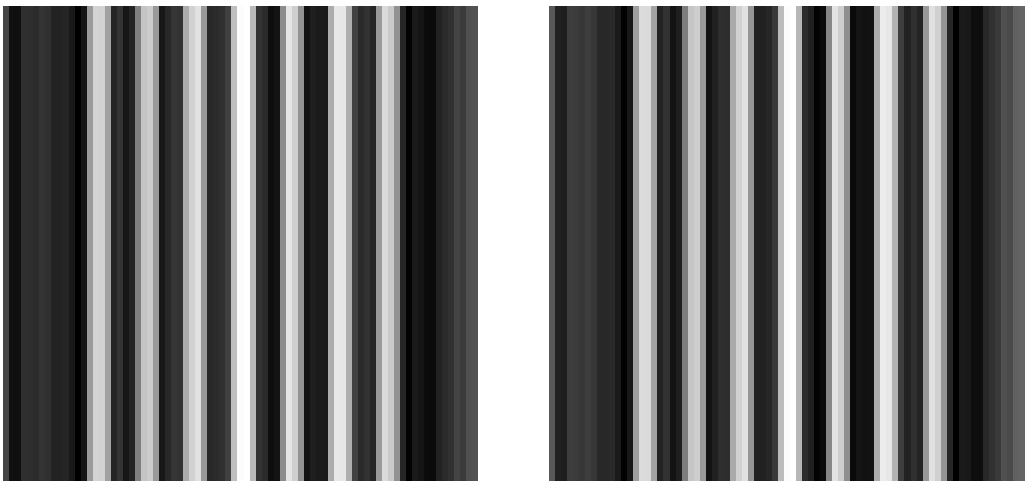

Direct Total

Fig. 2-9 X-ray Radiography for the Real Phantom

The difference between ‘direct’ and ‘total’ is the scattered component. This means that the ‘direct’ image has no scattering particles, only the net-penetrated particles. Therefore, the ‘total’ images are closer to the realistic conditions, including both ‘direct’ and ‘scatter’ components.

It can be seen that almost 70% of X-rays can penetrate the 1cm-thick real phantom. The equivalent attenuation efficient of the real phantom is around 0.4/cm, which agrees with the results in table 2-1.

The transmitted X-ray flux is plotted in figure 2-10, which illustrates what happens when the plastic phantom is irradiated. The calculated attenuation coefficient along the parallel direction is plotted in figure 2-11. The radiography images of the plastic phantom are displayed in figure 2-12.

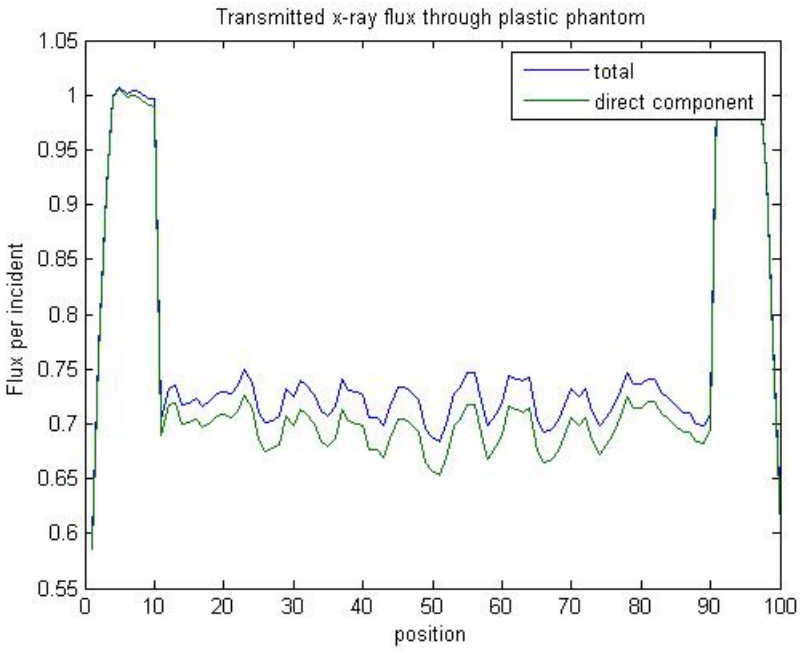

Fig. 2-10 Transmitted X-ray Flux Through the Plastic Phantom

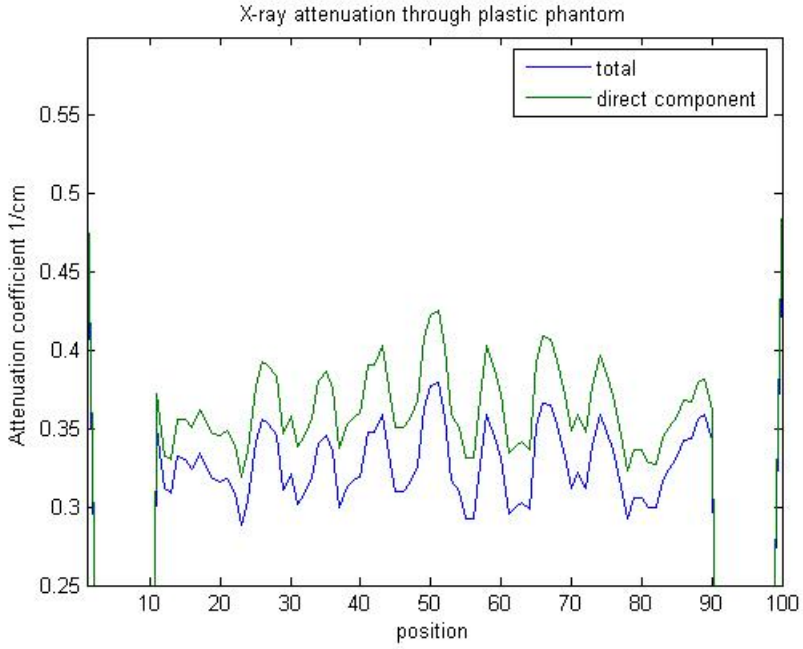

Fig. 2-11 Calculated Attenuation Coefficient for the Plastic Phantom

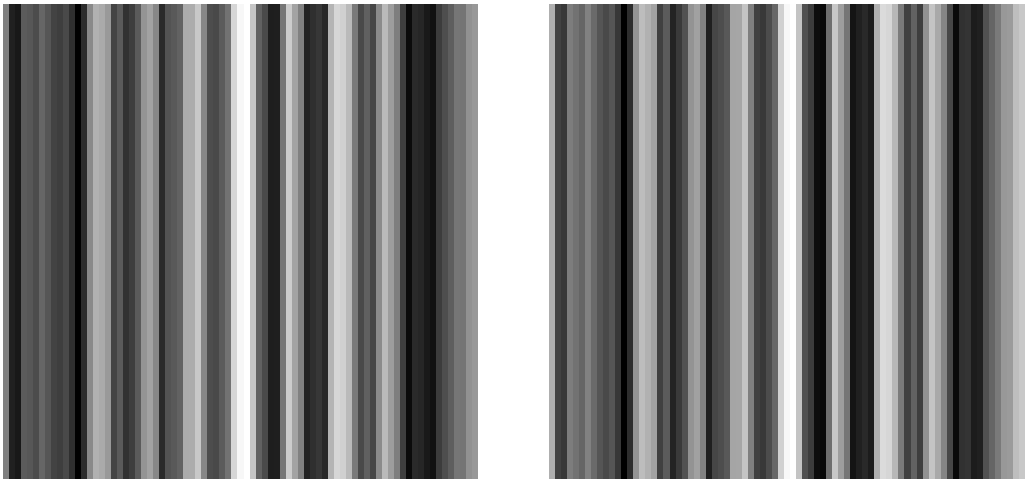

Direct Total

Fig. 2-12 X-ray Radiography for the Plastic Phantom

Almost 70% of X-rays can penetrate the 1cm-thick plastic phantom. The equivalent attenuation efficient of the plastic phantom is around 0.35/cm, which agree with the results in table 2-1.

There is no big difference between direct-images and total-images, which is the scattered component for both the plastic phantom and the real phantom. Further analysis of the raw data shows that the scattered component is about 4-5% of the total transmitted X-ray flux. Both radiographic images from the plastic phantom and the real phantom give the same black-and-white pattern. That means that Lucite and Teflon are good substitutes for soft tissue and bone in X-ray imaging testing since the relative difference between Lucite and Teflon is similar to of the difference between soft tissue and bone. In fact, Lucite and Teflon have been used in practical X-ray experiments as alternatives for soft tissue and bone.

2.5.1.2 Thermal Neutron Radiography

The transmitted neutron flux is plotted in figure 2-13 when the real phantom is irradiated. The calculated attenuation coefficient along the parallel direction is plotted in figure 2-14. The radiography images of the real phantom are displayed in figure 2-15.

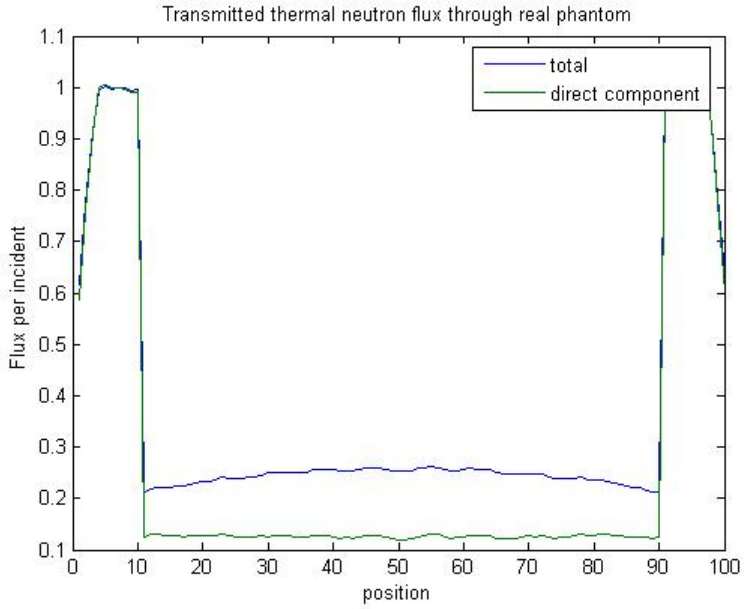

Fig. 2-13 Transmitted Neutron Flux Through the Real Phantom

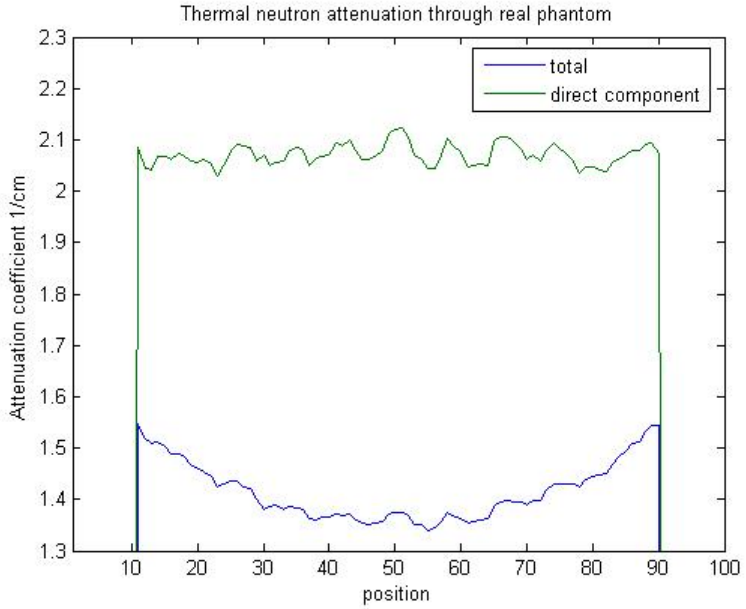

Fig. 2-14 Calculated Attenuation Coefficient for the Real Phantom

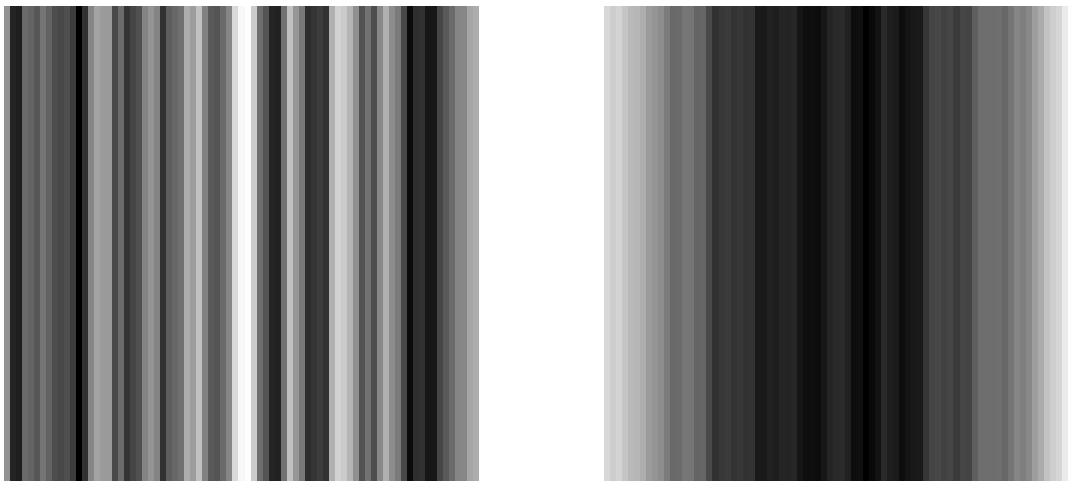

Fig. 2-15. Neutron Radiography for the Real Phantom

It can be seen that the scattered component takes a large amount of the total transmitted flux. Almost 24% of the thermal neutron can penetrate the object, but half of the total transmitted flux is from scattered neutrons. The calculated attenuation coefficient by direct component is around 2.1/cm, which agreed with the results in table 2-1.

The transmitted neutron flux is plotted in figure 2-16, which shows what happens when the plastic phantom is irradiated. The calculated attenuation coefficient along the parallel direction is plotted in figure 2-17. The radiography images of the plastic phantom are displayed in figure 2-18.

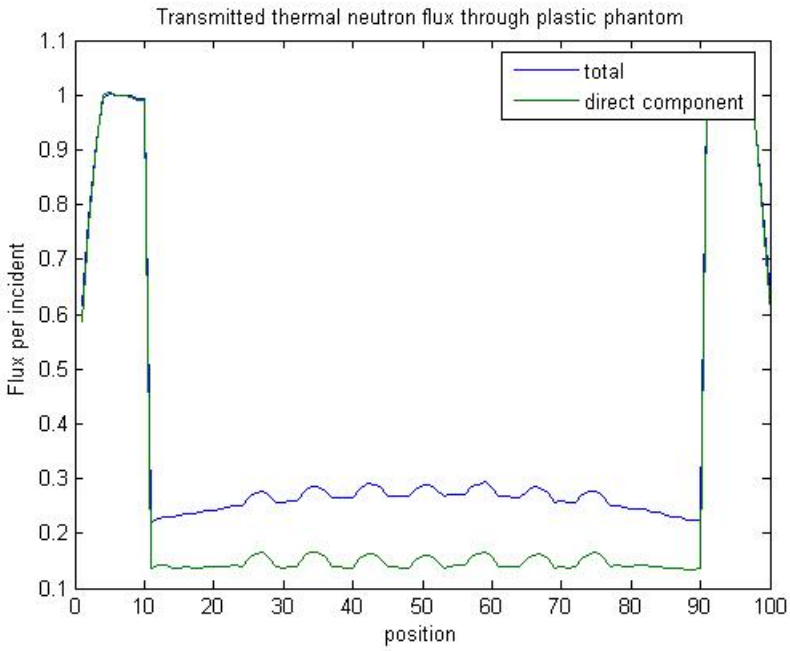

Fig. 2-16 Transmitted Neutron Flux Through the Plastic Phantom

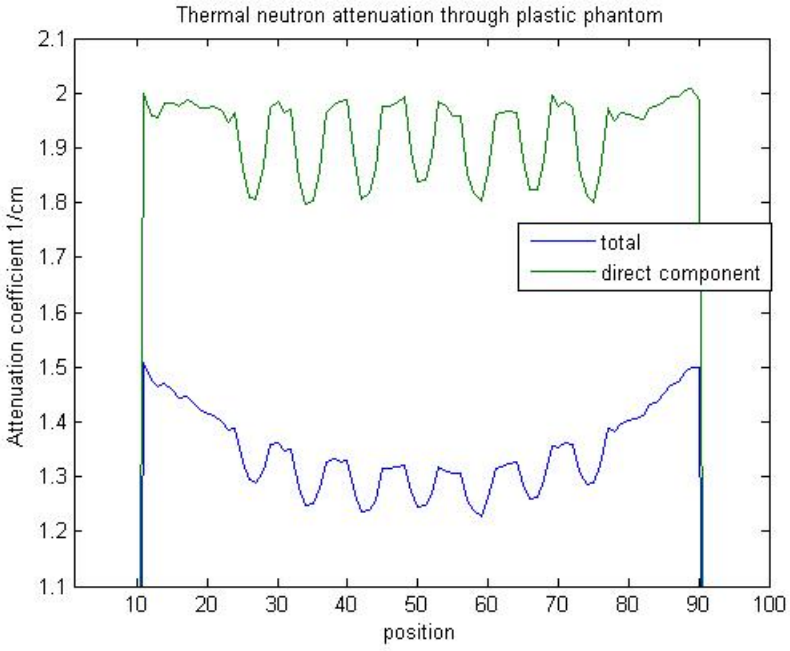

Fig. 2-17 Calculated Attenuation Coefficients for the Plastic Phantom

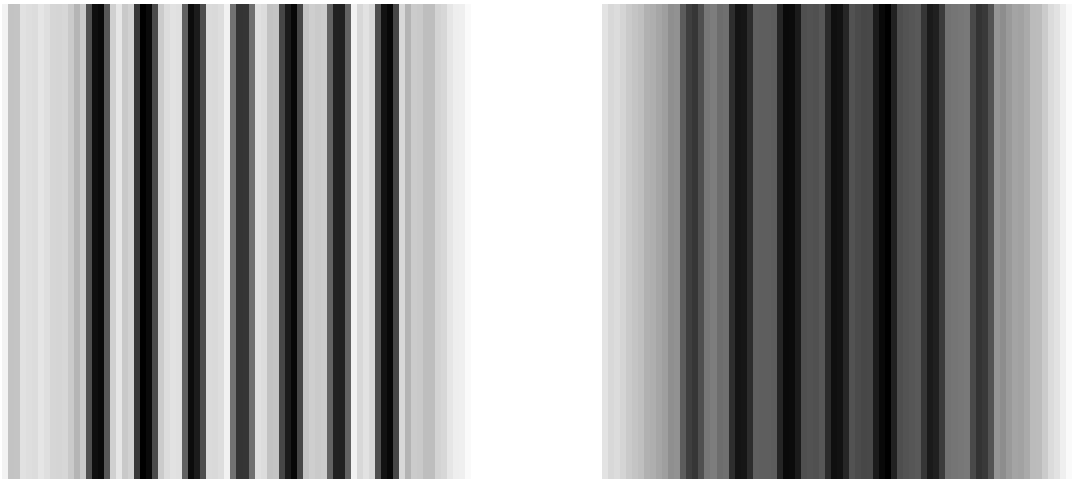

Direct Total

Fig.2-18. Neutron Radiography for the Plastic Phantom

Similar to the real phantom results, the scattered component also takes a large amount of the total flux. Compared with the real phantom results, there are more neutrons penetrating the object, and the plastic phantom has a smaller attenuation coefficient, since the attenuation coefficient of Teflon by thermal neutrons is only 0.506/cm, which is much smaller than that of bone.

Comparing real phantom images and plastic phantom images, it can be seen that they are totally reversed in a white-and-black pattern. This is caused by the totally different attenuation relation between Lucite-Teflon and tissue-bone for neutrons when compared with X-rays. For X-rays, the attenuation coefficient of Lucite is smaller than that of Teflon; but for neutrons, the attenuation coefficient of Lucite is much larger than that of Teflon. All of this information tells us that Lucite and Teflon are not good substitutes for soft tissue and bone in neutron imaging testing.

2.5.1.3 30keV X-ray Radiography vs. Thermal Neutron Radiography

So far, it has been shown that one significant difference between X-ray radiography and neutron radiography is the scatter effect. In our application, the scatter component is around 4-5% for X-rays, but 50% for neutrons. Another difference is that one material may have a larger attenuation coefficient for X-rays, but a smaller attenuation coefficient for neutrons. This is caused by the different physics between X-ray interactions and neutron interactions with matter.

2.5.2 Tomography Simulation Results

The tomography phantom is shown in figure 2-19 below.

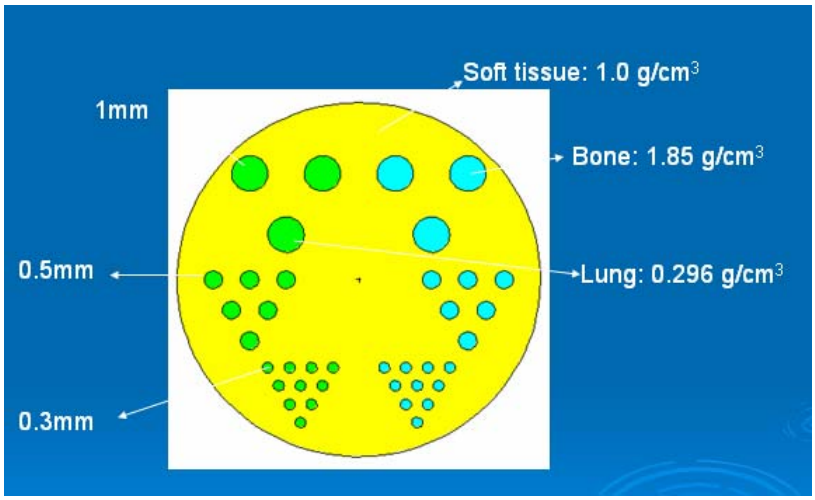

Fig. 2-19 The Phantom for Tomography

It is a cylindrical phantom with a diameter of 1cm. There are several groups of small cylindrical holes with various sizes representing different materials. In this phantom, the yellow region is soft tissue with a density of 1.0g/cm^3, the green region is lung with a density of 0.296g/cm^3, and the blue region is bone with a density of 1.85g/cm^3. The diameters of the holes are 1mm, 0.5mm, and 0.3mm, respectively. The elemental composition for each part is obtained from the NIST standard and shown in table 2-2.

After rotating the phantom 64 times from 0º to 180º, 64 projections data are obtained. Stacking them together, the sinograms are obtained and displayed in figure 2-20. (Note: these sinograms correspond to the total component, which is the sum of the direct component and the scatter component).

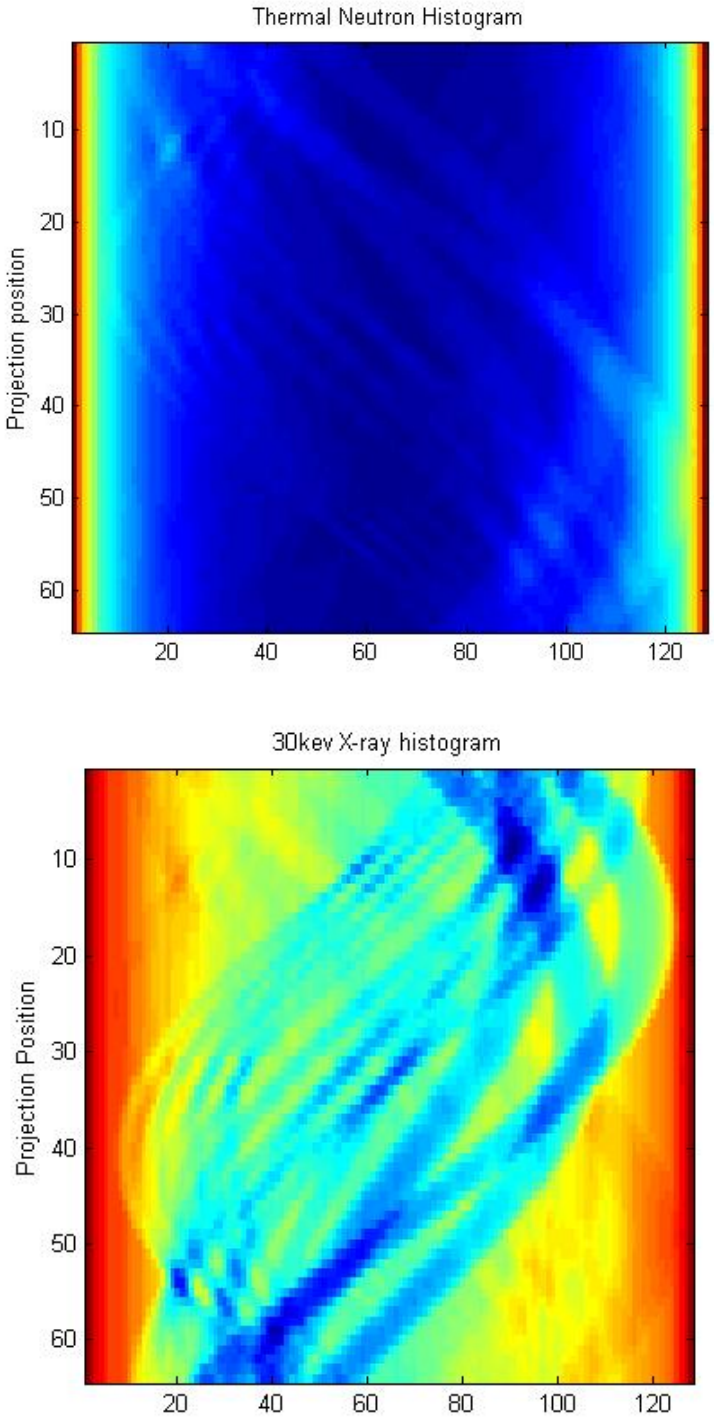

Fig. 2-20. Sinogram for Neutron and X-ray Tomography

The y axis represents different projection angles. For each projection, there are 128 pixel points which cover the whole diameter of the phantom. It is seen that the 30keV X-ray sinogram has a better contrast than the thermal neutron sinogram does. The raw data of certain projection is displayed in figure 2-21.

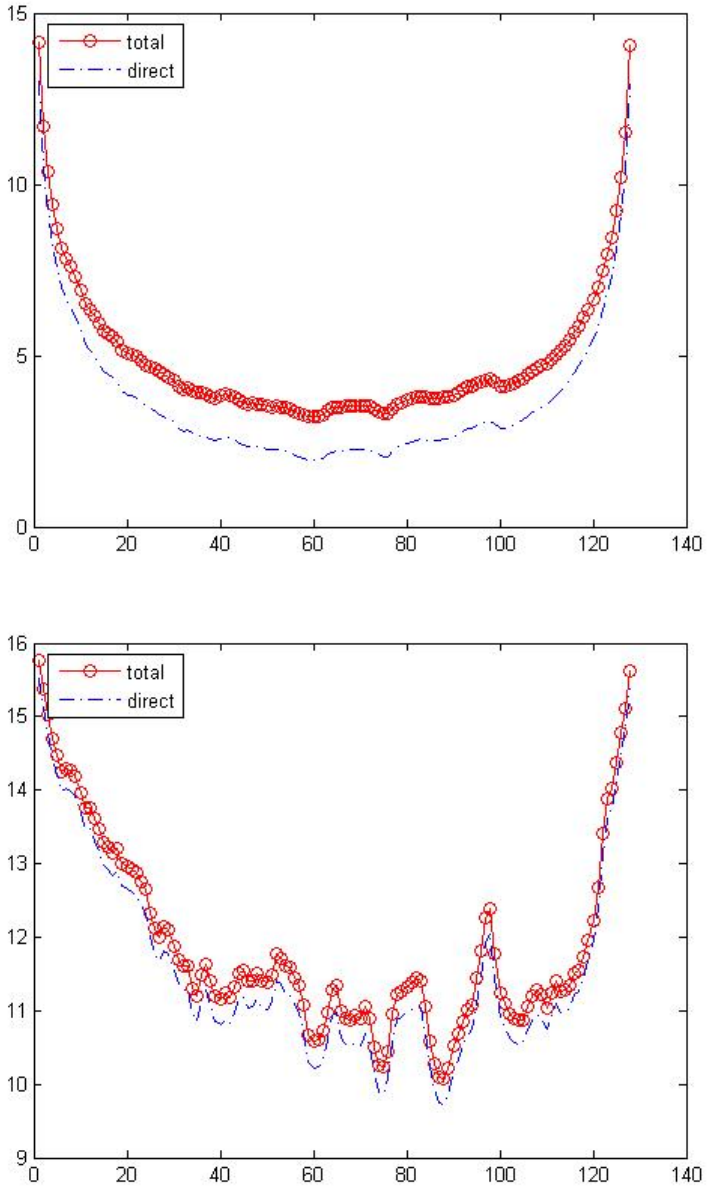

Fig. 2-21 Raw Flux Data of One Projection
The one above is for neutrons. The one below is for X-rays.

In the figure, the red circle represents the total component, and the blue dots represent the direct component. The difference, the scatter component, is calculated and displayed in figure 2-22.

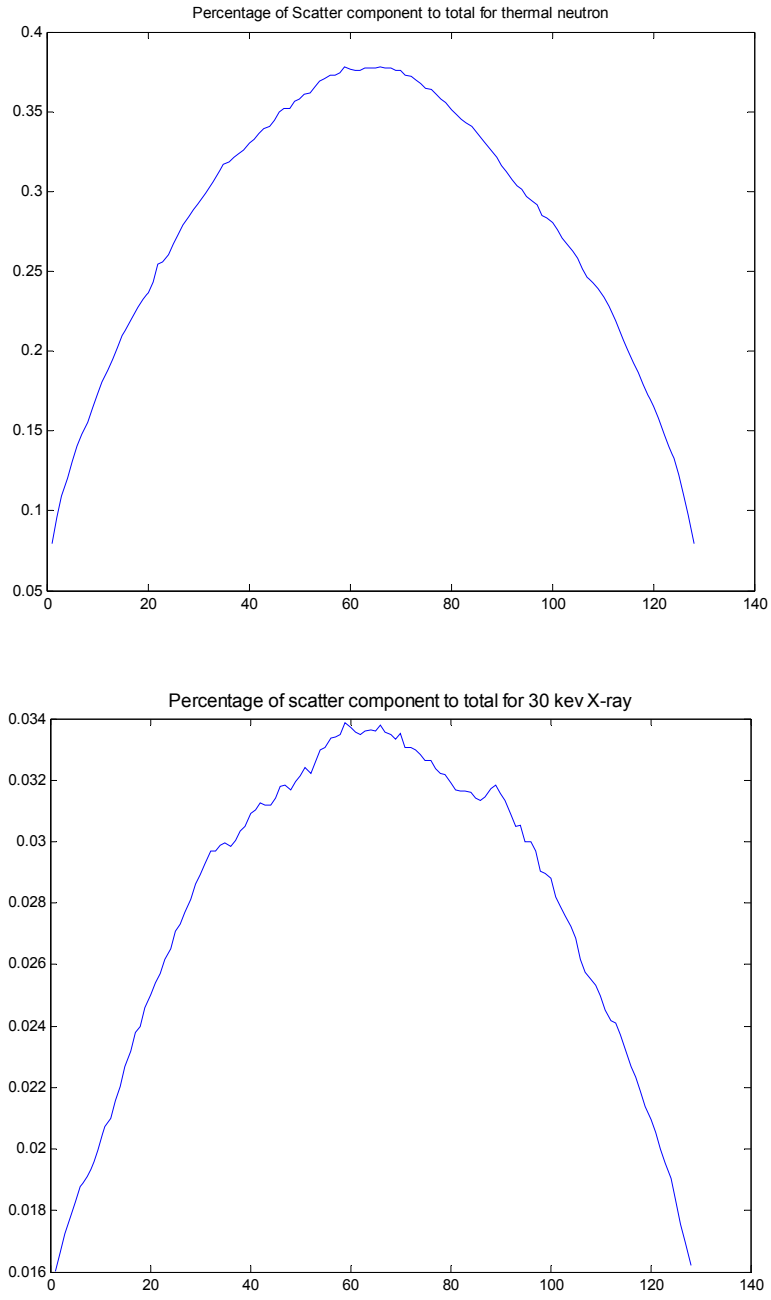

Fig. 2-22 Percentage of Scatter Component vs. Position
The one above is for neutrons. The one below is for X-rays.

From the figure, it can be seen that the scatter component is around 38% of total flux intensity in the middle, and 7% at the sides for neutron tomography. For X-ray tomography, the shape is same, but the magnitude is much lower. The absolute intensity of the scatter component has been calculated, and it is 10% stronger in the middle than at the boundary for both X-ray tomography and neutron tomography. Here, the ratios of the scatter component to the total are a little different from those of radiographic cases, because the different phantoms are used.

Matlab was used to reconstruct images, and the same parameters were used in the reconstruction method for both thermal neutron tomography and X-ray tomography. The reconstructed images are shown in figure 2-23 below.

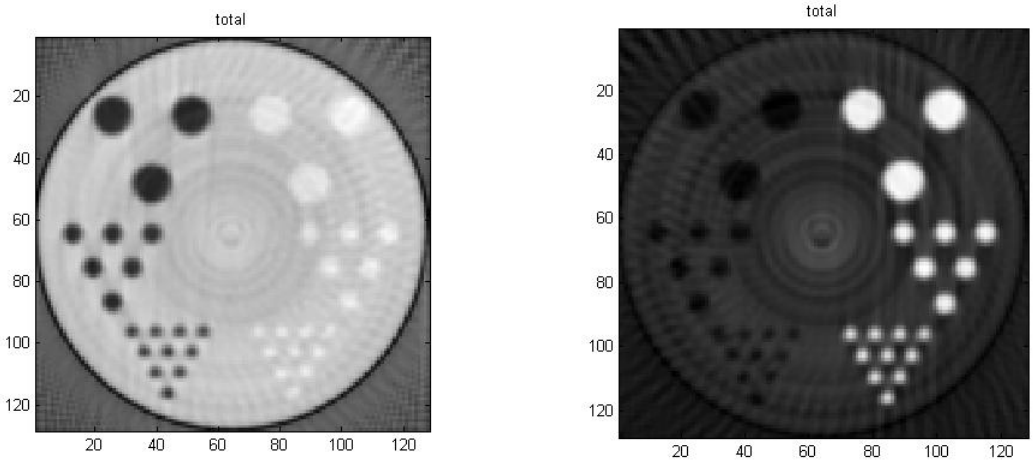

Fig. 2-23 Tomography Images
The one on the left is for thermal neutrons, and the one on the right is for X-rays.

The reconstructed images above correspond to the total components in the simulation. This means that the scatter component is taken into account in the reconstruction process, and the

intensities of the scatter components are shown in figure 2-22. The values of the 24th row, which acrosses the both bone and lung regions, of each image are shown in figure 2-24.

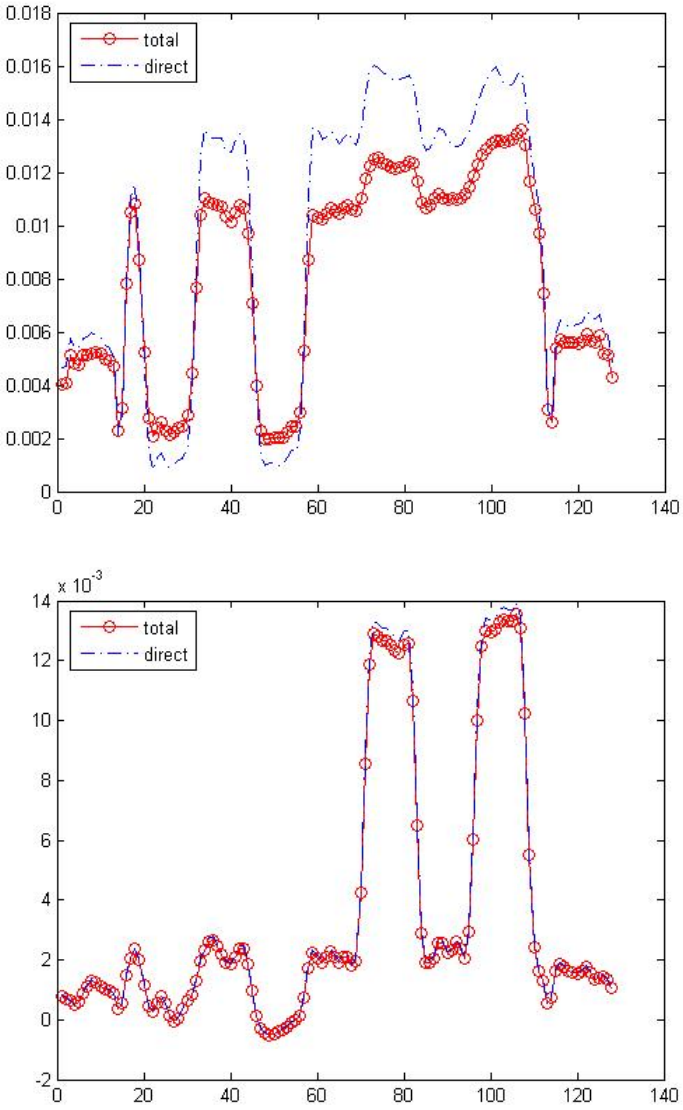

Fig. 2-24 Calculated Attenuation Coefficient of the 24th Row
The one above is for thermal neutrons, and the one below is
for X-rays.

The red circles represent the results reconstructed by using the total flux. The blue curves represent the results reconstructed by using only the direct components, which is the ideal case. The y axis represents the reconstructed attenuation coefficient for X-rays and neutrons.

These data are not the absolute attenuation coefficient data for each material. Therefore, only the relative data analysis between each material is meaningful. First, it can be seen that there is a larger difference between the results of the total component and the results of the direct component for thermal neutrons, compared with the X-ray results. The difference tells us that the scatter component will decrease the whole image contrast. Second, it can be seen that the contrast between soft tissue and bone is almost 1.2 for thermal neutrons, and 6 for X-rays. The contrast between soft tissue and lung is 5.5 for thermal neutrons, and 6 for X-rays.

2.6 Preliminary Experiments

Two mouse fetuses shown in figure 2-25 have been irradiated by thermal neutrons in the neutron imaging facility at North Carolina State University. Currently, only neutron radiography has been applied to the fetuses. The neutron tomography system is still being set up. The neutron flux at the fetuses' position is around $10^7/cm^2.s$. The collimation parameter is around 90 for L/D.

Fig. 2-25 Mouse Fetuses

Several images are obtained and shown in figure 2-26. These images correspond to the distance between the fetus and the imaging plate from 0cm, 1cm, 2cm, 4cm, and 8cm to 16cm.

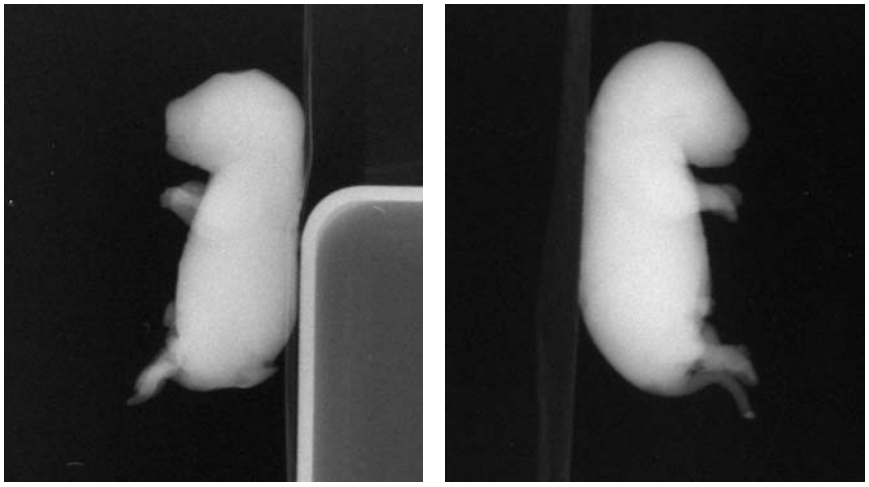

0cm 1cm

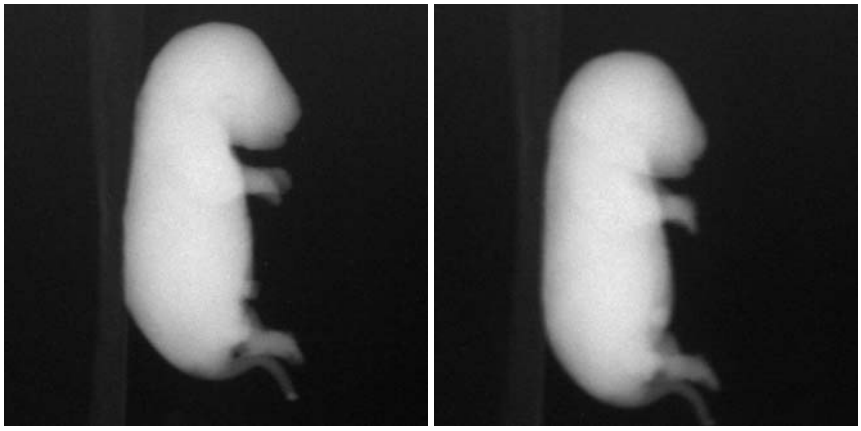

2cm 4cm

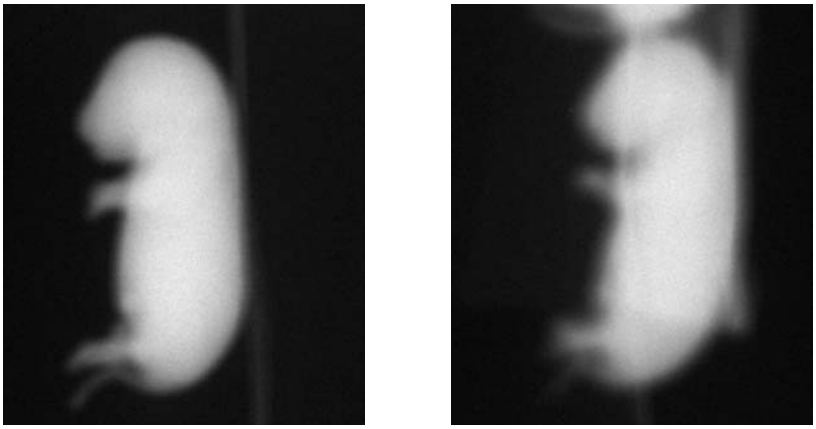

8cm 16cm

Fig. 2-26. Neutron Radiography for Mouse Fetuses

We can clearly see the difference caused by increasing the distance between the fetus and the imaging plate. The images are blurred as the distance increases due to the parallel-like, but non-deal parallel beam. However, the 0cm image is also not the best one, because the scatter effect is the worst at that distance. The distance that is the best for neutron imaging of mouse fetuses is still being investigated.

An analysis of the raw neutron flux data has been done and can be found in figure 2-27. It can be seen that the neutron flux decreases as the distance increases from 0cm to 16cm. It can be explained that the scatter is very strong when the imaging plate is placed close to the fetus, but the scatter is reduced to a low level when the imaging plate is placed far away from the fetus. In this experiment, the scatter level is not that high when the distance is greater than 4cm. When the distance is 1cm, the ratio of the scatter component to the total is almost 37%. That result agreed with our simulation.

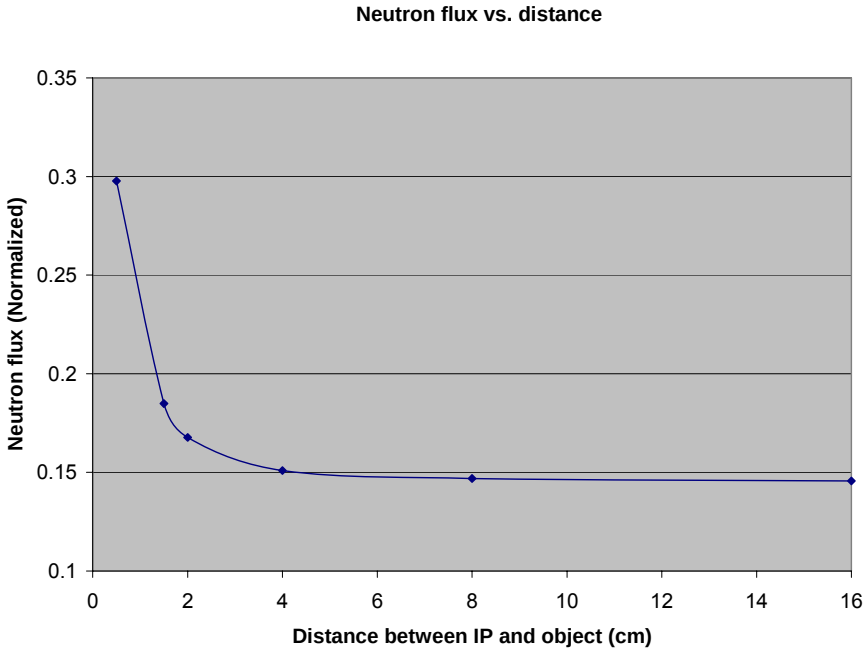

Fig. 2-27 Experimental Neutron Flux vs. Object-to-IP Distance

2.7 Summary

In this chapter, X-ray imaging and neutron imaging were simulated by MCNP5, and compared with each other. The major difference between X-ray imaging and neutron imaging is originating from the different X-rays and neutrons interactions with matter. Neutrons interact with the nuclei of the atoms, whereas X-rays interact with the electrons in the shell. The interaction probability increases as the atomic number increases for X-rays, whereas neutrons do not exhibit such systematic behavior.

For small animal applications, the attenuation coefficient of X-rays is mainly determined by object density, but for thermal neutrons, it is more related to the hydrogen concentration of objects. Totally different information is achieved by X-ray imaging and neutron imaging.

X-ray tomography provides a better contrast between bone and soft tissue than neutron tomography. However, neutron tomography provides better soft tissue contrast because of its higher attenuation coefficient. The current problem is that the scattered component is too severe. The possible solution is using a collimation grid made by a nanotube (Kumakhov, 2000) to filter the scattered component.

The plastic phantom is a good alternative for the human body in X-ray experiments, but it is not effective in thermal neutron experiments.

3. PROMPT GAMMA-RAY MODELLING

A Monte Carlo simulation code is developed in this chapter, which will be the main platform to test the feasibility of prompt gamma-ray imaging.

3.1 Available Monte Carlo Simulation Codes

The overall approach in accomplishing this project is to first use Monte Carlo simulation; that is, either the specific purpose code CEARCPG (Han, 2005), developed at North Carolina State University, or the general purpose codes GEANT4 (Agostinelli et al., 2003) or MCNP5 (LANL, 2004) to predict experimental results and investigate the feasibility of this project.

MCNP5 is a general-purpose, neutron, photon, and electron transport simulation code, which was developed at the Los Alamos National Lab. MCNP5 can be used to simulate prompt gamma rays. However, MCNP5 cannot simulate coincident prompt gamma rays, which are considered to be the most useful to improve the signal-to-noise ratio in neutron-related applications, where normally the gamma ray background would be very intense. The coincidence counting technique (Metwally, 2004; Gardner, 2000) has been investigated in CEAR and has been proved to be able to improve the signal-to-noise ratio. Therefore, MCNP is not considered the final simulation platform for PGI, but is still used in this project mainly for estimating the absorbed dose induced by thermal neutrons and neutron transmission imaging.

GEANT4 is another popular general purpose simulation environment, and was developed by CERN (European Organization for Nuclear Research). Due to its complete physics models, powerful visualization interfaces, and the fact that it has been widely benchmarked, GEANT4 has been selected to be the platform for emission tomography simulation, which is called GATE (Geant4 Application for Tomographic Emission) (Strul et al., 2003). In this work, GEANT4 is also considered as the final simulation platform for PGI.

CEARCPG was developed by our CEAR group. Recently, it has been updated to be capable of simulating coincident prompt gamma rays (Han, 2005). The problem with CEARCPG is that the CEARCPG geometry package is based on MCNP4B, which cannot simulate repeated geometry structures. However, simulating repeated structures is widely used in imaging related applications such as detector array design and collimation array design in PGI. The other problem with CEARCPG is that CEARCPG is based on the FORTRAN language and does not have very powerful visualization ability. All of these problems make CEARCPG not very suitable for PGI simulation. But we still use CEARCPG to simulate some non-imaging related calculations, such as yields and detector spectrum to benchmark with Geant4-based results. Further development to CEARCPG to incorporate a new geometry package will be implemented in future.

3.2 Introduction to GEANT4

GEANT4 is a state-of-the-art radiation toolkit for the comprehensive three-dimensional Monte Carlo simulation of energetic particles from Pev energies to hundreds of

ev. The toolkit was initially developed for the high-energy physics community, primarily to support experiments for the CERN's Large Hadron Collider, but has found increasing use within other communities, such as medical physics, high-energy astrophysics, and space radiation effects groups. Its object-oriented design and implementation in C++ means that the code is flexible and can be enhanced easily through class inheritance, and it is well supported by geometry visualization and data analysis utilities.

The heart of GEANT4 is the abundant set of physics processes. There are seven main categories of physics processes. There are electromagnetic, hadronic, decay, photolepton-hadron, optical, parameterization, and transportation. You may write your own physics processes, and add them to GEANT4 libraries. Electromagnetic processes and hadronic processes are two processes that we will use primarily in PGI simulation.

In electromagnetic interactions, there are two models. One is the standard electromagnetic process. The other is a low-energy electromagnetic interaction. In the standard electromagnetic process, the following processes are available in GEANT4:

- Photon processes
  - Compton scattering (class name: *G4ComptonScattering*)
  - Gamma conversion (also called pair production; class name: *G4GammaConversion*)
  - Photo-electric effect (class name: *G4PhotoElectricEffect*)
  - Muon pair production (class name: *G4GammaConversionToMuons*)
- Electron/positron processes
  - Ionisation and delta ray production (class name: *G4eIonisation*)
  - Bremsstrahlung (class name: *G4eBremsstrahlung*)
  - Positron annihilation into two gamma (class name: *G4eplusAnnihilation*)
  - Positron annihilation into two muons (class name: *G4AnnihiToMuPair*)
  - Positron annihilation into hadrons (class name: *G4eeToHadrons*)
  - Synchrotron radiation (class name: *G4SynchrotronRadiation*)
- Muon processes

Ionisation and delta ray production (class name: *G4MuIonisation*)
Bremsstrahlung (class name: *G4MuBremsstrahlung*)
e+e- pair production (class name: *G4MuPairProduction*)

- Hadron/ion processes
  Ionisation (class name: *G4hIonisation*)
  Ionisation for ions (class name: *G4ionEnergyLoss*)
- The multiple scattering process

In low-energy electromagnetic processes, the following processes are available:

- Photon processes
  Compton scattering (class name: *G4LowEnergyCompton*)
  Polarized Compton scattering (class name: *G4LowEnergyPolarizedCompton*)
  Rayleigh scattering (class name: *G4LowEnergyRayleigh*)
  Gamma conversion (also called pair production; class name: *G4LowEnergyGammaConversion*)
  Photo-electric effect (class name: *G4LowEnergyPhotoElectric*)
- Electron processes
  Bremsstrahlung (class name: *G4LowEnergyBremsstrahlung*)
  Ionisation and delta ray production (class name: *G4LowEnergyIonisation*)
- Hadron and ion processes
  Ionisation and delta ray production (class name: *G4hLowEnergyIonisation*)

In the hadronic processes, the following processes are available in Geant4:

Hadrons at Rest

- pi-absorption (class name: *G4PionMinusAbsorptionAtRest* or *G4PiMinusAbsorptionAtRest*)
- kaon-absorption (class name: *G4KaonMinusAbsorptionAtRest* or *G4KaonMinusAbsorption*)
- neutron-capture (class name: *G4NeutronCaptureAtRest*)
- anti-proton annihilation (class name: *G4AntiProtonAnnihilationAtRest*)
- anti-neutron annihilation (class name: *G4AntiNeutronAnnihilationAtRest*)
- mu-capture (class name: *G4MuonMinusCaptureAtRest*)

Hadrons in Flight

- G4HadronElasticProcess
- G4HadronInelasticProcess
- G4HadronFissionProcess
- G4CaptureProcess

3.3 Prompt Gamma Ray Simulation by GEANT4

3.3.1 Environment

Part I Software Environment

Windows + Cygwin
GEANT4.5.2
Gcc3.2.2

Part II Physics Environment

Neutron Processes:

Elastic Scattering (class name: G4NeutronHPElastic)
Inelastic Scattering (class name: G4NeutronHPInelastic)
Capture (class name: G4NeutronHPCapture)

Photon Processes:

Compton Scattering (class name: G4LowEnergyCompton)
Rayleigh scattering (class name: G4LowEnergyRayleigh)
Photo-electric effect (class name: G4LowEnergyPhotoElectric)
Pair production (class name: G4LowEnergyGammaconversion)

Electron Processes:

Ionisation (class name: G4LowEnergyIonisation)
Bremsstrahlung (class name: G4LowEnergyBremsstrahlung)

Positron Processes:

Ionisation (class name: G4eIonisation)
Bremsstrahlung (class name: G4eBremsstrahlung)
Annihilation (class name: G4eplusAnnihilation)

To accelerate the simulation speed, the energy cut for the electron and the positron is 100Mev. The electron and the positron are still to be produced, but they will deposit all of their energy locally. For the positron, the annihilation process is still active. The energy cut for the photon is 10keV.

Part III Nuclear Data

Default data libraries:

G4EMLOW2.2 for low-energy electromagnetic processes

G4NDL3.7 for high-precision neutron processes

PhotonEvaporation2.0 for photon evaporation

RadiativeDecay3.0 for radio-active decay hadronic processes

3.3.2 Neutron Capture Reaction Simulation by GEANT4

There are two kinds of methods to simulate neutron capture reactions and produce prompt gamma rays in GEANT4. One is by sampling the prompt gamma ray spectrum for each isotope, which is the most popular method and is also used in MCNP shown in figure 3-1.

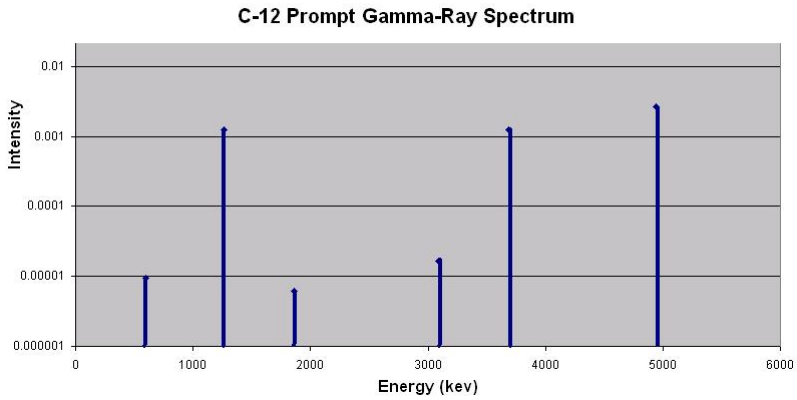

Fig. 3-1 C-12 Prompt Gamma-Ray Spectrum

Basically, the prompt gamma-ray spectrum is a two-column table. The first column is the energy information of prompt gamma rays; the other column is the intensity information of prompt gamma rays. A random number is used to pick up one specific energetic gamma ray

based on the intensity information. The good point is that the intensity information is guaranteed, and the single spectrum will definitely be correct. The biggest problem is that time information is lost. Each gamma ray is produced independently, and this does not agree with neutron capture physics. The other way to simulate a neutron-capture reaction and produce prompt gamma rays is to follow the nuclear structure of a produced compound during one capture reaction. For example, a thermal neutron is absorbed by C-12. The new compound is C-13 and its nuclear structure is displayed in figure 3-2.

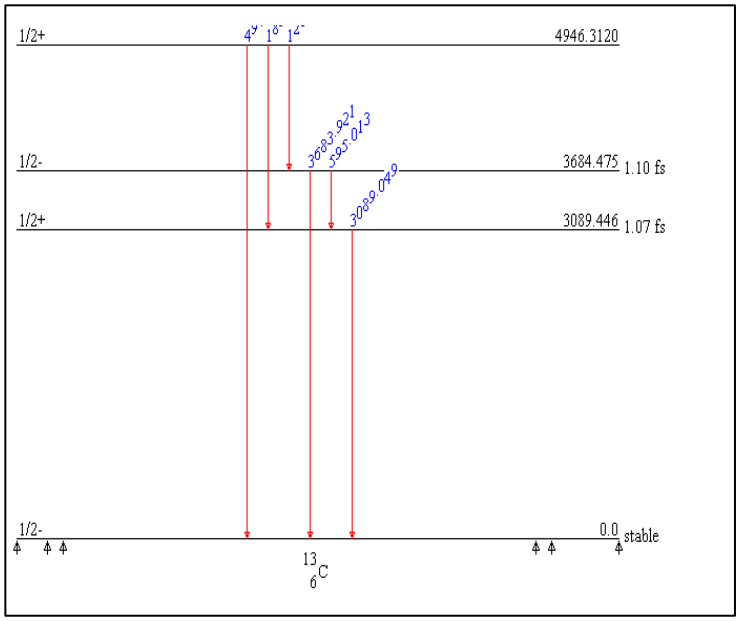

Fig. 3-2 C-13 Nuclear Structure

To produce gamma rays, energy level information is required; the starting level and ending level of each prompt gamma ray are also required. For gamma rays starting from the same energy level, the branching ratio is required. With all of this information available, gamma rays are produced and the final gamma ray spectrum is exactly the same as the one produced by the first method. The good point of using this method is that time information is maintained and prompt gamma rays are emitted dependently, which is the fundamental

physics behind it. The potential problem is that no absolute intensity information is used to produce gamma rays; only a branching ratio is used. If some prompt gamma ray information is missing (that is very possible for high atomic number elements), then the final prompt gamma ray spectrum will be inaccurate.

By default, GEANT4 uses the first method to produce gamma rays. All of the prompt gamma data are stored in G4NDL3.7 and are maintained under the directory of "/G4NDL3.7/Capture/FS". In this project, the second method is used. The nuclear structure data are calculated by Photon Evaporation model (GEANT4 Manual) and stored in PhotonEvaporation2.0.

A simple case is calculated by GEANT4 to test the GEANT4 model of producing prompt gamma rays. Sulfur-32 is the irradiation sample and its prompt gamma ray spectrum is displayed in figure 3-3. Three spectra are displayed in total.

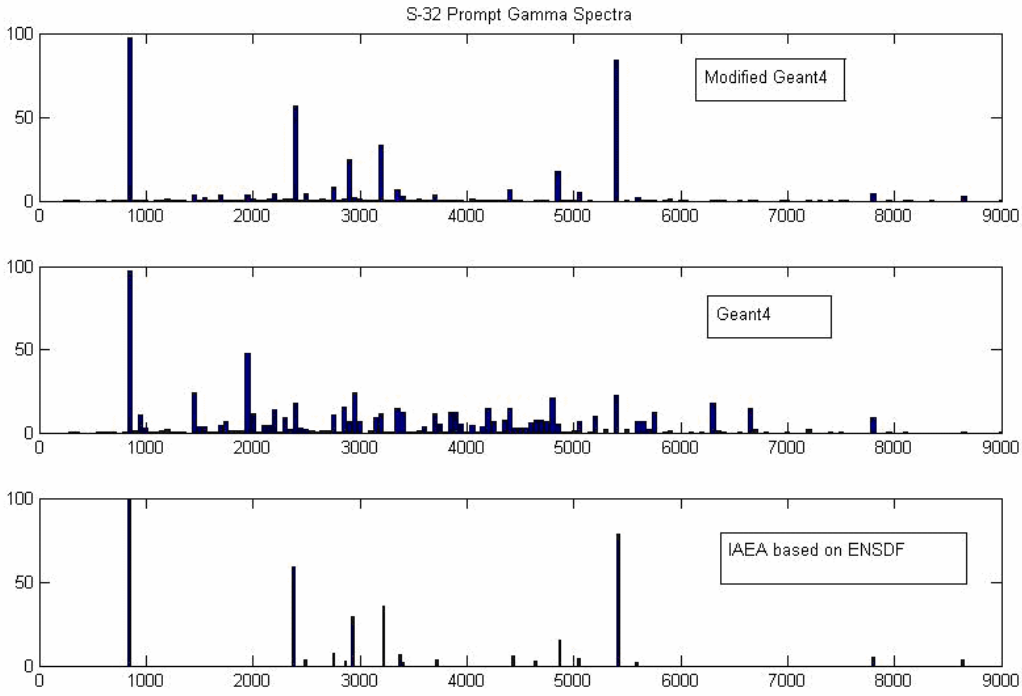

Fig. 3-3 S-32 Prompt Gamma-ray Spectrum

The lower one is displayed directly from the Evaluated Nuclear Structure Data File (ENSDF) (BNL, 2005), which is the standard. The middle one is the spectrum calculated by GEANT4. Obviously, it is totally wrong. The reason is that GEANT4 uses a certain theoretical model called the Photon Evaporation Model to simulate the neutron capture reaction. The Q-value of the neutron capture reaction is calculated based on the incident neutron energy. However, our common knowledge of a neutron capture reaction is that the Q-value is a fixed value. This difference causes the subsequent prompt gamma ray information to be totally wrong. Therefore, the GEANT4 neutron capture model is modified by fixing the Q-value and adding a new level of information into GEANT4 data libraries (Old Geant4 data libraries have all of the nuclear structure levels except the highest one, which is calculated by Geant4). After modification, the new sulfur prompt gamma ray spectrum is displayed in the upper figure, which matches the lower one very well.

An interface by GEANT4 is displayed in figure 3-4 to illustrate how GEANT4 simulates prompt gamma rays. In this case, four prompt gamma rays are emitted and in coincidence. After a large number of emissions, their intensity information also agreed with ENSDF.

3.3.3 Prompt Gamma Ray Yields

After the modification, GEANT4 has the ability to simulate prompt gamma-ray application by following nuclear structures. The next question is: What are the prompt gamma ray yields from each element in prompt gamma-ray imaging when a small animal is irradiated by thermal neutron beam? It is assumed that the basic compositions of small

animals are the same as human soft tissue, which is given in ICRU 44. The simulation geometry is shown in figure 3-5.

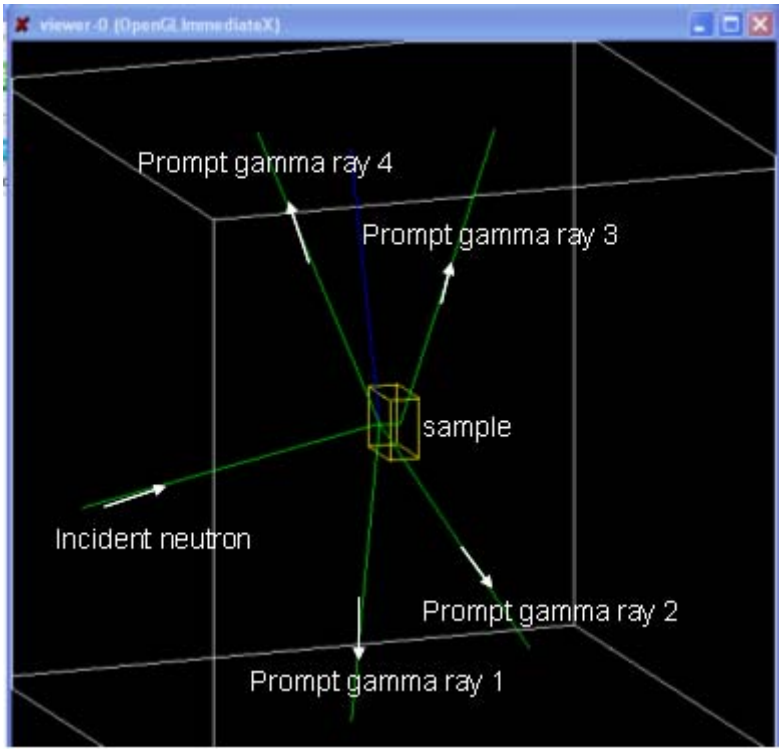

Fig. 3-4 Neutron Capture by GEANT4

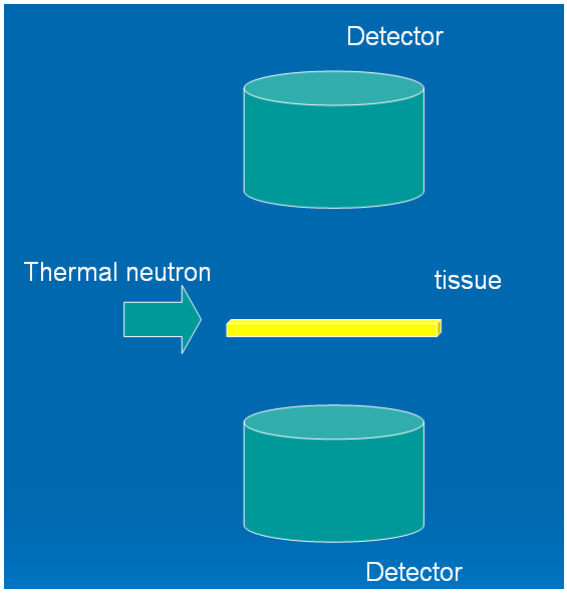

Fig. 3-5 Geometry to Calculate Prompt Gamma Ray Yields

The simulated results of yields are displayed in the below table 3-1.

Table 3-1 Prompt Gamma Ray Yields for Each element

Element	Z	WF	Q-value	σ (total)(b)	σ (capture)	Calculated	Simulated(A)	B
H	1	0.104472	2.22	20.5	0.332	14308	12485	16890
C	6	0.23219	4.95	4.95	3.37E-03	26.9	50	50
N	7	0.02488	10.80	12.2	7.47E-02	54.76	74	84
O	8	0.630238	4.14	4.01	2.70E-04	4.387	1	1
Na	11	0.00113	6.96	3.92	0.400	8.107	1	1
Mg	12	0.00013	7.33	3.47	6.30E-02	0.141	1	1
P	15	0.00133	7.94	4.36	0.180	3.186	5	1
S	16	0.00199	8.64	1.52	0.520	13.34	22	20
Cl	17	0.00134	8.58	50.4	33.2	524.4	755	779
K	19	0.00199	7.80	4.38	2.10	44.2	70	70
Ca	20	0.00023	8.36	3.46	0.430	1.02	0	2
Fe	26	0.00005	7.65	14.8	2.55	0.939	4	3

The new results of the number of captures (when 3% Hg is added) are displayed in the table below.

Hg	80	0.03	8.03	403	376	22811	20583	32214

In this simulation, the number of histories is 1 million. In the final application, these thermal neutrons are far from sufficient. It can be seen that hydrogen has a very high prompt gamma ray yield, caused by its large concentration in organic bodies. Hydrogen's prompt gamma rays may be measured to provide useful information about neutron distribution inside the organic body. Prompt gamma rays from chlorine are also relatively high. Prompt gamma rays from iron are very few. This is mainly caused by its low concentration. Mercury has a very high thermal neutron capture cross-section. Even though a very low mass fraction of mercury exists in the organic body, its prompt gamma rays are still very strong. This makes mercury very suitable to be imaged in prompt gamma ray imaging applications. Our following simulations are mainly focused on how to measure prompt gamma rays from mercury to get a concentration distribution of mercury.

3.3.4 Visualization by GEANT4

GEANT4 has very powerful visualization capability. The following figure 3-6 is my simulation geometry and is displayed by GEANT4.

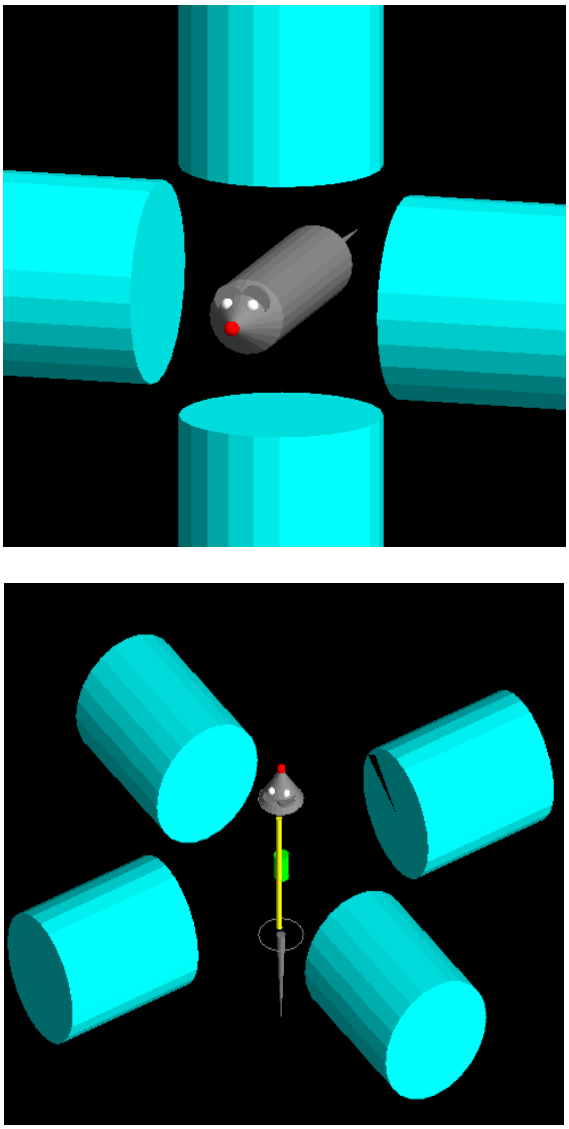

Fig. 3-6 Simulation Geometry by GEANT4

So far, prompt gamma rays have been produced for each element in simulation. We need to figure out a method of retrieving the images.

4. PROMPT GAMMA RAY EXPERIMENTS

Benchmark experiments are very important in Monte Carlo simulation codes design. Several experiments have been conducted for benchmarking purposes. Both single and coincidence experimental spectra are compared with simulated results.

4.1 Experiment Setup

Experiments were carried out on the Pulse Star research reactor at North Carolina State University. The basic experiment setup is the same for different samples and illustrated in figure 4-1.

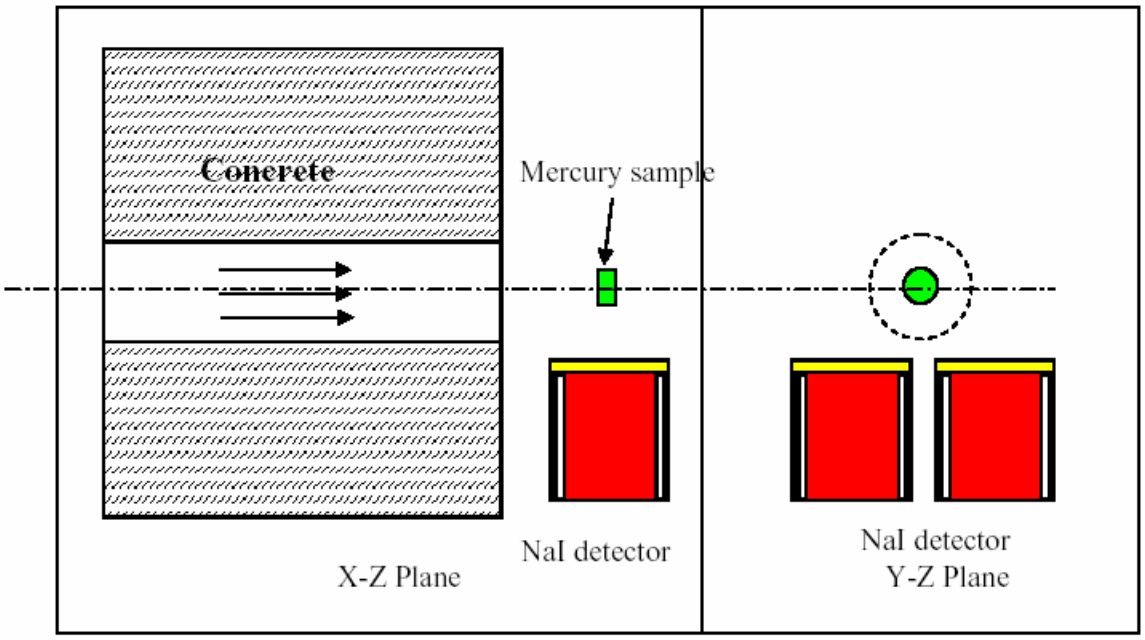

Fig. 4-1 Schematic of Experiment Setup

Two 6”×6” NaI detectors were placed under the irradiated samples. Both single and coincidence spectra were measured. The experimental electronic connection is illustrated in figure 4-2. Both the energy signal and the time signal were acquired from each detector. The energy signal came from the anode of PMT, and went through the preamplifier, the main amplifier, and finally the sparrow acquisition system. A single spectrum was recorded. The time signal came from the dynode of PMT, which is a little bit faster than the energy signal. If these two time signals are within a preset resolving time window, a coincidence gate signal is sent to the sparrow acquisition system and then the coincidence spectrum is recorded. For details on how to set up these electronics, see Matwally Ph.D. thesis (2003).

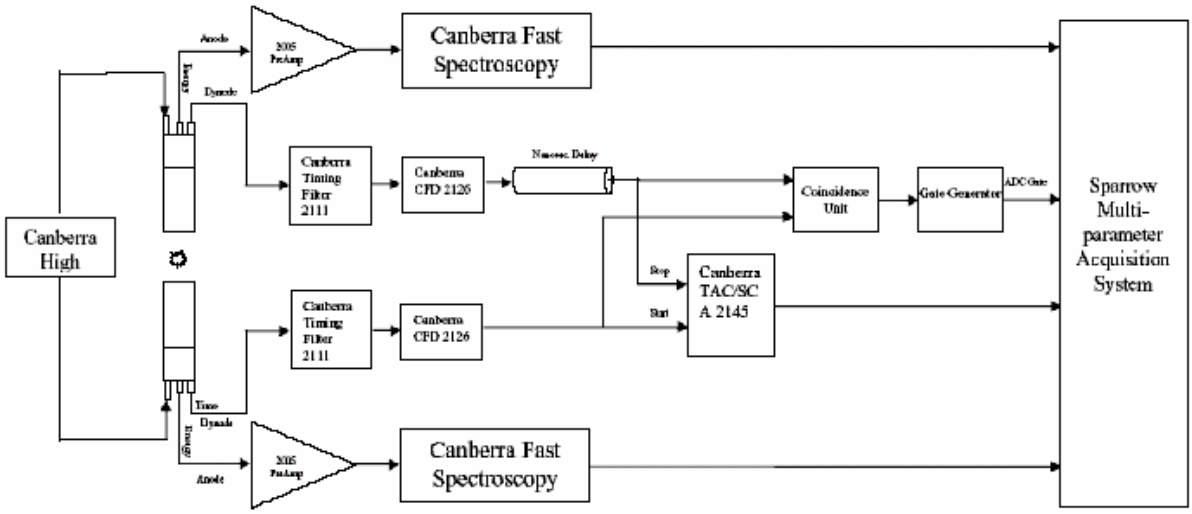

Fig. 4-2 Schematics of the Electronic Connection of two 6”×6” NaI System

4.2 Experiment 1— Pure Mercury Sample

Basic information about mercury is listed in table 4-1 below. Almost 94.5% of prompt gamma rays come from Hg-199. The Q-value of $^{199}Hg(n,r)^{200}Hg$ is 8.028Mev.

Table 4-1 Basic Information about Mercury

Isotope	θ*(%)*	σ_{γ}^{Z}(b)
Hg-196	0.15(1)	3190(180)
Hg-198	9.97(20)	2.0(3)
Hg-199	16.87(22)	2150(50)
Hg-201	13.18(9)	5.7(12)
Hg-204	6.87(15)	0.43(10)

4.2.1 Experimental Results

The experiment setup is displayed in figure 4-1. The reactor power was 100KW. The acquisition time was 5 hours. The background spectrum was also measured when the neutron beam was open, but no mercury sample was placed there. Experimental spectra are displayed in figure 4-3.

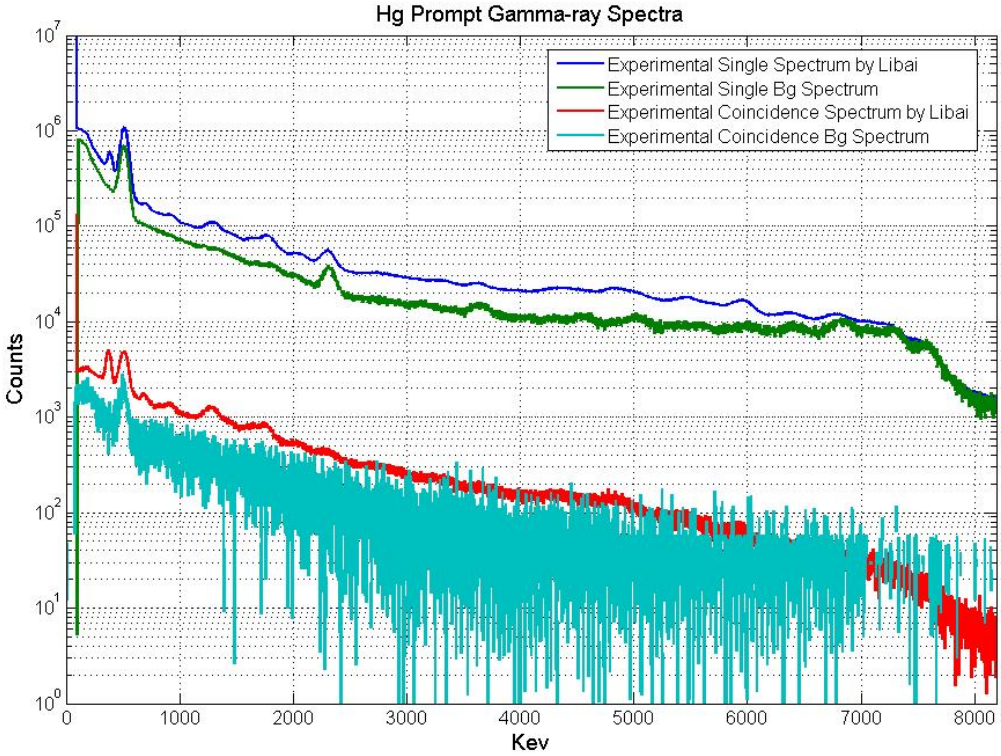

Fig. 4-3 Hg Experimental Prompt Gamma-ray Spectra

The background spectra were measured for only 5 minutes. The background counts shown in the figure above are the values derived after multiplying them by 60. Therefore, the statistical fluctuation is very poor, especially in the background coincidence spectrum. There were not too many background coincidence counts within 5 minutes. These experimental results are also compared with previous experimental results by Metwally (2003) and shown in figure 4-4.

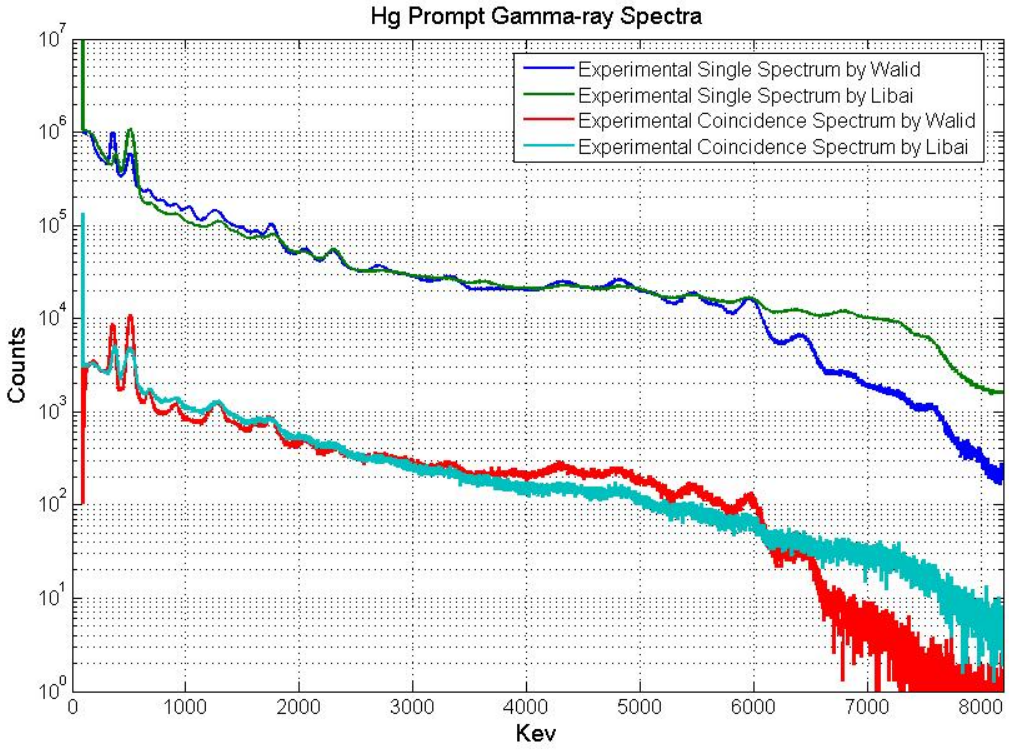

Fig. 4-4 Experimental Results of Libai Xu and Walid Metwally (Metwally 2003)

Metwally's results have a better resolution than our results. The possible reason is that the current experimental environment is not as good as the one before. A new neutron shielding room has been built around the neutron beam as a neutron imaging facility. The gamma background is much higher inside that room than in the one before, which was a spacious room.

4.2.2 Monte Carlo Modeling

Both GEANT4 and MCNP5 are used to simulate mercury prompt gamma ray spectra. Only Hg-199 is considered in the sample. For Geant4, we checked that the production of the prompt gamma rays of Hg-199 was corrected. For MCNP5, the prompt gamma ray data for mercury are also included and are shown in table 4-2 below; its resulting prompt gamma-ray spectra are displayed in figure 4-5 below.

Table 4-2 Mercury Nuclear Data by MCNP5

GPD "yes" means that photon-production data are included; "no" means that such data are not included.

ZAID	AWR	Library Name	Source	Eval Date	Temp (°K)	Length words	NE	E_{max} (MeV)	GPD	$\bar{U}$	CP	DN	UR
Z = 80 **********		Mercury	**********										
** Hg-nat**													
80000.40c	198.8668	endl92	LLNL	<1992	300.0	29731	2507	30.0	yes	no	no	no	no
80000.42c	198.8668	endl92	LLNL:X	<1992	300.0	29731	2507	30.0	yes	no	no	no	no
** Hg-196 **													
80196.24c	194.2820	la150n	LANL	1998	293.6	153206	1690	150.0	yes	no	yes	no	no
** Hg-198 **													
80198.24c	196.2660	la150n	LANL	1998	293.6	172481	3205	150.0	yes	no	yes	no	no
** Hg-199 **													
80199.24c	197.2590	la150n	LANL	1998	293.6	173336	4126	150.0	yes	no	yes	no	no
** Hg-200 **													
80200.24c	198.2500	la150n	LANL	1998	293.6	192339	2560	150.0	yes	no	yes	no	no
** Hg-201 **													
80201.24c	199.2440	la150n	LANL	1998	293.6	166179	3492	150.0	yes	no	yes	no	no
** Hg-202 **													
80202.24c	200.2360	la150n	LANL	1998	293.6	154736	1887	150.0	yes	no	yes	no	no
** Hg-204 **													
80204.24c	202.2210	la150n	LANL	1998	293.6	140754	832	150.0	yes	no	yes	no	no

For nature mercury, both 80000.40c and 80000.42c were tried, and they gave almost the same results, which are plotted by the blue line. For Hg-199, 80199.24c was tried, and its prompt gamma ray spectrum is plotted by the pink line. The yellow dots are from ENSDF, which is the standard prompt gamma-ray spectrum for Hg-199.

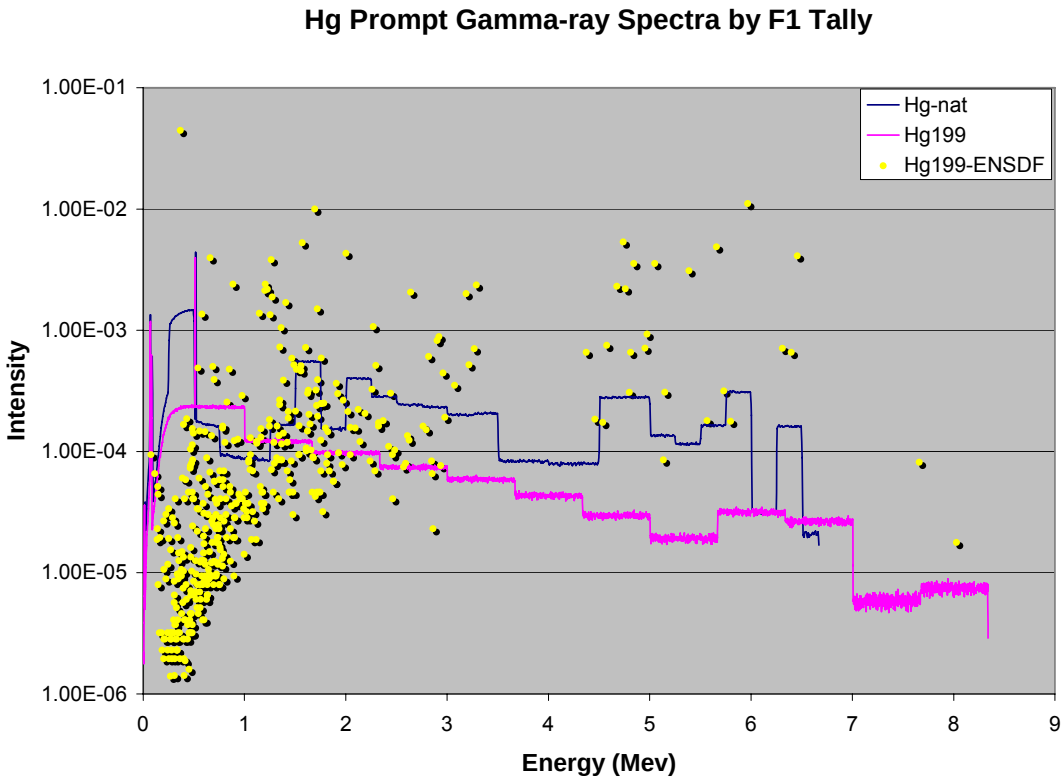

Fig. 4-5 Mercury Prompt Gamma Ray Spectrum by MCNP5

The mercury prompt gamma ray information in MCNP5 is appears incorrect (MCNP data libraries for prompt gamma-ray part have problems, the MCNP codes itself have no problems). At least, the prompt gamma ray energy should be distributed discretely, but not continuously.

In GEANT4 simulation, the simulation geometry is very close to the experiment. Only the thermal neutron with an energy of 0.025ev was simulated. The final energy deposition in each detector was recorded and post-processed by applying Gaussian broadening by Matlab. The simulated results are compared with experimental results and are displayed in figures 4-6 and 4-7.

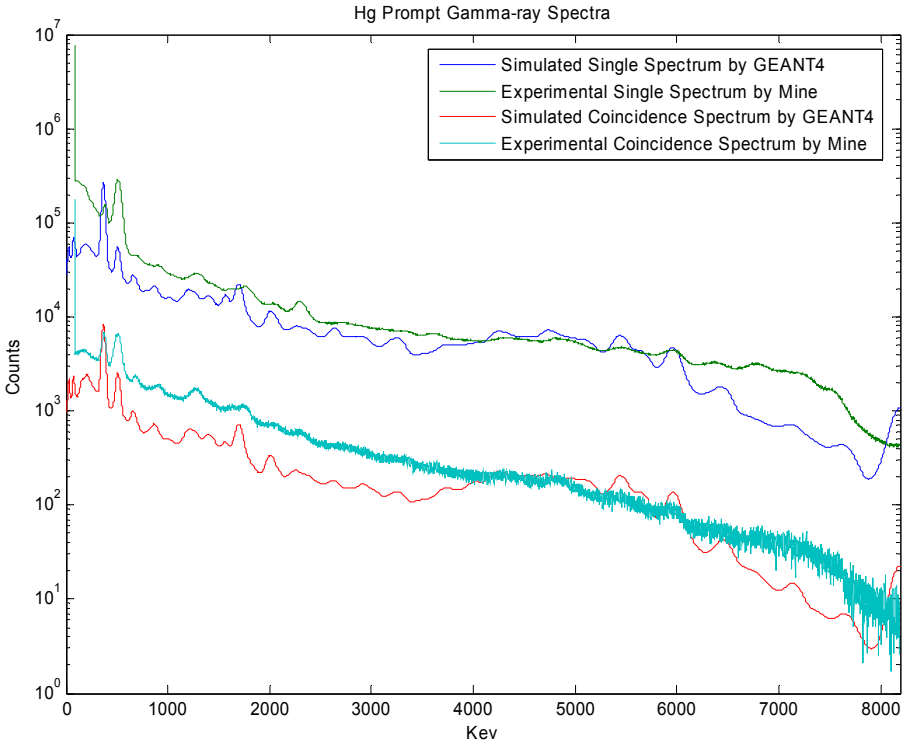

Fig. 4-6 Comparison Between Simulated Results and Libai's Experimental Results

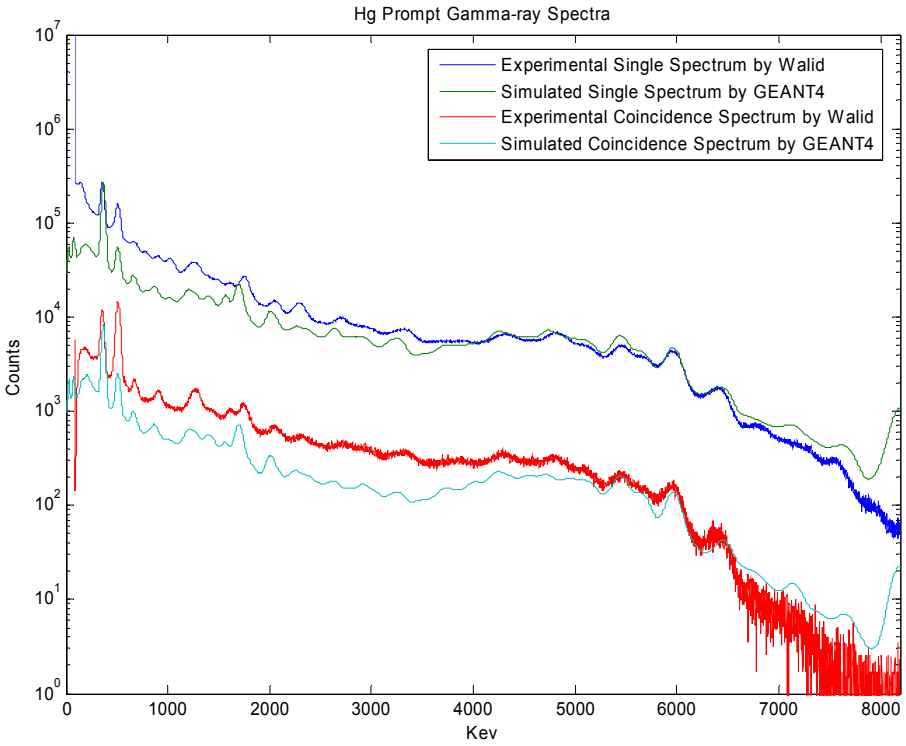

Fig. 4-7 Comparison Between the Simulated Results and Metwally's Experimental Results

The biggest difference between the simulated results and the experimental results is that there were more counts in the high-energy region in the simulated results than in the experimental results. The reason is that there was no gamma background in the simulation. Gamma background normally concentrates on low-energy regions. If we were to apply a gamma background to the simulated results, the new spectra would have higher counts in the low-energy region, which would make the total simulated spectrum much closer to the experimental spectra. The peak information between the simulated spectra and the experimental spectra are matched well in both high- and low-energy regions. In the middle, there are a few shifts. The reason is that the 0.511Mev and 5.967Mev peaks are used in spectra shifts. So the low- and high-energy regions are matched very well. In the middle regions, the simulated results did not consider the no-linear effect of NaI detectors.

The simulated results and experimental background spectra are used to do a library least-square fitting (Shyu et al. 1993). The fitting results are displayed in figure 4-8. Most peak information matched very well and the entire shape of the fitting spectra was also very good. Here, the coincident fitting results were not applied due to the high statistical error in the experimental coincidence background spectrum.

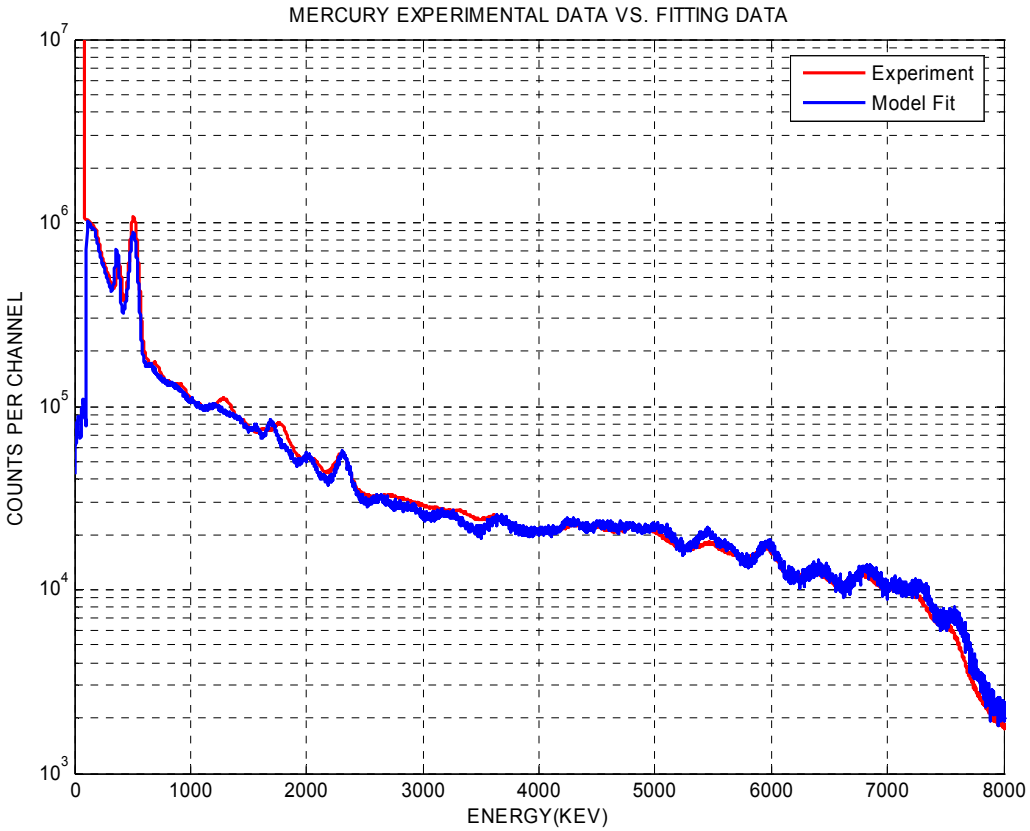

Fig. 4-8 The Fitting Results of Hg Prompt Gamma-ray Spectra

4.3 Experiment 2 – Pure Gd Sample

Basic information about gadolinium is listed in the table 4-3 below. Almost 81.5% of the prompt gamma rays are from Gd-157. The Q-value of $^{157}Gd(n,r)^{158}Gd$ is 7.937Mev. 18.5% of the prompt gamma rays are from Gd-155. The Q-value of $^{155}Gd(n,r)^{156}Gd$ is 8.536Mev.

Table 4-3 Basic Information of Gadolinium

Isotope	θ(%)	σ_{γ}^{Z}(b)
Gd-154	2.18(3)	85(12)
Gd-155	14.80(12)	60900(500)
Gd-157	15.65(2)	254000(800)
Gd-158	24.84(7)	2.2(2)
Gd-160	21.86(19)	1.4(3)

4.3.1 Experimental Results

The experiment setup is displayed in figure 4-1. The reactor power was 100KW. The acquisition time was 5 hours. The background spectrum was also measured when the neutron beam was open and no gadolinium sample was placed there. The experimental spectra are displayed in figures 4-9 and 4-10.

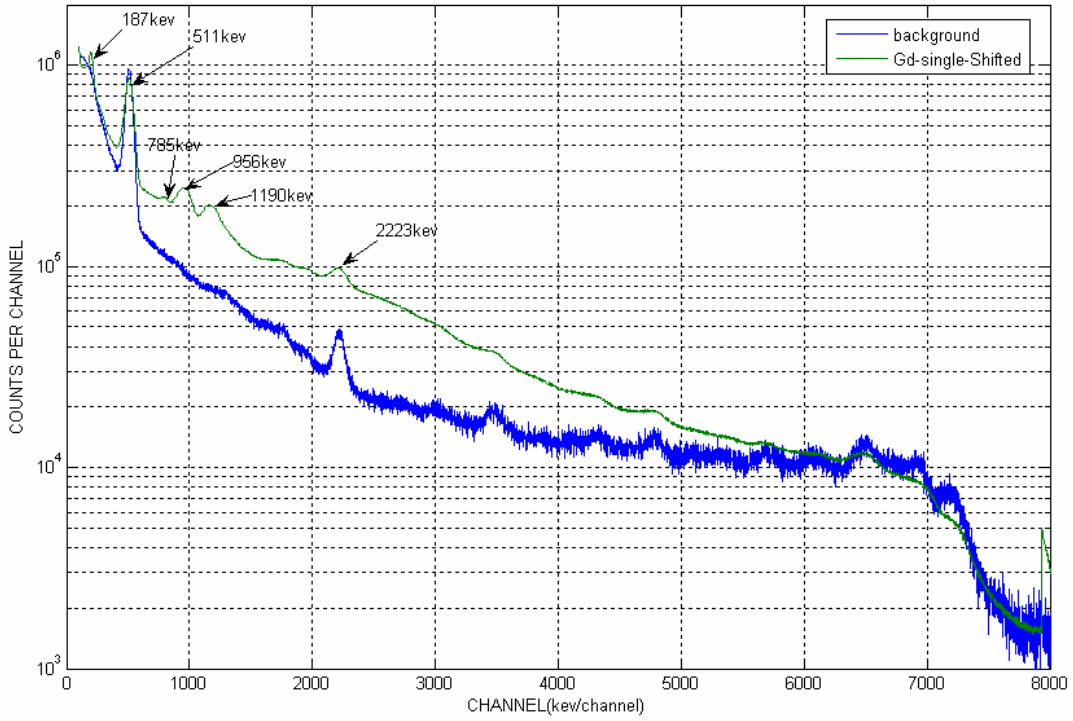

Fig. 4-9 Gd Experimental Prompt Gamma-ray Spectra

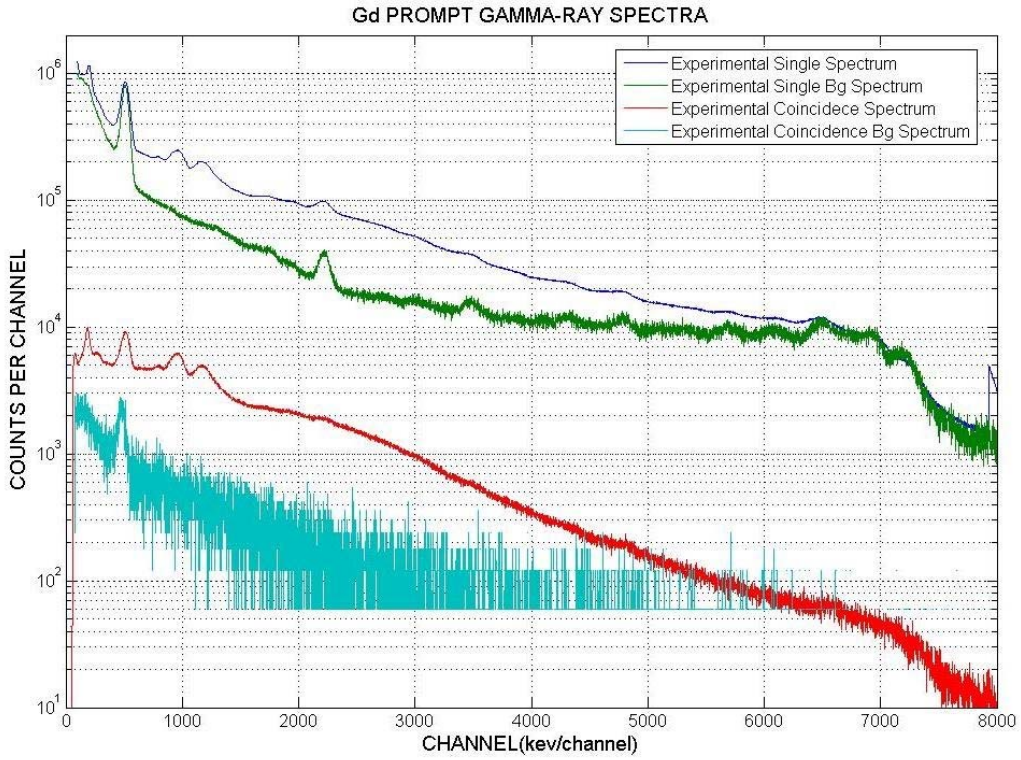

Fig. 4-10 Gd Experimental Prompt Gamma Ray Spectra

One obvious difference between the Gd spectrum and the Hg spectrum is that we do not see a lot of peaks in the high-energy region in the Gd spectrum, especially in the coincidence spectrum. That is actually the biggest difference between Gd and Hg. Relatively speaking, the Hg nuclear structure is simpler than the Gd structure. In the high-energy region, there were some peaks for Hg, and they were far apart. However, there were more peaks for Gd, and most of them were close to each other; no one was dominant so that, finally, not many Gd peaks appeared in the high-energy region.

4.3.2 Monte Carlo Modeling

Both GEANT4 and MCNP5 were used to simulate gadolinium prompt gamma ray spectra. Only Gd-157 was considered in the sample. For GEANT4, the nuclear structure of

Gd-157 was not complete, so we could not produce prompt gamma rays by following its nuclear structure. For MCNP5, the prompt gamma ray data for gadolinium are included (see table 4-4 below), and its produced prompt gamma ray spectra are displayed in figure 4-11 below.

Table 4-4 Gadolinium Nuclear Data by MCNP5

GPD "yes" means that photon-production data are included; "no" means that such data are not included.

ZAID	AWR	Library Name	Source	Eval Date	Temp (°K)	Length words	NE	E_{max} (MeV)	GPD	$\bar{U}$	CP	DN	UR
Z = 64 **********		Gadolinium	**********										
** Gd-nat**													
64000.35c	155.8991	rmccsa	LLNL	<1985	yes	7878	454	20.0	yes	no	no	no	no
64000.35d	155.8991	drmccs	LLNL	<1985	yes	6833	263	20.0	yes	no	no	no	no
** Gd-152 **													
64152.50c	150.6150	endf5u	B-V.0	1977	293.6	26251	3285	20.0	no	no	no	no	no
64152.50d	150.6150	dre5	B-V.0	1977	293.6	5899	263	20.0	no	no	no	no	no
64152.55c	150.6150	mise5xs[7,14]	B-V.0:T	1986	293.6	32590	3285	20.0	yes	no	no	no	no
64152.60c	150.6150	endf60	B-VI.0	1977	293.6	32760	4391	20.0	no	no	no	no	no
64152.65c	150.6150	endf66e	B-VI.4	1994	3000.1	263235	20777	20.0	no	no	no	no	yes
64152.66c	150.6150	endf66b	B-VI.4	1994	293.6	341562	29480	20.0	no	no	no	no	yes
** Gd-154 **													
64154.50d	152.5990	dre5	B-V.0	1977	293.6	5930	263	20.0	no	no	no	no	no
64154.50c	152.5990	endf5u	B-V.0	1977	293.6	49572	7167	20.0	no	no	no	no	no
64154.55c	152.5990	mise5xs[7,14]	B-V.0:T	1986	293.6	59814	7167	20.0	yes	no	no	no	no
64154.60c	152.5990	endf60	B-VI.0	1977	293.6	67662	10189	20.0	no	no	no	no	no
64154.65c	152.5990	endf66e	B-VI.4	1994	3000.1	218806	21530	20.0	no	no	no	no	yes
64154.66c	152.5990	endf66b	B-VI.4	1994	293.6	286357	31180	20.0	no	no	no	no	yes
** Gd-155 **													
64155.50c	153.5920	endf5u	B-V.0	1977	293.6	44965	6314	20.0	no	no	no	no	no
64155.50d	153.5920	dre5	B-V.0	1977	293.6	6528	263	20.0	no	no	no	no	no
64155.55c	153.5920	mise5xs[7,14]	B-V.0:T	1986	293.6	54346	6314	20.0	yes	no	no	no	no
64155.60c	153.5920	endf60	B-VI.0	1977	293.6	61398	9052	20.0	no	no	no	no	no
64155.65c	153.5920	endf66e	B-VI.0	1977	3000.1	62954	6748	20.0	no	no	no	no	yes
64155.66c	153.5920	endf66b	B-VI.0	1977	293.6	106795	13011	20.0	no	no	no	no	yes
** Gd-156 **													
64156.50c	154.5830	endf5u	B-V.0	1977	293.6	37371	3964	20.0	no	no	no	no	no
64156.50d	154.5830	dre5	B-V.0	1977	293.6	6175	263	20.0	no	no	no	no	no
64156.55c	154.5830	mise5xs[7,14]	B-V.0:T	1986	293.6	44391	3964	20.0	yes	no	no	no	no
64156.60c	154.5830	endf60	B-VI.0	1977	293.6	42885	5281	20.0	no	no	no	no	no
64156.66c	154.5830	endf66b	B-VI.0	1977	293.6	79827	7354	20.0	no	no	no	no	no
** Gd-157 **													
64157.50d	155.5760	dre5	B-V.0	1977	293.6	6346	263	20.0	no	no	no	no	no
64157.50c	155.5760	endf5u	B-V.0	1977	293.6	38975	5370	20.0	no	no	no	no	no
64157.55c	155.5760	mise5xs[7,14]	B-V.0:T	1986	293.6	47271	5370	20.0	yes	no	no	no	no
64157.60c	155.5760	endf60	B-VI.0	1977	293.6	56957	8368	20.0	no	no	no	no	no
64157.65c	155.5760	endf66e	B-VI.0	1977	3000.1	71857	8101	20.0	no	no	no	no	yes
64157.66c	155.5760	endf66b	B-VI.0	1977	293.6	99199	12007	20.0	no	no	no	no	yes
** Gd-158 **													
64158.50d	156.5670	dre5	B-V.0	1977	293.6	5811	263	20.0	no	no	no	no	no
64158.50c	156.5670	endf5u	B-V.0	1977	293.6	95876	15000	20.0	no	no	no	no	no
64158.55c	156.5670	mise5xs[7,14]	B-V.0:T	1986	293.6	113916	15000	20.0	yes	no	no	no	no
64158.60c	156.5670	endf60	B-VI.0	1977	293.6	59210	8909	20.0	no	no	no	no	no
64158.66c	156.5670	endf66b	B-VI.0	1977	293.6	152895	19903	20.0	no	no	no	no	no
** Gd-160 **													
64160.50d	158.5530	dre5	B-V.0	1977	293.6	5030	263	20.0	no	no	no	no	no
64160.50c	158.5530	endf5u	B-V.0	1977	293.6	53988	8229	20.0	no	no	no	no	no
64160.55c	158.5530	mise5xs[7,14]	B-V.0:T	1986	293.6	65261	8229	20.0	yes	no	no	no	no
64160.60c	158.5530	endf60	B-VI.0	1977	293.6	54488	8304	20.0	no	no	no	no	no
64160.66c	158.5530	endf66b	B-VI.0	1977	293.6	90407	11183	20.0	no	no	no	no	no

For natural gadolinium, both 64000.35c and 64000.35dc were tried, and they gave almost the same results, which are plotted by the blue line. For Gd-157, 64157.55c was tried, and its prompt gamma ray spectrum is plotted by the pink line. The yellow dots came from ENSDF, which is the standard prompt gamma ray spectrum for Gd-157.

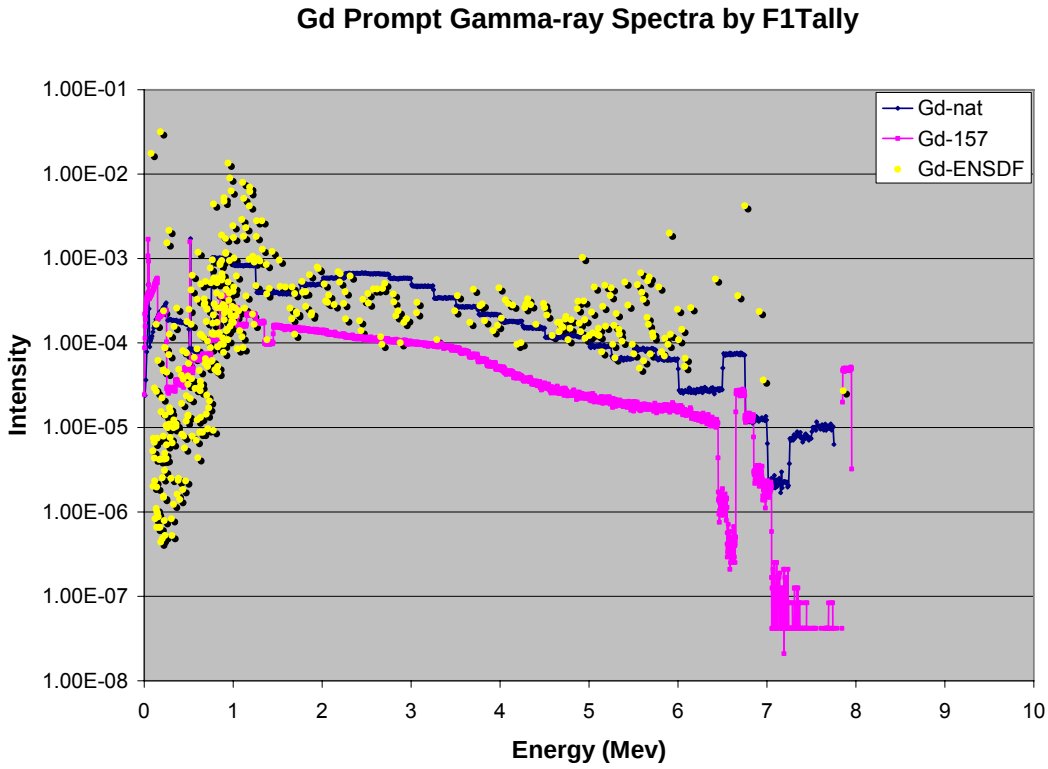

Fig. 4-11 Gadolinium Prompt Gamma-ray Spectrum by MCNP5

Similar to the mercury prompt gamma ray information by MCNP5, the gadolinium prompt gamma ray information appears incorrect. The information should be distributed discretely, but not continuously.

Several coincidence pairs of Gd-157 were picked out from its ENSDF, and displayed in table 4-5.

Table 4-5 Coincidence Pairs of Gd-157

Coincidence Pair	Coincidence Intensity (per 10000 captures)
6750.0 kev ----1187.1 kev	126
6750.0 kev ----1107.61 kev	148
5903.0 kev ---- 1010.0 kev ---- 944.2 kev	58
5903.0 kev------875.0 kev ----- 895.5---- 181.9	46
5903.0 kev------768.4 kev ------1186.0kev	33
181.9 kev ---- 79.5 kev	436
897.6 kev ---- 79.5 kev	70
944.2 kev ---- 79.5 kev	204
962.1 kev ----- 79.5 kev	130
1107.7 kev -----79.5kev	107
1186.0 kev ----79.5 kev	102
277.6 kev ---- 181.9 kev	113
780.2 kev ----- 181.9 kev	250
897.5 kev ----- 181.9 kev	327
915.0 kev ----- 181.9 kev	107
1097.0kev ---- 181.9 kev	180
1119.0 kev ----- 181.9 kev	312
1141.5kev ------181.9kev	170

The Q-value for Gd-157 is 7.937 Mev. From the above table, it can be seen that there are a lot of coincidence pairs for 79.5keV and 181.9keV gamma rays. The 79.5keV one is too low for the scintillation detector to detect. Therefore, the coincidence with181.9keV is our main concern. There is no one specific high-energy gamma ray (above 3Mev) which is in coincidence with 181.1keV and is much more intense than other high-energy gamma rays. There are a lot of high-energy gamma rays which are in coincidence with 181.keV to make the sum of gamma rays be the Q-value, but no one is more intense than the others. This complicates the detection of neutron-captured gamma-rays from Gd.

4.4 Summary

GEANT4 is used as the platform to simulate prompt gamma rays by following isotope nuclear structures. In this way, time information among prompt gamma rays is kept, and the coincidence technique can be simulated. A GEANT4-based simulated code is developed and benchmarked mainly by mercury experimental results. The simulated results agree with the experimental results very well. Currently, gadolinium cannot be simulated in GEANT4. The main reason is that gadolinium's nuclear structure data are not complete; prompt gamma rays cannot be produced by following its nuclear structures. Further efforts will be made to repair gadolinium's nuclear structure data libraries.

5. PROMPT GAMMA-RAY IMAGING

An image is a mapping over the space of some distribution, which in our case is that of prompt gamma emitters. Placing a position-sensitive detector directly before the emitting object is not enough to generate an image because any photon that is detected could be due to any part of the source. In this sense, no spatial information is obtained and it is impossible to produce an image. An imaging system must associate events with a place of emission.

Collimation is the technique used to build the relation between detected events and emission points. There are two kinds of collimations. One is called electronic collimation, such as the annihilation photons in PET; they are in an opposite direction. Once a coincidence is detected in a PET scanner, the emission point is assumed to be along the line that connects the two coincident detectors. A Compton camera also uses electronic collimation from the kinematics of Compton scattering to reconstruct position information of the emission points. The other is called mechanical collimation, such as the collimators in SPECT applications, which are usually made by lead.

Prompt gamma ray imaging is a case between PET and SPECT. Similar to PET, prompt gamma rays are emitted in coincidence once a single capture reaction occurs. Angular correlations (Evans, 1955) among prompt gamma rays do exist. The angle distributions among these prompt gamma rays are not as simple as PET, which are almost 180º. The angular correlation is tried as a kind of electronic collimation to reconstruct images by EM. If the coincidence among prompt gamma rays is not a factor, prompt gamma ray imaging is very similar to SPECT, just with various energies and normally higher energies. By using different kinds of collimators, it is possible to get prompt gamma ray images.

5.1 PET-like Trial

Coincidences among prompt gamma rays are taken into account, and used as an electronic collimation. Only γ- γ coincidences are considered.

5.1.1 Angular Correlation

In PET applications, the angle between the two annihilation photons is almost 180°. In PGI, angle distributions are controlled by the angular correlations of elements, which is one of the most important differences between PET and PGI. Equation 5-1 is the most common form for angular correlations.

$$w(\theta)d\Omega = (1 + a_2 \cos^2\theta + a_4 \cos^4\theta)d\Omega \qquad \text{Eq. (5-1)}$$

where θ is the angle between two coincident gamma rays, Ω is the solid angle subtended, and ω is the probability density function of that angle.

Three angular correlations are compared with PET. They are denoted by 'co' for ^{60}Co (a_2=1/8, a_4=1/24), 'isotropy' (a_2=0, a_4=0), and '-34' (a_2=-3, a_4=4). The corresponding angle distributions are shown in figure 5-1. The x axis represents the angle from 0° to 180°. The y axis is the probability at that angle. It can be seen that "co" and "isotropy" are quite similar to each other.

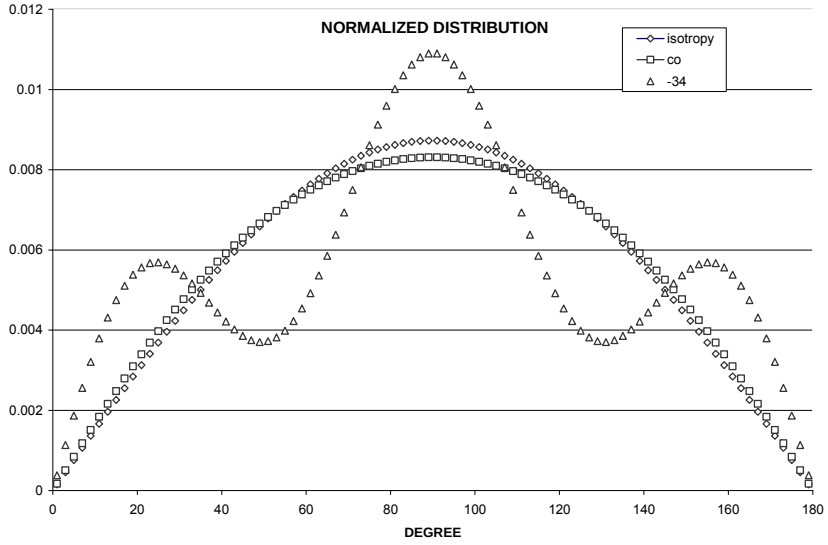

Fig. 5-1. Ideal Angle Distributions for “co”, “isotropy”, and “-34”

5.1.2. Image Reconstruction by EM

The Expectation Maximization (EM) (Shepp, 1982) algorithm is used to perform image reconstruction. EM is a general iterative method in mathematical statistics. It was first introduced into PET reconstruction algorithm by Shepp and Vardi in 1982. After 20 years in development, it has pretty much matured. The detailed EM algorithm in this work is referred to Kontaxakis, 1996.

5.1.3 Implementation

5.1.3.1 Phantom

A three-circle phantom (Kontaxakis, 1996) was used in the study. It is a two-dimensional slice with 3 areas of different activity levels of a circular shape, with a ratio of A:

B: C=1:2.5:4.5 for the areas A (background activity), B (low-activity area) and C (high-activity area). Figure 5-2 displays the phantom. The radius of the detector ring is 15cm. The width of the detector ring is 1cm. There are a total of 32 detectors. Every detector is regarded as an ideal detector. That means the efficiency is 100%. The object region is divided into a grid that is 32×32.

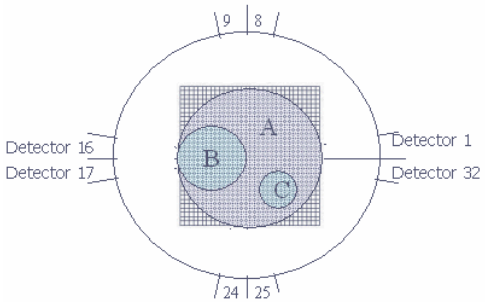

Fig. 5-2. Three-circle Phantom

5.1.3.2. Arrangement of the Measured Data

There are 32 detectors, so there are 496 detector pairs. For every coincidence event, there is one detector pair to record it. To show the results clearly, it is necessary to use a standardized approach to arrange the data. The approach used here is shown in figure 5-3.

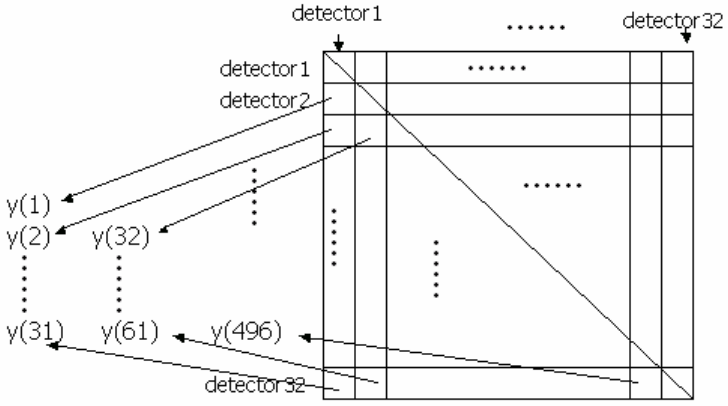

Fig. 5-3. Approach of Arranging Measured Data

Both the rows and columns in the figure represent detectors. The column index represents the detector number that detects one of two coincident gammas and the row index represents the detector number that detects the other. Note that the detector pair (1, 2) is the same as detector pair (2, 1), because we do not care about which one hits the detectors first. Therefore, only half of the matrix is used—that is, from y(1) to y(496).

5.1.3.3. Results for a Simple Point Source Model

A simple model is used to check the result. A point source is located at the center of the detector ring. The detected coincidence result is shown in figure 5-4

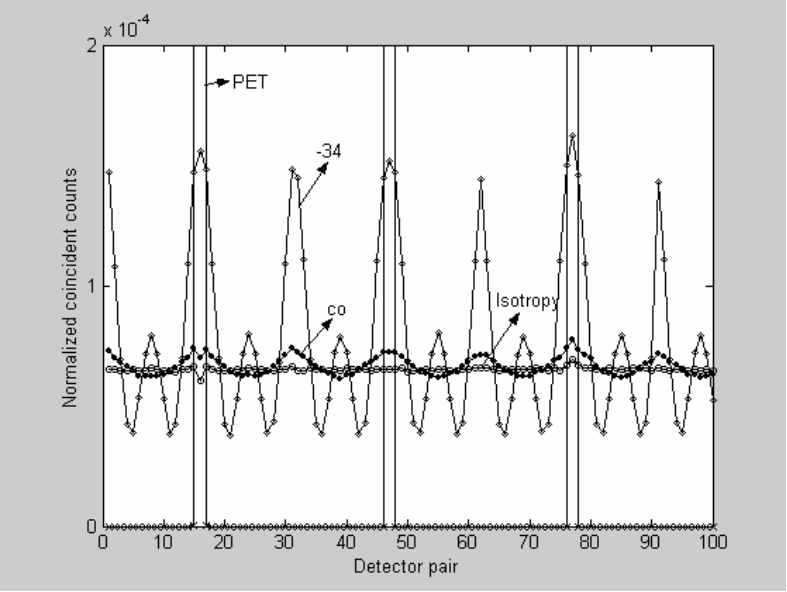

Fig. 5-4. Coincidence Distributions in Detector Pairs for the Simple Model

The horizontal axis represents the detector pair sequence (in order to show the figure clearly, only the first 100 detector pairs of 496 are shown). The vertical axis represents the normalized counts. The approach of arranging the sequence is shown in figure 5-3. Based on this approach, the first 31 detector pairs represent the sequence from the detector pair (1, 2) to the detector pair (1, 32). This is the order in which the angle between two coincident gamma rays changes continuously from 0° to 360°. This mimics the experiment in which the movable detector changes angles from 0° to 360°. The simulated results are the same as for ideal angular correlations, which can be obtained from equation 1. The results in figure 6 are normalized with respect to those for PET. The sums under the curves are 1, 0.032, 0.033, and 0.038, corresponding to 'PET', 'isotropy', 'co', and '–34', respectively. They are the relative detection efficiencies for coincidence events. Obviously, PET has the highest efficiency.

5.1.3.4. Results of the Three-Circle Phantom

A comparison based on the three-circle phantom between PET and PGI is shown in figure 5-5. The vertical axis is RMS (root mean square) error (Kontaxakis, 1996). It is a simple image quality indicator. The smaller the value is, the better the image quality. From the figure, we can see that PET has the fastest convergence rate and the best RMS error (all of these curves have reached their minimum values). Some acceleration has been applied to the 'isotropy' and 'co' data. In these cases, the acceleration can improve the convergence speed by about two times. Among the '-34', 'co', and 'isotropy' results, the '-34' result is better by a significant amount. 'Co' and 'isotropy' give almost the same results.

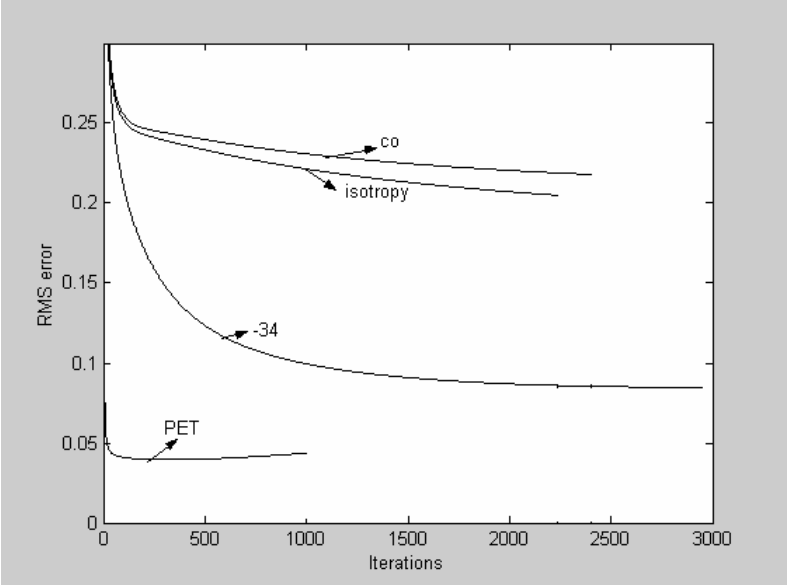

Fig. 5-5. Comparison Between PET and PGI

This simulation only takes into account the geometry effect. Prompt gamma ray energy information is not considered. Therefore, the difference between these results is due solely to the different angular correlations. It can be found that the distributions of coincidence data in figure 4-4 are quite different. This difference leads to the different convergence rates and different convergence values that were found for the RMS error.

5.1.3.5 Images for Three-Circle Phantom

The phantom image and the reconstructed images of each angular correlation are displayed in a 3-D mode in figure 5-6. The x axis and the y axis represent positions. The z axis represents the radioactivity level.

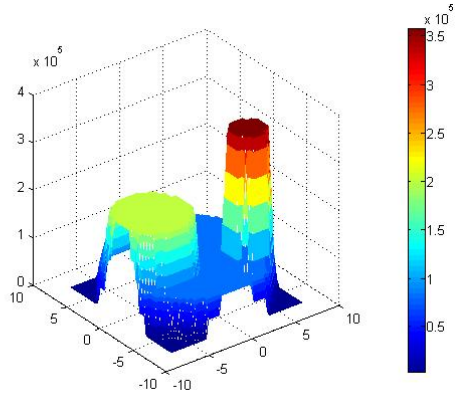

(a) Phantom

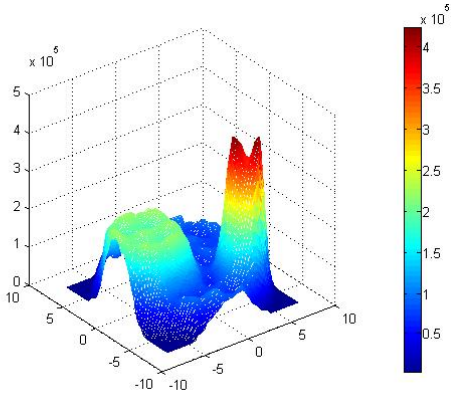

(b) Reconstructed image for PET

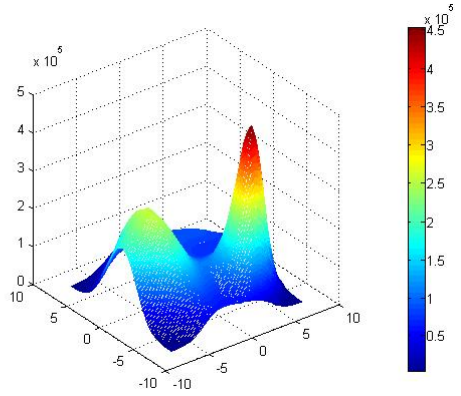

(c) Reconstructed image for “-34”

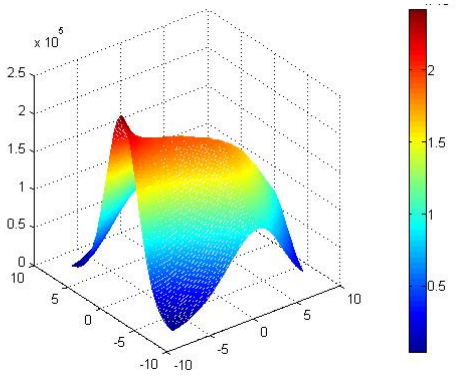

(d) Reconstructed image for “co”

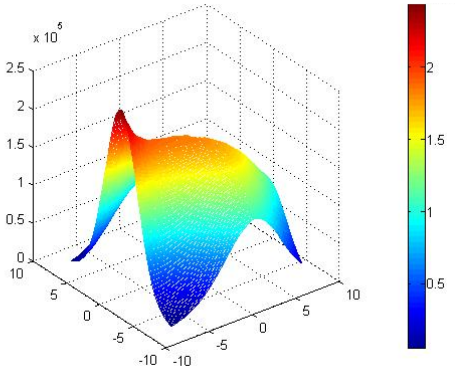

(e) Reconstructed image for “isotropy”

Fig. 5-6 Reconstructed Images

5.1.3.6 Conclusions

The present study concentrated on the effect of angular distribution and indicates that the higher the degree of angular correlation, the better the ability to use it in imaging. (The '-34' case is representative of the maximum angular correlation that is likely to be encountered. For example, Hg has this type of angular correlation.) Compared with the prompt gamma rays for the various angular correlations, PET has the highest detection efficiency, the fastest convergence rate, and the smallest RMS error when using the present model and geometrical simulation. For the detection efficiency: If the absolute detection efficiency for PET is d%, the absolute detection efficiency for the 'isotropy' method is almost $(d\ \%)^2$. The detection efficiency for 'co' and '-34' lies between these two. For the convergence rate: The development of computer techniques and the realization of special algorithms aimed at accelerating the EM can improve it significantly. For the RMS error: It is determined by the EM approach and the specific angular correlation. From the results of the geometrical simulation, PET was found to be better than the others in this aspect, but at present the prompt gamma-ray energies have not been considered. If spectrometry is used so that the prompt gamma-ray energies will also give additional information, it is likely that the PGI approach will improve considerably in relation to the PET case. The '-34' case probably will have the most potential among the cases involving angular correlation.

5.2 SPECT-Like Trial

If the coincidences among prompt gamma rays are not considered, PGI is very similar to a SPECT application from the perspective of imaging. Therefore, the collimators used in SPECT can also be used for imaging here. There are basically four kinds of collimators, as shown in figure 5-7. For small animal applications, a pinhole is widely used to achieve high resolution and high sensitivity at the expense of a smaller field of view (Smith et al., 2003; MacDonald et al., 2001; Jaszczak et al., 1994). We first tried a pinhole in PGI.

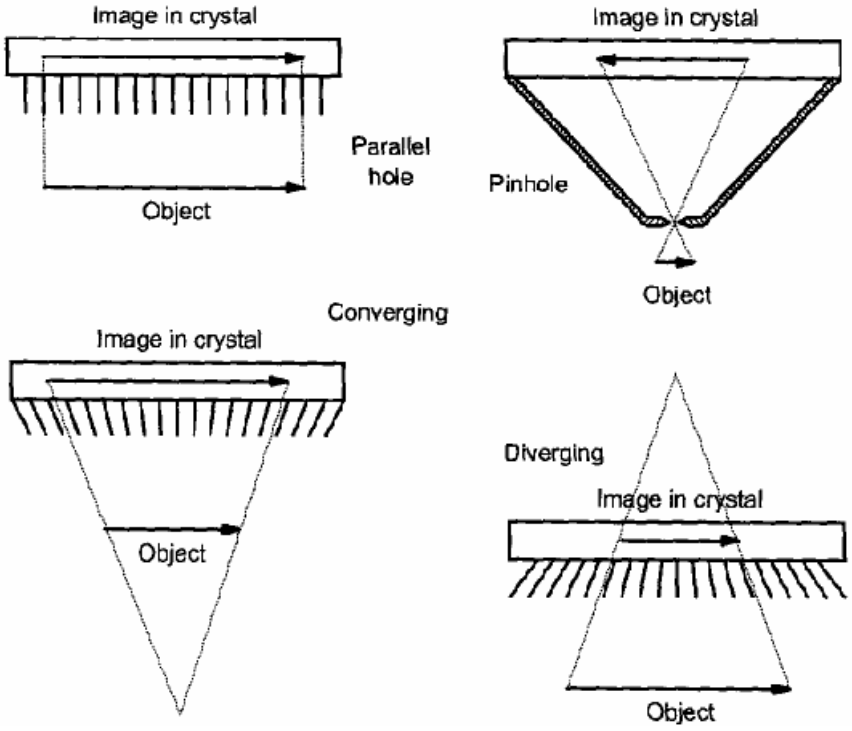

Fig. 5-7 Collimators Used in SPECT

5.2.1 Simulation Geometry

Simulation Geometry is visualized by GEANT4 in figure 5-8. The distance between the detector plane and the pinhole aperture is 8cm. The distance between the pinhole aperture and the object is 2cm. This is a 4-time magnification. The detector plane is a NaI detector with a cross-section of 10cm×10cm and a thickness of 3cm. The coincidence detector is also a NaI detector with a radius of 3in. The pinhole is made of lead with a thickness of 4cm. The sample is made of soft tissue. The pinhole aperture geometry is shown in figure 5-9.

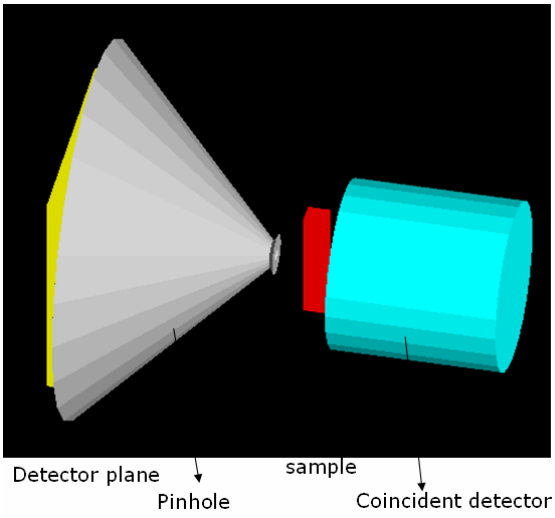

Fig. 5-8 Imaging Geometry in Simulation

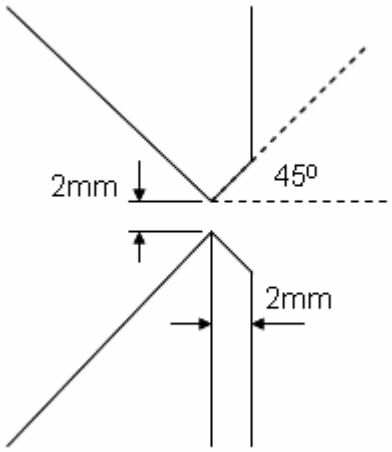

Fig. 5-9 Pinhole Aperture Geometry

5.2.2 Sample in Simulation

A 3mm×3mm×3mm cubic mercury block was placed on the sample, as shown in figure 5-10. The center of the block is 5mm above the center line of the detector plane and the pinhole aperture.

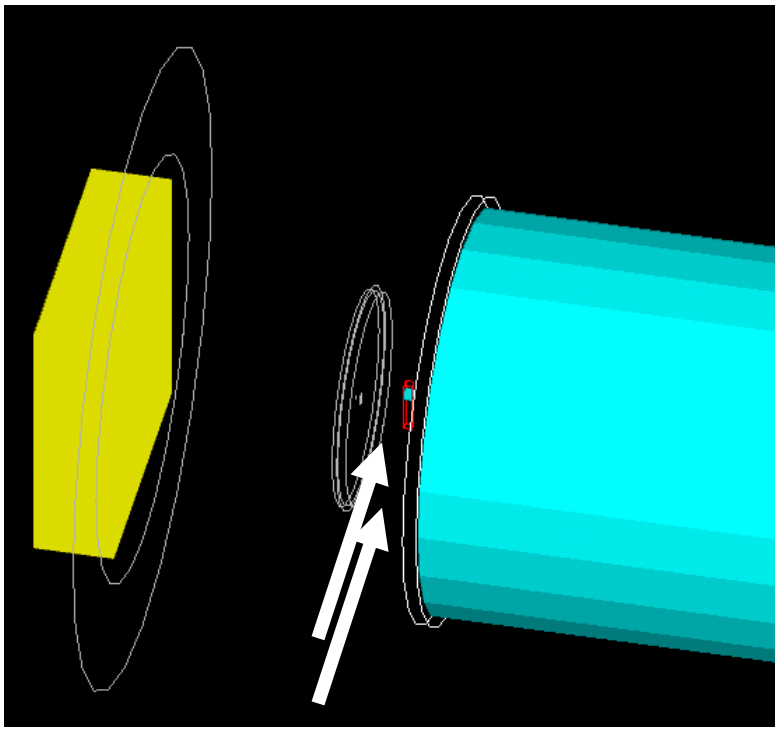

Fig. 5-10 An Example for SPECT-like Trial

A parallel thermal neutron beam irradiated the sample, as illustrated by the white arrows.

5.2.3 Simulation Results

A prompt gamma-ray spectrum from Hg-199 is displayed in figure 5-11. Not all these gamma rays are measured to identify mercury. The 370keV gamma ray has the largest intensity, around 0.8 per capture reaction. First, we used 370keV gamma ray to get images.

This means once the energy deposition in the detector plane was around 370keV, the position information of that event was recorded and displayed in figure 5-12.

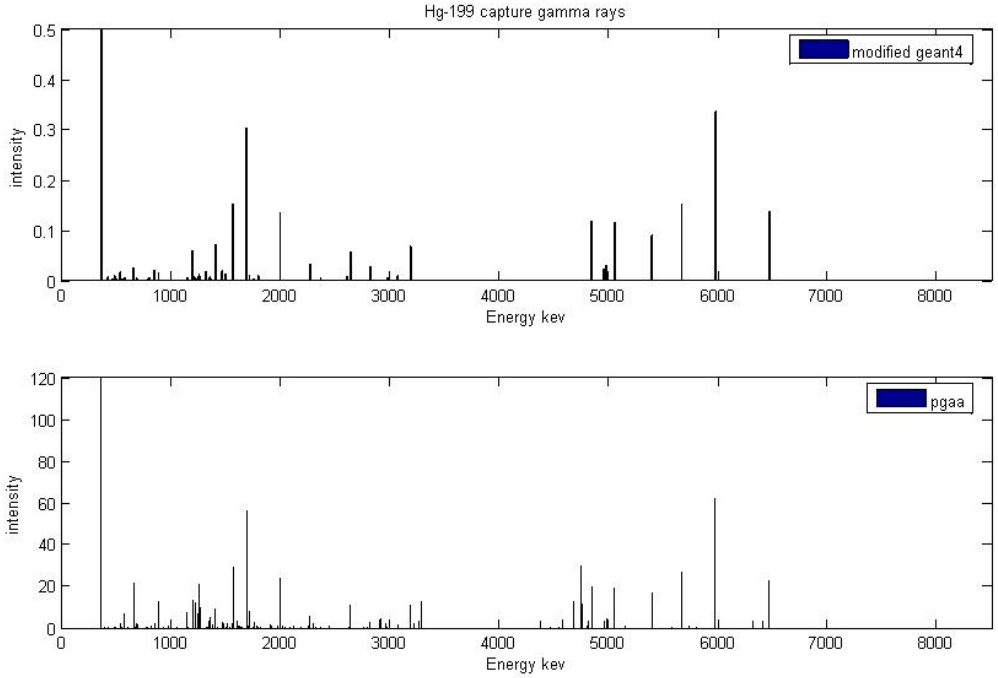

Fig. 5-11 Prompt Gamma-ray Spectrum from Hg-199

Secondly, we used prompt gamma rays with energy above 6Mev to get images. Once the energy deposition in detector plane was larger than 6Mev, the position information of that event was recorded and displayed in figure 5-13. The units of axis in both figures 5-12 and 5-13 are mm.

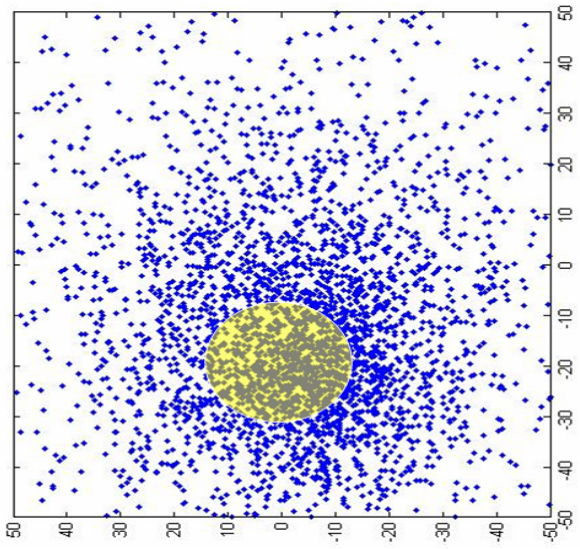

Fig. 5-12 370kev Prompt Gamma-ray Imaging

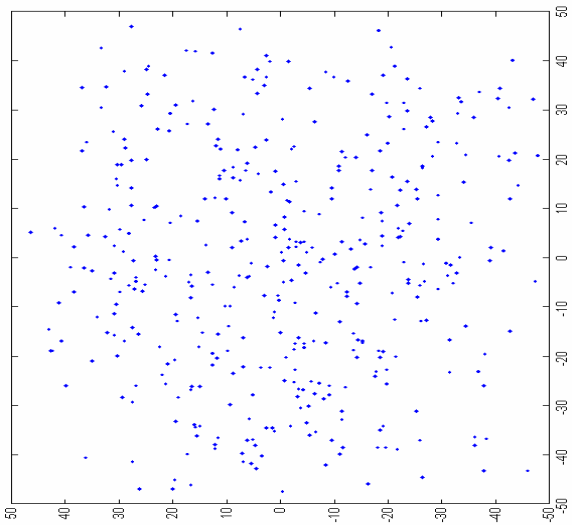

Fig. 5-13. 6Mev and Above Prompt Gamma-ray Imaging

In figure 5-12, the yellow circle signifies the ideal position distribution of 370 prompt gamma rays. It can be derived from the system geometry and sample size. The simulated result is more dispersive than the derived results. The main reason is the knife-edge effect that happens in SPECT. The aperture edge is not thick enough to stop gamma rays as it is supposed to do. In figure 5-13, no patterns can be recognized due to the same reason. 6Mev gamma rays have stronger penetration ability than 370keV gamma rays. The pinhole doesn't work at all.

6. RELATED CRITICAL TOPICS

6.1 Absorbed Doses to Small Animals

To evaluate this new imaging approach, the absorbed dose for small animals caused by thermal neutrons was investigated. Based on this knowledge, the maximum allowed thermal neutron flux may be determined, which can be used further to estimate both PGI and neutron tomography imaging quality. However, very little research has concentrated on imaging mice with thermal neutrons, and even fewer for the absorbed dose for mice. A lot of knowledge about neutron-induced doses in relation to the human body has accumulated. The common method to calculate the neutron dose for the human body is to use the flux-to-dose conversion factor (Bozkurt, 2000; Knoll, 1999) or the Monte Carlo simulation. By using a conversion factor time neutron flux, it is very convenient to obtain the absorbed dose or the equivalent dose for the human body and for each organ. However, considering the difference between the human body and mice, it is not accurate to use the same conversion factor directly on mice. Consequently, the Monte Carlo simulation is used, which is also the method to calculate the flux-to-dose conversion factor for the human body, the flux-to-dose conversion factor for mice, and moreover, the whole body's absorbed dose for mice. The whole body's absorbed dose—instead of the effective dose —is calculated to simplify the consideration of the mouse organ weighting factor.

6.1.1 Methods

1) Method I: MCNP5

Basically, there are three methods in MCNP5 to calculate absorbed doses. 1) F4 tally and FM card, which should be the flux-to-dose conversion factor for mice. 2) F6 tally. 3) F8 tally. Both F6 and F8 tallies were tried for this case. The difference between them is around 10%, which is acceptable for a preliminary study. And finally, according to Bozkurt et al. (2000), MCNP5 and F6 tally are used to calculate the absorbed dose in the unit of energy deposition per mass. A cylinder with a height of 10cm and a radius of 1cm is used to represent a mouse. The mouse composition is simplified as soft tissue. The elemental composition of soft tissue is from the four-component model (ICRU FOUR-COMPONENT), shown in table 6-1. Its density is 1.0 g/cm^3. The MCNP5 simulation geometry is shown in figure 6-1.

Table 6-1 Four Component Model for Soft Tissue

COMPOSITION:	
Atomic number	**Fraction by weight**
1	0.101172
6	0.111000
7	0.026000
8	0.761828

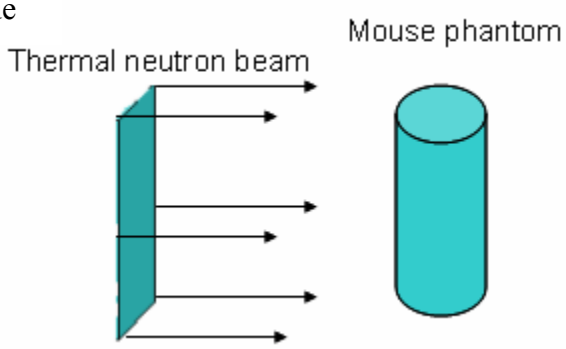

Fig. 6-1 MCNP Simulation Geometry

The source is a parallel thermal neutron beam with a cross section of 2cm×10cm. The neutron flux is 10^6n/cm^2 s. The neutron is monotonic in energy, which is 0.0025ev.

2) Method II: Dose Estimate By Hand Calculation

To investigate the detailed dose contribution from each element (MCNP5 cannot sort the absorbed dose by elements), and if a rough estimate is not too difficult to do by hand, a hand calculation is made. The neutron-absorbed dose is mainly caused by neutron capture reactions when the incident neutrons are thermal neutrons, and can be expressed in the following equation 6-1 for each element:

$$D = \frac{\Phi N \sigma E}{\rho} \qquad \text{Eq. (6-1)}$$

where φis thermal neutron fluence (n/cm^2), N is the atom density of that element (/cm^{-3}), σis the capture cross-section for each element, E is energy from the capture reaction for each element, andρis the object density. By summing the absorbed doses over each element, the total absorbed dose is obtained. The only unknown parameter in the above formula is E, which is calculated in the following way. For thermal neutron applications to biological objects, the important capture reactions are (n, γ) reactions and ^{14}N (n, p) ^{14}C, which is shown below:

The major thermal neutron capture reactions in tissue

$^{14}N(n,p)^{14}C$ $\sigma = 1.7$ barns $Q = 0.626$ MeV

$E_p = 0.58$ MeV, range in water ~ 8 μm
$E_C = 0.04$ MeV
Energy is deposited locally

For (n, γ) reactions, according to Faw (1999), we can calculate how many prompt gamma rays are emitted in one capture reaction for every element, and derive a simple energy distribution for them. Then, by using MCNP5, we can get the energy deposition of every gamma ray in the mouse phantom by assuming that these gamma rays are uniformly emitted over the phantom and are emitted in isotropy. Table 6-2 below shows the number of gamma rays produced by one capture reaction for each element of the mouse phantom, the energy distribution, and the MCNP calculated energy deposition for each gamma ray.

Table 6-2 Prompt Gamma Rays Caused by Different Elements

Prompt gamma E(Mev)	Energy deposition (keV)	Numbers of Gamma Rays Produced per Capture			
		O	C	N	Hg
0.5	22.9	1		0.2632	0.9153
1.5	59.5	0.82	0.2953	0.3716	0.3383
2.5	84.6	0.82		0.2450	0.2106
3.5	106.0	0.18	0.321	0.2819	0.1322
4.5	124.6		0.6764	0.1573	0.2744
5.5	140.5			0.8031	0.3008
6.5	155.8			0.2064	0.0698
7.5	173.2			0.1019	
8.5	191.3			0.0397	
9.5	207.5			0.0222	
10.5	224.3			0.1412	
Total Energy deposition per capture (keV)	N/A	160.1	135.9	302.5	159.0

For hydrogen, the prompt gamma ray energy is 2.22Mev. The calculated energy deposition is 78.5keV per capture.

The energy deposition per capture reaction for each element was obtained, and it would be very easy to estimate how many capture reactions take place during PGI for each element. Then the absorbed dose caused by each element can be estimated.

6.1.2 Results

1) Results of Method I

The averaged absorbed dose to the mouse phantom by MCNP5 is 1.44950E-04 Mev/gram per incident neutron, with a relative error of 0.0035.

Changing the unit to Gy:

$$\frac{1.4495\times10^{-4}\,Mev}{gram}=\frac{1.4495\times10^{-4}\times1.6\times10^{-19}\times10^{6}\times10^{3}}{10^{3}\,grams}=2.32\times10^{-14}\,Gy$$

Normalized by unit neutron flux (1 neutron per cm^2), we can get the flux-to-dose conversion factor for the mouse phantom:

$$2.32\times10^{-14}\,Gy\times20cm^{2}=0.464\,pGy\bullet cm^{2}$$

Considering a practical case, if the neutron flux is $10^6/cm^2s$ and the scan time is 30min, the total absorbed dose will be:

$$0.464\,pGy\bullet cm^{2}\times10^{6}\,cm^{-2}\bullet s^{-1}\times1800s=0.8352mGy$$

If 1% Hg is added to the mouse composition, the new absorbed dose will be as follows:

The averaged absorbed dose will be 2.50971E-04 Mev/gram per incident neutron, with a relative error of 0.0049.

$$\frac{2.5097\times10^{-4}\,Mev}{gram}=\frac{2.5097\times10^{-4}\times1.6\times10^{-19}\times10^{6}\times10^{3}}{10^{3}\,grams}=4.01\times10^{-14}\,Gy$$

Normalized by unit neutron flux (1 neutron per cm^2):

$$4.01\times10^{-14}\,Gy\times20cm=0.802\,pGy\bullet cm^{2}$$

If the neutron flux is $10^6/cm^2s$ and the scan time is 30min, the total absorbed dose is:

$$0.802\,pGy\bullet cm^{2}\times10^{6}\,cm^{-2}\bullet s^{-1}\times1800s=1.44mGy$$

Then, the total absorbed dose caused by mercury is:

1.44mGy-0.8352mGy= 0.60mGy

This value is close to the absorbed dose caused by the mouse body itself.

2) Results of Method II:

The mass of the mouse phantom is 31.4g.

The number of (n, γ) captures for H:

(31.4g)×0.101÷(1.67×10^{-24} g/atoms) ×0.33×10 $^{-24}$ cm^2 /atom×10^6 cm^{-2}s^{-1} ×1800s=1.13 × 10^9 captures

The number of (n, γ) captures for O:

(31.4g)×0.762÷(16×1.67×10^{-24} g/atoms) ×0.00019×10 $^{-24}$ cm^2 /atom×10^6 cm^{-2}s^{-1} ×1800s=3.12 × 10^5 captures

The number of (n, γ) captures for C:

(31.4g)×0.111÷(12×1.67×10^{-24} g/atoms) ×0.0035×10 $^{-24}$ cm^2 /atom×10^6 cm^{-2}s^{-1} ×1800s=1.10 × 10^6 captures

The number of (n, γ) captures for N:

(31.4g)×0.026÷(14×1.67×10^{-24} g/atoms) ×0.0747×10 $^{-24}$ cm^2 /atom×10^6 cm^{-2}s^{-1} ×1800s=4.70 × 10^6 captures

The number of $^{14}N(n, p)^{14}C$ for N:

$(31.4g)\times 0.026 \div (14\times 1.67\times 10^{-24}\ g/atoms) \times 1.70\times 10^{-24}\ cm^2/atom \times 10^6\ cm^{-2}s^{-1} \times 1800s = 1.07\times 10^8$

The number of (n, γ) captures for Hg:

$(0.314g) \div (200\times 1.67\times 10^{-24}\ g/atoms) \times 376\times 10^{-24}\ cm^2/atom \times 10^6\ cm^{-2}s^{-1} \times 1800s = 6.3\times 10^8$

Then, the absorbed dose caused by each element can be calculated.

By (n, γ) capture of H, C, O, and N:

$$D_{H,C,O,N} = \sum_{H,C,O,N} Number(Captures) \times \frac{E(per\_Capture)}{mass(mouse)}$$
$$= 1.13\times 10^9 \times \frac{0.0785Mev}{31.4g} + 3.12\times 10^5 \frac{0.16Mev}{31.4g} + 1.10\times 10^6 \times \frac{0.136Mev}{31.4g} + 4.7\times 10^6 \frac{0.3Mev}{31.4g}$$
$$= 0.45mGy$$

By $^{14}N(n,p)^{14}C$:

$$D_{n\_p} = Number(N\_P) \times \frac{E_P}{mass(mouse)} = 1.07\times 10^8 \times \frac{0.626Mev}{31.4g} = 0.34mGy$$

The total absorbed dose to the mouse phantom caused by itself is:

$$D_{H,C,O,N} + D_{n\_p} = 0.45mGy + 0.34mGy = 0.79mGy$$

Compared with method I's result, 0.8352mGy, they are matched very well.

Similarly, if 1% mercury is added, then:

The absorbed dose caused by (n, γ) capture of Hg is:

$$D_{Hg} = Number(Hg\_Capture) \times \frac{E(per\_Capture)}{mass(mouse)} = 6.3\times 10^8 \times \frac{0.159Mev}{31.4g} = 0.51mGy$$

Compared with method I's result, 0.6mGy, the match is not bad.

So finally, the total absorbed dose after 1% mercury is added is:

$$D = D_{C,H,O,N} + D_{n\_p} + D_{Hg} = 1.3mGy$$

From these results, we can estimate that the whole body's absorbed dose for the mouse phantom is around 0.81mGy (average of two methods). If 1% (in mass) mercury is added, an additional 0.55mGy will be induced. These results are obtained when the mouse phantom is irradiated by a $10^6/cm^2s$ thermal neutron beam in a 30min scan. According to Chow et al. (2001), the average CT dose for a mouse is 10cGy in a 3-D high-resolution X-ray CT system, MicroCAT (40kVp/0.500mmAl/250ms/400uA) (Chow, 2001). This dose is approximately 1% of LD50/30 for a mouse (9Gy), which is a measure of a lethal dose to 50% of the population after 30 days. According to another simple estimation for PET (Appendix C), if 100uCi ^{18}F is injected into the mouse phantom, the estimated absorbed dose is 52mGy. Therefore, the total of the whole body's absorbed dose for a mouse when imaged with a combined PET/CT system is about 152mGy. Compared with our simulation results, we can increase the neutron flux intensity by 100 times to optimize the neutron image quality from the point of the absorbed dose. Considering the different quality factors between neutrons and photons, we may not be able to increase neutron intensity that much. From ICRU60, the thermal neutron quality factor is 5, and the photon quality factor is 1. This results in the equivalent dose for a mouse when imaged with a thermal neutron beam with a flux of $2\times10^7/cm^2s$ in 30min to be equivalent to that which is imaged with a combined PET/CT system (for CT, 40kVp/0.500mmAl/250ms/400uA; for PET, 100uCi ^{18}F).

6.1.3 Conclusions

The Monte Carlo simulation is used to estimate the whole body's absorbed dose for a cylindrical mouse phantom. Although the phantom is very simple, it provides an initial estimate of the radiation exposure to small animals when they are imaged with a thermal neutron beam. Under our current parameters, a $10^6/cm^2s$ flux and a 30min scan, the absorbed dose is 0.81mGy, which is caused by the body itself and an additional 0.55mGy by an additional 1% of mercury. Compared with the absorbed dose of the current PET/CT application, we may increase the neutron flux by 100 times to get the best image quality if the different quality factors between neutrons and photons are not considered. A more detailed and accurate dose calculation needs to be done in the future. This will require the use of a more accurate voxel-based mouse phantom, which may be based on mouse data acquired from the X-ray CT scanner.

6.2 High-energy Prompt Gamma Ray Detection in an LSO Crystal

Various energies of prompt gamma rays are emitted and are to be detected in PGI application. The common energy range is from several keV to 11 Mev. The detection of high-energy prompt gamma rays for this purpose was studied by using currently available PET scanners, especially those that use LSO crystals. MCNP5 was used.

After the discovery of the LSO (cerium-activated lutetium orthosilicate, or Lu_2SiO_5: Ce) scintillator by Melcher and Schweitzer (1992), it quickly became the most promising crystal

in detector design for PET application, because of its high stopping power as BGO, a higher light output, and a faster decay time than BGO. The characteristics of some scintillators are listed in table 6-3. The typical size of an LSO crystal in a commercial PET scanner is 6.45mm×6.45mm×25mm in CTI Accel (Spinks et al., 2002). Most recently, a smaller sized LSO crystal has been applied in various small animals imaging PET systems to achieve a higher spatial resolution. A typical size for this kind of application is 2mm×2mm×10mm in the MicroPET (Cherry et al.,1997) system.

Table 6-3 Characteristics of Some Scintillators

	LSO	BGO	GSO	NaI
Density (g/cc)	⇒ 7.4	7.1	6.7	3.7
μ (cm−1)	0.86	⇒ 0.95	0.70	0.35
Decay Time (nsec)	⇒ 40	300	56, 600	230
Relative Light Output	75	15	25	⇒ 100
Energy Resolution	10	10	9	⇒ 8

6.2.1 Methods and Theory

For high-energy prompt gamma rays, pair production is dominant, and this process generates a pair of electrons and positrons. This means that electron transport is important in this simulation. At the same time, detection crystals are very small due to the high spatial resolution requirement. Therefore, electrons or positrons can escape these small crystals very easily while depositing only part of their energy. Under this condition, the initial directions of

electrons and positrons are important. The forward distribution of electrons or positrons can lead to more energy deposition than an isotropic distribution.

6.2.1.1 Cross-Section of Prompt Gamma Rays in LSO

The cross-sections of LSO as a function of gamma-ray energy are calculated by using XCOM (http://physics.nist.gov/PhysRefData/Xcom/Text/XCOM.html) and are shown in figure 6-2.

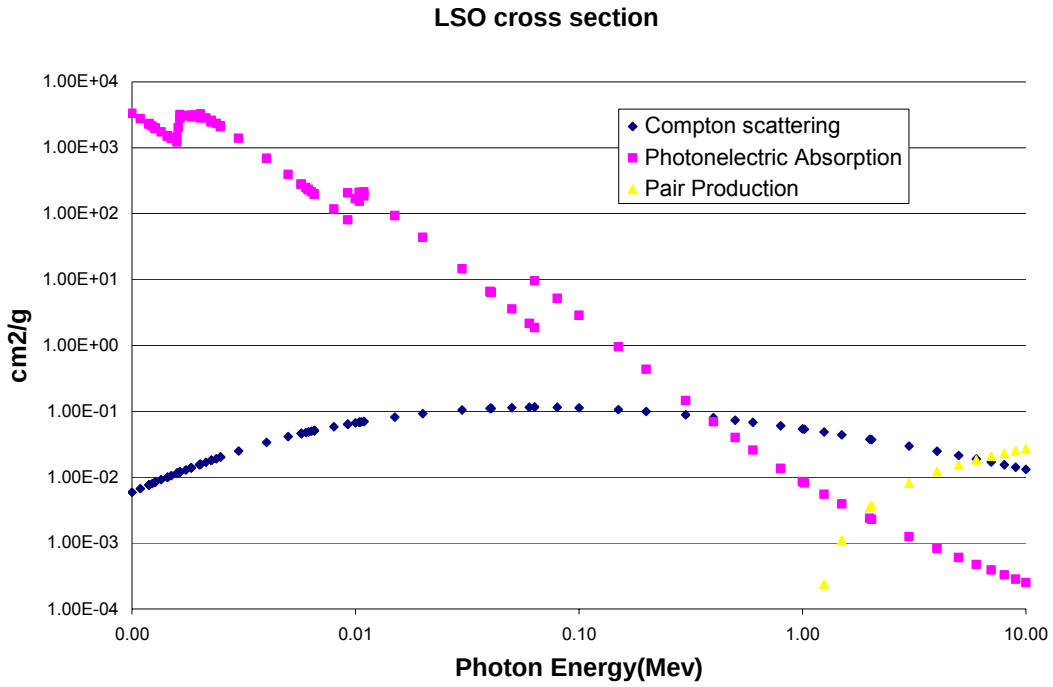

Fig. 6-2 Cross-sections of Gamma Rays for LSO

It can be seen that the photoelectric effect decreases rapidly as gamma-ray energy increases. Pair production increases rapidly as gamma-ray energy increases. At about 6Mev, the pair production cross-section will be larger than that of Compton scattering, and will be dominant for higher energy gamma rays.

6.2.1.2. Electron Range in LSO Crystals

The electron range in LSO is calculated as a function of gamma-ray energy by using EPICSHOW (http://www.llnl.gov/cullen1/epicshow.htm) and is shown in figure 6-3. From this figure, it can be seen that the order of magnitude of the electron range in LSO is almost 1mm per Mev. This is the same order or even larger than the typical LSO size for small animal applications. Therefore, it is very possible that some electrons only deposit part of their energy, and then escape the small crystals. This will decrease the counts of the photo peak, single-escape peak, and double-escape peak.

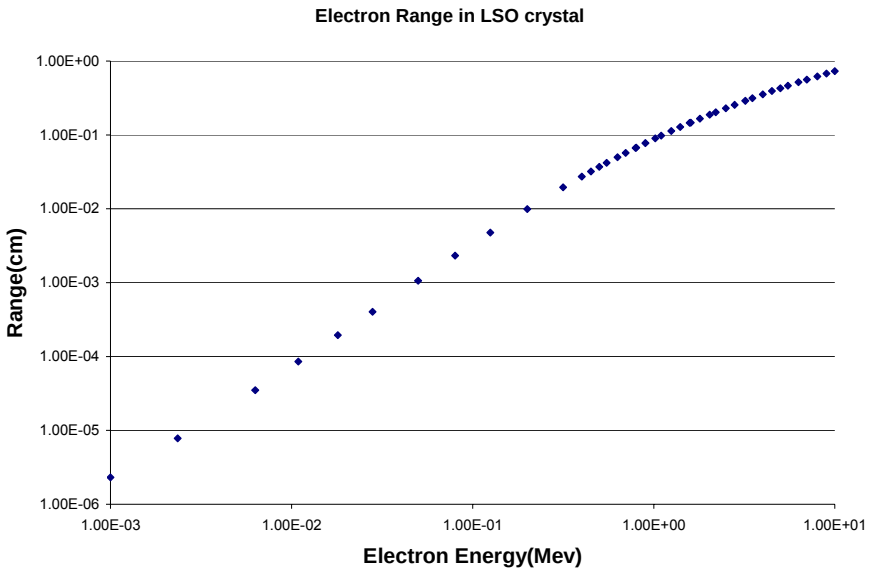

Fig. 6-3 Electron Range in LSO

6.2.1.3. Angle Distribution of Pair Production

Electron transport is very important for these small crystal detectors, and the initial directions of the electrons and positrons are also very important. It is obvious that an isotropic angular distribution of pair production electrons and positrons will lead to more

electrons escaping these small crystals while depositing only part of their energy—that is, compared to a forward distribution.

According to Evans (1955), the angular distribution of pair production electrons is a forward one, and electron and positron energies are also distributed. The MCNP5 code was tested for the pair production simulation and found to agree well with what was given in the Evans' book. The MCNP angular distribution and energy distribution are shown in figures 6-4 and 6-5.

The x axis in figure 6-4 is the polar angle between the incident direction and the direction of the produced electrons or positrons. Three gamma ray energies, 3Mev, 5Mev and 9Mev, were tried. It can be seen that the higher the energy, the more the electrons and positron will be in the forward direction and the smaller the deviation angle from the incident direction. It is an extremely forward distribution.

The x axis in figure 6-5 is the energy of the produced electrons or positions. It can be seen that the energy of the electrons and the positrons is not equal in pair production, and is controlled by a continuous distribution between 0 and total energy minus 1.02Mev. All these results agree with those in Evans' book (1955).

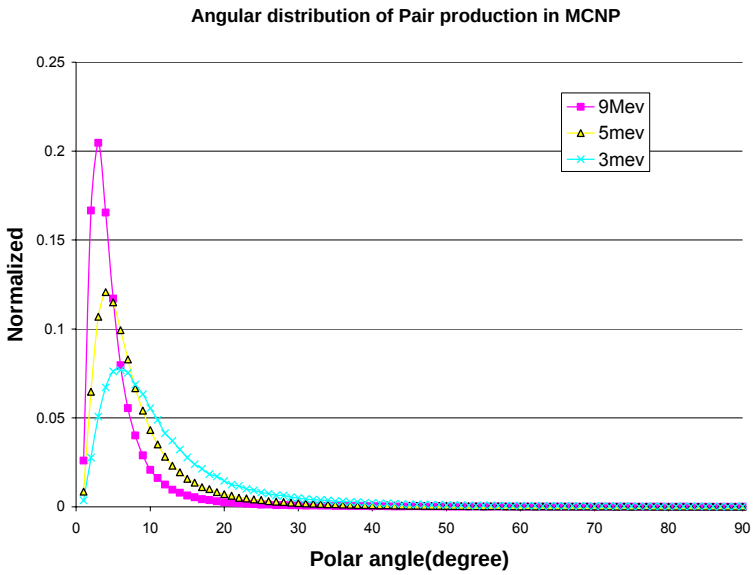

Fig. 6-4 Angle Distribution of Pair Production in MCNP

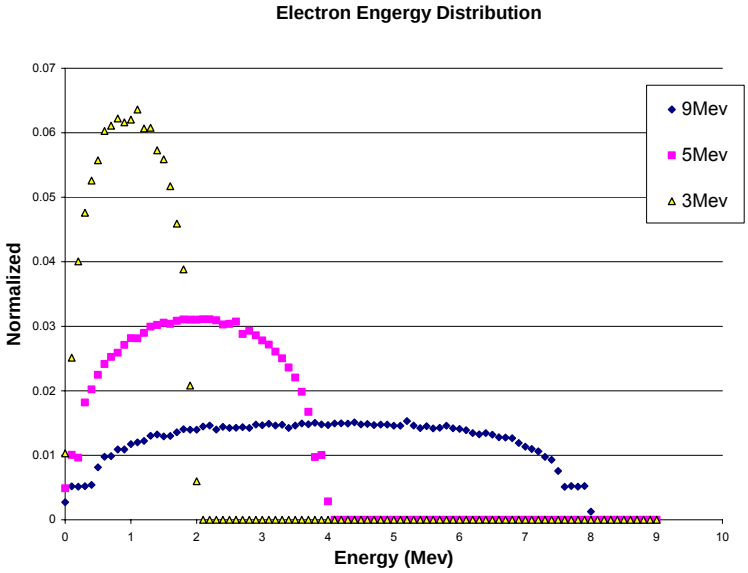

Fig. 6-5 Electron Energy Distribution of Pair Production in MCNP

6.2.2 Results

MCNP5 was used to calculate several cases. The basic simulation geometry is shown in figure 6-6.

Fig. 6-6 MCNP Simulation Geometry for LSO

Prompt gamma rays were incident from the left side of the LSO crystal, and hit the center. Various sizes of the LSO crystals were considered.

6.2.2.1. Typical Spectrum of 4-Mev Incident Prompt Gamma Rays

The incident gamma rays hit the center of the LSO crystal in the horizontal direction. The LSO crystal has dimensions: 2mm × 2mm × 10mm. The simulated spectra are shown in figure 6-7. There are two spectra. One is without electron transport while the other is with electron transport. The difference between them in the figure is mainly caused by the small size of the crystal. Some electrons only lose part of their energy and then escape from the crystal. From the figure, one can see that for high-energy gamma ray detection, the double-escape peak is the most recognizable feature.

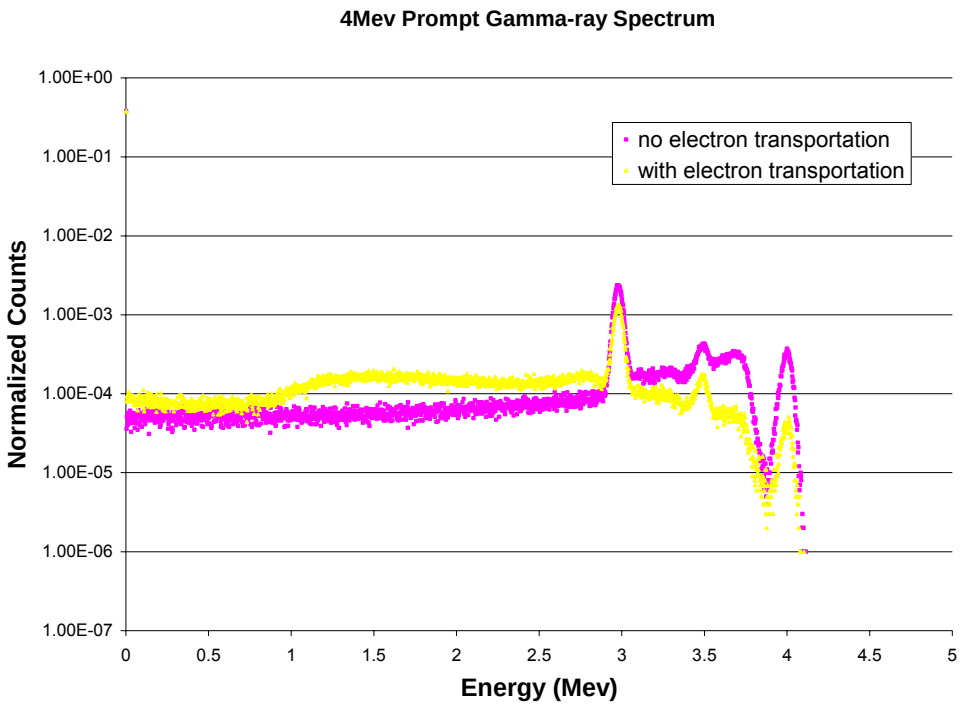

Fig. 6-7 Comparison Between With and Without Electron Transport

6.2.2.2. Comparison Between Isotropic Distribution and Forward Distribution

The isotropic angular distribution of pair production will lead to more of them losing part of their energy than the actual forward distribution. The effect is illustrated in figure 6-8. In this case, 9Mev gamma rays hit the center of the LSO crystal. The crystal size is 2mm × 2mm × 10mm.

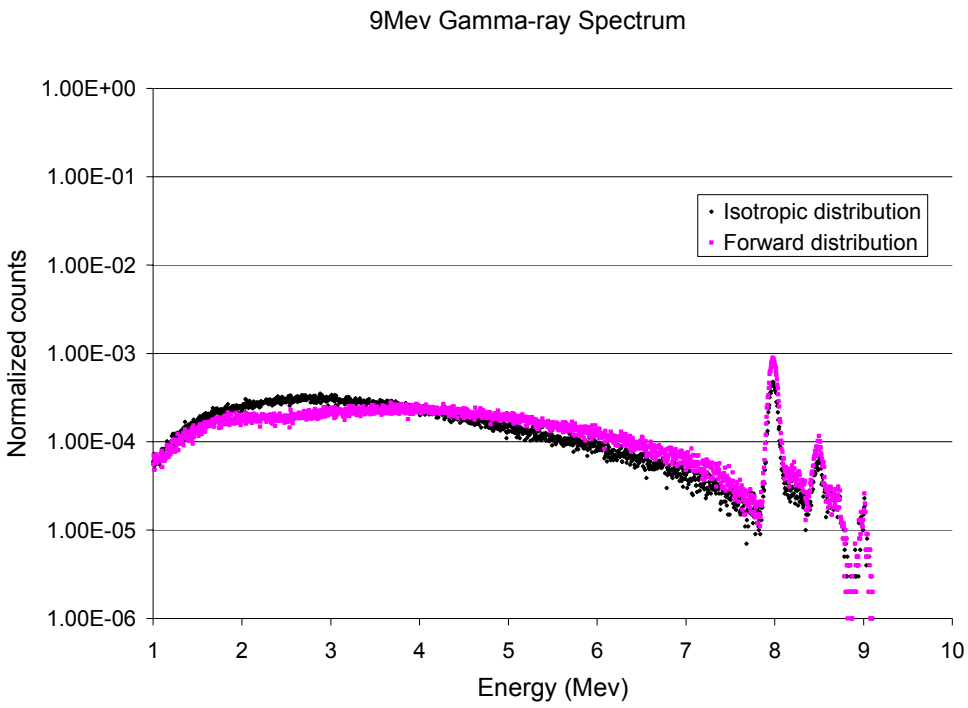

Fig. 6-8 Comparison Between Isotropic Distribution and Forward Distribution

It can be seen that the double- and single-escape peaks of the isotropic distribution case are almost 50% lower than that of the actual forward distribution.

6.2.2.3. Detection Efficiencies for Various LSO Detector Sizes

For the following cases, photo peak efficiency, single-escape efficiency, double-escape efficiency and total efficiency are calculated.

a) 2mm×2mm×10mm

For this case, the energy from 0.5Mev to 9Mev is calculated. The results are shown in figure 6-9.

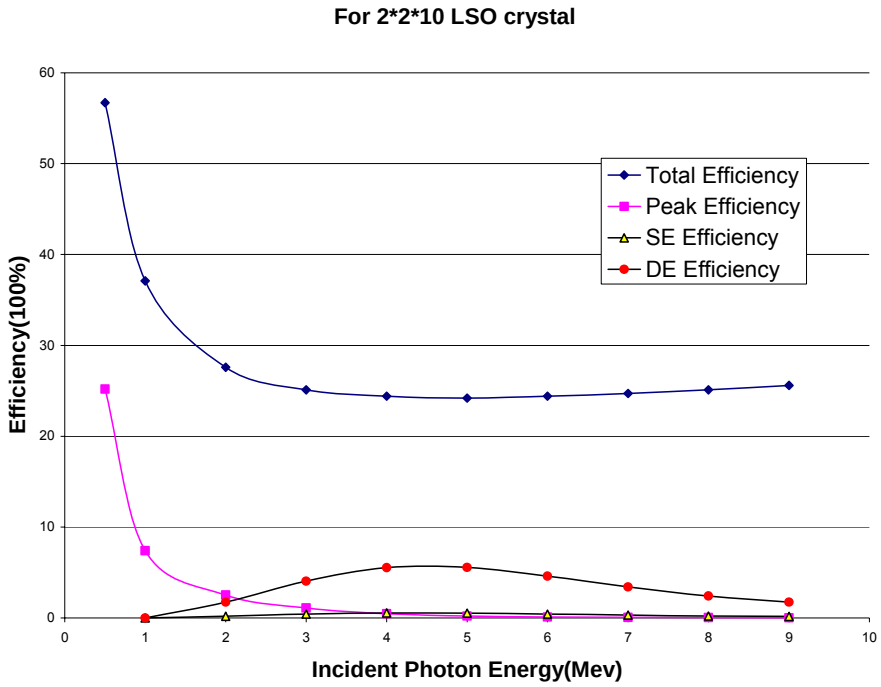

Fig. 6-9 Detection Efficiency for 2*2*10 LSO Crystal

From these results, one can see that the total efficiency decreases and then increases slightly as the energy increases. This is due to the effect of the total cross-section changing with increasing energy. The photo peak efficiency is going down continuously and is very small. Single-escape efficiency is always very small. Double-escape efficiency is relatively large and increases as energy increases. Due to the small cross-section area of the LSO crystal, the probability of both annihilation photons being detected is very small. This is the reason why photo peak efficiency and single-escape efficiency are smaller than double escape efficiency. For high-energy prompt gamma rays, the electrons produced also have a high energy. It is easy for these electrons to escape the LSO crystal and this probability increases as electron energy increases. This explains the shape of the double-escape efficiency with energy.

B) Different cross-section

The detector cross-section is changed from 2mm × 2mm to 5mm × 5mm. The length is fixed at 10mm. The results are shown in figure 6-10. Here only double-escape efficiency is displayed.

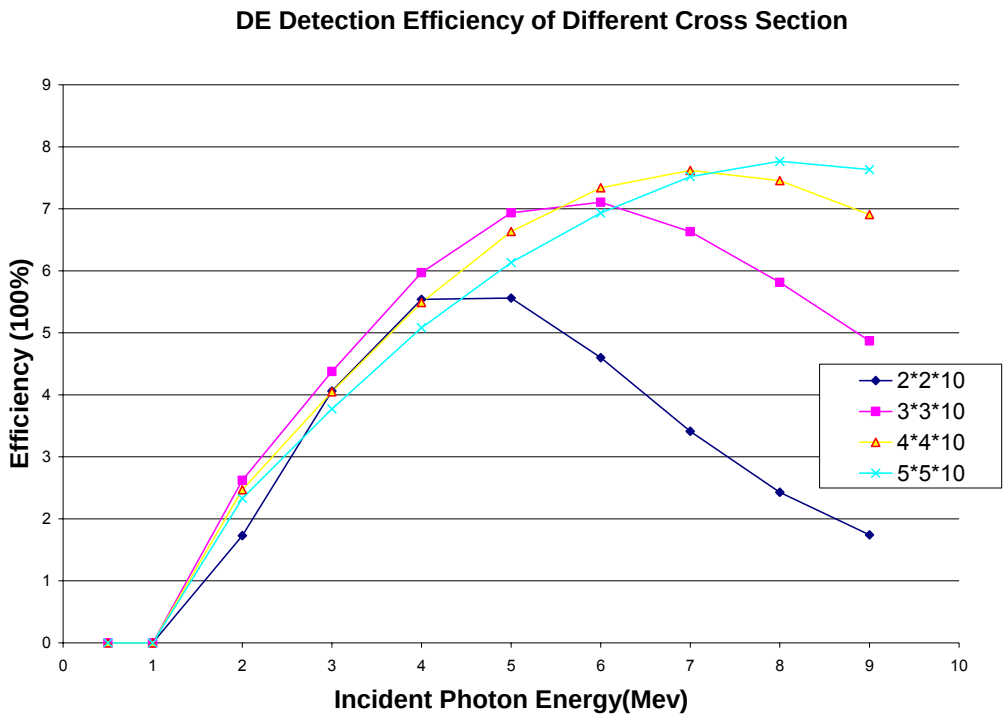

Fig. 6-10. Different Cross-Section for LSO

The double-escape efficiencies for different detector cross-sections are almost the same for the low-energy part from 1Mev to 4Mev as the energy increases, but increases at higher energies with increasing detector cross-sections. For low-energy prompt gamma rays, 2mm × 2mm is large enough for the detector to completely stop the produced electrons and positrons, but for the high-energy part, 2mm × 2mm is not large enough. As the detector cross-section increases, more and more high-energy electrons deposit all of their energy inside the crystal.

C) Different Detector Lengths

Detector lengths of 20mm and 30mm were tried. The results are shown in figures 6-11 and 6-12.

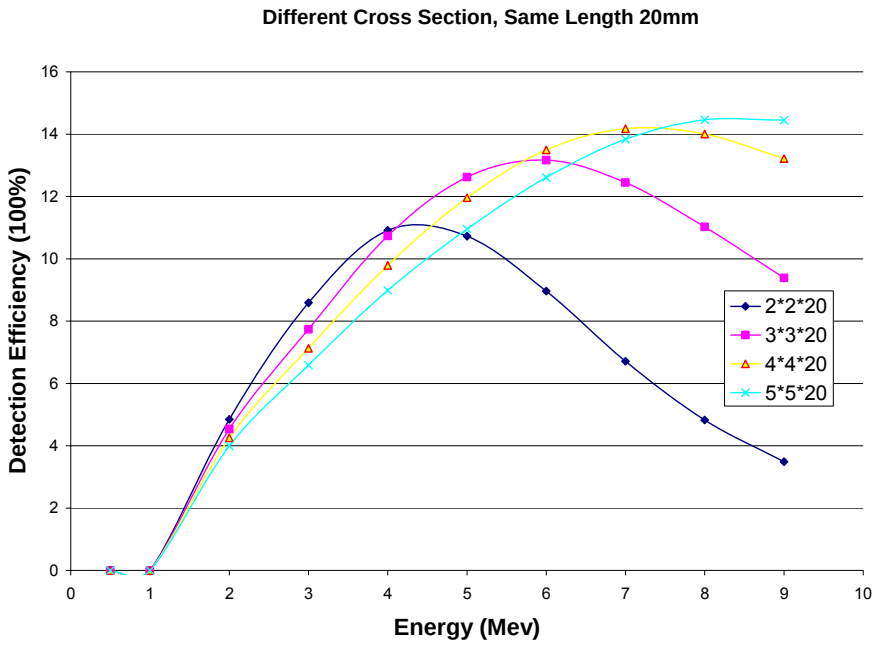

Fig. 6-11 Length=20mm for LSO

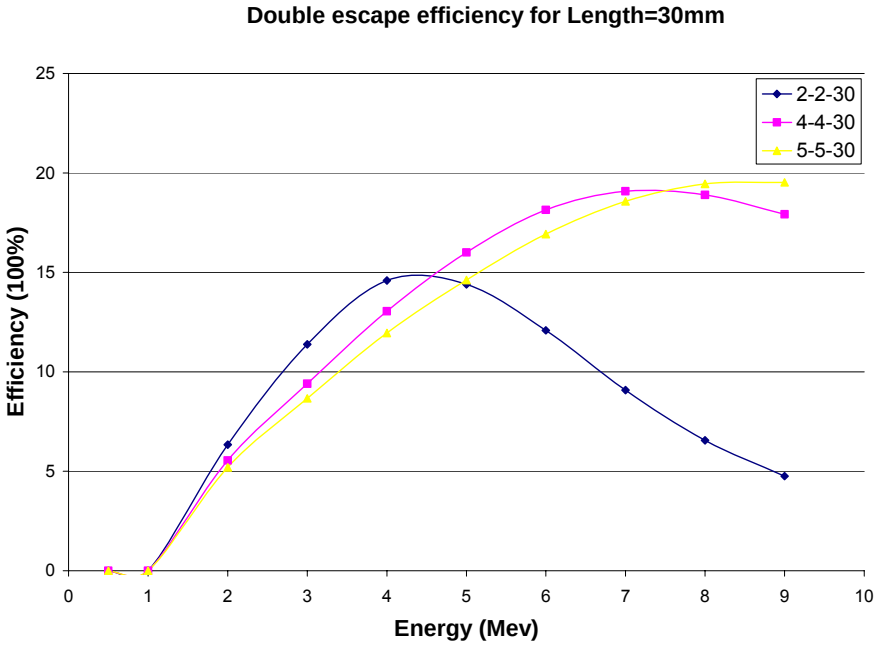

Fig. 6-12 Length=30mm for LSO

It can be seen that double-escape efficiency increases as the crystal length increases. The double-escape efficiency is about 10%-20% for energies above 3Mev for 20mm and 30mm lengths.

6.2.3 Conclusions

For high-energy prompt gamma rays, pair production is dominant. It is very likely that both annihilation 511keV photons escape the small detector without being detected; more than one is detected or both are detected. A preliminary conclusion is that detection with small LSO crystals for imaging applications is adequate for low- and high-energy gamma rays where either the photoelectric or pair production interactions dominate, but not as well for the intermediate range of gamma rays where the Compton scatter interaction dominates.

7. CONCLUSIONS AND DISCUSSIONS

The feasibility of Prompt Gamma-ray Imaging for small animals has been investigated primarily by Monte Carlo simulation.

GEANT4 was chosen as the main platform to simulate prompt gamma-ray imaging. Modifications have been applied to GEANT4 to make it capable of simulating prompt gamma rays from neutron capture reactions by following the compounds' nuclear structures. The mercury sample was irradiated by thermal neutron beams and measured with coincidence electronics setup to benchmark the simulation. The simulated sample spectrum shows good agreement with the experimental sample spectrum. This validates the idea of using Monte Carlo simulation for the feasibility study of prompt gamma-ray imaging, since the simulated sample spectra can be studied as good approximation of experimental sample spectra.

The gadolinium sample was also measured with the same experiment setup as the mercury's. Its coincidence spectrum was measured for the first time. Until now, gadolinium nuclear structure data libraries are still not complete yet. We can not simulate gadolinium prompt gamma rays by following its nuclear structure.

With simulated coincidence prompt gamma rays available, two major imaging techniques, electronic collimations and mechanic collimations, were implemented in the simulation to illustrate the feasibility of imaging elemental distribution. For electronic

collimations, several possible angular correlations were investigated, and the expectation maximization algorithm was employed to reconstruct images. Finally, the '-34' case has the most potential among the cases involving angular correlations to reconstruct images. For mechanical collimations, a pinhole, which is the most popular mechanical collimation in Micro-SPECT for small animal imaging, is utilized, and the common SPECT imaging algorithms are suggested to get images.

Neutron imaging were simulated by MCNP5, and compared with X-ray imaging. The major difference between X-ray imaging and neutron imaging is originating from the different X-rays and neutrons interactions with matter. Neutrons interact with the nuclei of the atoms, whereas X-rays interact with the electrons in the shell. The interaction probability increases as the atomic number increases for X-rays, whereas neutrons do not exhibit such systematic behavior. X-ray tomography provides a better contrast between bone and soft tissue than neutron tomography. However, neutron tomography provides better soft tissue contrast because of its higher attenuation coefficient.

The Monte Carlo simulation is used to estimate the whole body's absorbed dose for a cylindrical mouse phantom. Although the phantom is very simple, it provides an initial estimate of the radiation exposure to small animals when they are imaged with a thermal neutron beam. Under our current parameters, a $10^6/cm^2s$ flux and a 30min scan, the absorbed dose is 0.81mGy, which is caused by the body itself and an additional 0.55mGy by an additional 1% of mercury. Compared with the absorbed dose of the current PET/CT

application, we may increase the neutron flux by 100 times to get the best image quality if the different quality factors between neutrons and photons are not considered.

For high-energy prompt gamma rays, pair production is dominant. It is very likely that both annihilation 511keV photons escape the small detector without being detected; more than one is detected or both are detected. A preliminary conclusion is that detection with small LSO crystals for imaging applications is adequate for low- and high-energy gamma rays where either the photoelectric or pair production interactions dominate, but not as well for the intermediate range of gamma rays where the Compton scatter interaction dominates.

8. FUTURE WORK

Prompt gamma-ray imaging is a big project. There are still a lot of works need to be done.

Right now, GEANT4 can be used to simulate prompt gamma rays, but its speed not fast enough. GEANT4 is almost a pure analog method, and no too many variance reduction techniques there. We need to implement variance reduction techniques into GEANT4 in the future. And more benchmark experiments need to be conducted.

More efforts need to be made in nuclear data libraries, such as: completing gadolinium nuclear structure data libraries, looking for more angular correlations.

In neutron imaging, nanotube may be utilized as collimation grids and to reduce scattered neutron background.

A more detailed and accurate dose calculation needs to be done in the future. This will require the use of a more accurate voxel-based mouse phantom, which may be based on mouse data acquired from the X-ray CT scanner.

9. REFERENCES:

Adani, N. and Fallone, B. G. (2000). " Neutron imaging using medical linacs", Proceedings of the 22nd Annual EMBS Intel. Conf. Vol. 4 2457-2460, Chicago, IL,

Agostinelli, S. et al. (2003). "GEANT4- a simulation toolkit", Nucl. Instr. Meth. A. Vol. 506, pp. 250-303

Alexander, S. (2004). "Ultrafast micro-CT for in vivo small animal imaging and industrial applications," Proceedings of the SPIE, Volume 5535, pp. 733-739

Anderson, D. L. et al (1982). " Neutron-capture Prompt Gamma-ray Spectroscopy as a Quantitative Analytical Method", Neutron-capture Gamma-ray Spectroscopy and Related Topics, Inst. Phys. Ser. 62, Institute of Physics, London, 655-668

Arnold, M.L. et al (2000). "System design for in vivo neutron activation analysis measurements of manganese in the human brain: based on Monte Carlo modeling." Appl. Radiat. Isot. 53, 651-656

Balogun, F. A., Spyrou, N. M., and Adesanmi (1996), C. A. "Neutron induced gamma-ray emission tomography," Nuclear Instruments and Methods in Physics Research B 114, 387-393

Barker, H. B. and Maier, M. R. (2005). "The STING imaging system based on using neutrons and gammas." Nuclear Instruments and Methods in Physics Research A 542, 288-289

Barth, R. F. et al. (2005). " Boron Neutron Capture Therapy of Cancer: Current Status and Future Prospects." Clinical Cancer Research, Vol. 11, pp. 3987-4002, Jun. 1 2005

Bayon Guy (2005). "Present applications of neutron radiography in France." Nucl. Instru. Meth. A, Vol. 424, 92-97

Beddoe, A. H. et al. (1987) "Measurement of total body chlorine by prompt gamma in vivo neutron activation analysis." Phys. Med. Biol. 32, 191-201

Benveniste, H. (2000). "Magnetic resonance microscopy of the C57BL mouse brain." NeutoImage 11, 601-611

Biggin, H.C. et al (1972). "Determination of nitrogen in living patients." Nature New Biol. 236, 187-188

Bozkurt, A. Chao, T. C. and Xu, X. G. 2000, "Fluence-to-dose conversion coefficients from monoenergetic neutrons below 20Mev based on the VIP-Man anatomical model", Phys. Med. Biol. 45 3059-3079.

Byun, S.H. et al (2005). “In vivo measurement of bone aluminium: Recent developments.” Journal of Inorganic Biochemistry 99, 1899-1903

Cesca, N. et al. (2004). “ A triple modality device for simultaneous small animal CT and PET-SPECT imaging.” Nuclear Science Symposium conference record, 6, 3472-3474

Chang, L.T. et al. (1974). “ A method of tomographic imaging using a multiple-pinhole coded aperture.” J. Nucl. Med. 15, 1063-1065

Cherry, S. R. and Shao, Y. (1997). “MicroPET: a high resolution PET scanner for imaging small animals,” IEEE Trans, Nucl. Sci., 44,1161-1166

Chettle, D.R. and Fremlin, J.H. (1984). “ Techniques of in vivo neutron activation analysis.” Phys. Med. Biol. 29, 1011-1043

Cho, Z. H. (2005). “PET-MRI hybrid imaging scanner – an emerging new tool for molecular neuroimaging.” Enterprise networking and Computing in healthcare industry, Proceedings of 7th international workshop. 5

Chow, P.L., A.L. Goertzen, F. Berger, J.J. DeMarco, A.F. Chatziioannou, 2001, “Monte Carlo model for estimation of dose delivered to small animals during 3D high resolution X-ray computed tomography“, Nuclear Science Symposium Conference Record, 2001 IEEE, Nov. 2001, Vol. 3, 1678-1681.

Coderre, J. A. and Morris, G. M. 1999. “The radiation biology of boron neutron capture therapy” Radiat. Res. 151 1-18

Denison, C., Carlson, W. D., and Ketcham, R. A. (2002). “Three-dimensional quantitative textural analysis of metamorphic rocks using high-resolution computed X-ray tomography: part I:methods and techniques,” J. Metamorph. Geol., vol. 15, pp. 29-44

Eriksson, L. et al. (2002). “ NEMA count-rate evaluation of the first and second generation of the Ecat Exact and Ecat Exact HR family of scanners”. Nucl. Sci. IEEE Trans. Vol. 49, 640-643

Evans, H. J. et al. (1979). “Facility for regional in vivo neutron activation analysis of skeletal calcium”, Phys. Med. Biol. 24, 181-187

Evans, R. D. (1955). The Atomic Nucleus, McGRAW-Hill Book Company, London.

Faw, R. E. and Shultis, J. K. 1999, Radiological Assessment: Sources and Doses, P622.

Foster, F.S. (2000). “Advances in ultrasound biomicroscopy.” Ultrasound Bio. Med. 26, 1-27

Franklin, D.M. et al. (1990). “An improved in vivo neutron activation system for measuring kidney cadmium.” Phys. Med. Biol. 35, 1397-1408

Gardner, R. P. and Xu, L. (2004), "Prompt Gamma-Ray Imaging for Small Animals," ISBI, 1373-1376

Gardner, R. P., Mayo, C. W., El-Sayyed, E. S., Metwally, Zheng, W. A., Y. and Poezart, M., A feasibility study of a coincidence counting approach for PGNAA applications, Applied Radiation and Isotopes, Volume 53, Issues 4-5, 15 November 2000, Pages 515-526

Gehrke, S. and Wirth, M. (2005). "Application of Conventional and Dual-Energy X-Ray tomography in Process Engineering," IEEE Sensor J. Vol. 5, No. 2, pp.183-187.

Gladney, E. S. et al (1979), A Literature Survey of Chemical Analysis by Thermal Neutron-induced Capture Gamma-ray Spectroscopy, Los Alamos Scientific Laboratory Report LA-8023-MS

Glascock, M. D. (1984) A Literature Survey of Elemental Analysis by Neutron-induced Prompt Gamma-ray Spectroscopy and Related Topics, University of Missouri Report, Columbia.

Genant, H.K. (1999). "Advanced imaging of bone macro and micro structure." Bone 25, 149-152

Graichen, H. (1998). "A non-destructive technique for 3-D microstructral phenotypic characterization of bones in genetically altered mice: preliminary data in growth hormone transgenic animals and normal controls." Anat. Embryol. 199. 239-248.

Greenwood, R. C. (1979), " Practical Applications of Neutron Capture Gamma Rays", Proc. Third Int. Sysp. Neutron-capture Gamma-ray Spectroscopy and Ralated Topics, Plenum, New York, 441-460

Grinyer, J., Byun, S.H., and Chettle, D.R. (2005), "In vivo prompt gamma neutron activation analysis of cadmium in the kidney and liver." Appl. Radiat. Isot. 63, 475-479

Guerra, A. D. et al. (2003). "A dedicated system for breast cancer study with combined SPECT-CT modalities." Nucl. Instru. Meth. A. 497, 129-134

Han, X. G. (2005), "Development of Monte Carlo Code for Coincidence Prompt Gamma-ray Neutron Activation analysis", Ph.D thesis, North Carolina State University.

Hipp, J.A. (1996). "Trabecular bone morphology from micro magnetic resonance imaging." J. Bone Miner. Res. 11, 286-297

Hiriyannaiah, H. P. (1997). "X-ray computed tomography for medical imaging," Signal Processing Magazine, IEEE, Vol. 14, Issue 2, pp. 42-59.

ICRU, FOUR-COMPONENT, http://physics.nist.gov/cgi-bin/Star/compos.pl?matno=262

Jacobs, P., Sevens, E., and Kunnen, M. (1995). ”Principles of computerized X-ray tomography and applications to building materials,” Sci. of The Total Env. Vol. 167, Issues 1-3, pp. 161-170

Jaszczak, R. J. et al. (1994). “Pinhole collimation for ultra-high-resolution, small-field-of-view SPECT.” Phys. Med. Biol. 39, 425-437

Johnson, G.A., and Turnbull, D.H. (1999). “In Vivo Microscopy: Technologies and Applications” A workshop for small animal imaging.

Kardjilov, N. et al. (2005). “Industrial applications at the new cold neutron radiography and tomography facility of the HMI.” Nucl. Instru. Meth. A. Vol. 542, 16-21

Knoll, G. F. (1999). Radiation Detection and Measurement,

Kontaxakis, G. (1996). “Maximum Likelihood Image Reconstruction in Positron Emission Tomography: Convergence Characteristic and Stopping Rules,” PH.D. Thesis, Rutgers, the State University of New Jersey

Kornblum, H.I. (2000). “In vivo imaging of neuronal activation and plasticity in the rat brain by high resolution positron emission tomography (microPET).” Nat. Biotechnol. 18, 655-660

Lindstrom, R. M. et al (1994). “ Analytical Applications of Cold Neutron Capture and Opportunities for Nuclear Physics”, Capture Gamma-ray Spectroscopy and Related Topics, World Scientific, Singapore, 955-961

Lindstrom, R. M. et al (1997). “ Analytical Applications of Neutron Capture Gamma Rays”, Proc. 9th Int. Capture Gamma-ray Spectroscopy and Related Topics, Springer, Budapest, 693-704

Locher, G. L. (1936). “Biological effects and therapeutic possibility of neutrons”, Am. J. Roentgenol. Radium ther. 36, 1-13.

Los Alamos National Laboratory, Monte Carlo N-Particle code(MCNP) http://mcnp-green.lanl.gov/index.html

Ma, R. et al (1998). “Total Body Chlorine: Calibration of the In vivo Neutron Activation Measurement.” Appl. Radiat. Isot. 49, 533-535

MacDonald, L. R. et al. (2001). “Pinhole SPECT of Mice Using the LumaGEM Gamma Camera.” IEEE Trans. Nucl. Sci. Vol. 48, No. 3

Metwally, W. A., Gardner, R. P. and Mayo, C. W., Two-dimensional diagonal summing of coincidence spectra for bulk PGNAA applications , Nuclear Instruments and Methods in Physics Research Section A: Accelerators, Spectrometers, Detectors and Associated Equipment, Volume 525, Issue 3, 11 June 2004, Pages 511-517

Metwally, Walid A., Gardner, Robin P. and Mayo, Charles W., Elemental PGNAA analysis using gamma-gamma coincidence counting with the library leastsquares approach, Nuclear Instruments and Methods in Physics Research Section B: Beam Interactions with Materials and Atoms, Volume 213, January 2004, Pages 394-399

Metwally, Walid A., Gardner, Robin P., Mayo, Charles W., Elemental PGNAA analysis using gamma-gamma coincidence counting with the library leastsquares approach, Nucl. Instru. Methods, B, In press, 2004

Metwally, Walid A., Gardner, Robin. P., Mayo, Charles W., Elemental PGNAA analysis using gamma-gamma coincidence counting with the library leastsquares approach. Nuclear Instrument and Methods in Physics Research B 213 (2004) 394-399.

Mishima, K. et al. (1999). "The review of the application of neutron radiography to thermal hydraulic research." Nucl. Instr. Meth. A. Vol. 424, 66-72

Mitra, S. et al. (1993). "In vivo measurement of total body chlorine using the 8.57Mev prompt de-excitation following thermal neutron capture." Phys. Med. Biol. 38, 161-172

Melcher, C. L. and Schweitzer, J. S. (1992). "Cerium-doped Lutetium Oxyorthosilicate: A fast, efficient new scintillator," IEEE Trans, Nucl. Sci., vol. 39, pp. 502-505

Montero, A. (2000). "Disruption of the fibroblst growth factor-2 gene results in decreased bone mass and bone formation." J. Clin. Invest. 105. 1085-1093

Nicoll, J. J. et al. (1987) " In vivo precision of total body calcium and sodium measurements by neutron activation analysis." Phys. Med. Biol. 32, 243-246

Lange, K. et al. (1987). "A Theoretical Study of Some Maximum Likelihood Algorithm for Emission and Transmission Tomography", IEEE Transaction Medical Imaging, 6(2): 106-114

Lerman, A. and Ritman, E.L. (1999). "Evaluation of microvascular anatomy by micro-CT." Herz 24, 531-533

Locher, G.L., 1936, "Biological effects and therapeutic possibility of neutrons", Am. J. Roentgenol. Radium ther. 36, 1-13.

O'Meara, J.M. et al (2001). " The feasibility of accelerator-based in vivo neutron activation analysis of nitrogen." App. Rad. Iso. 55,767-774

Paul, D.A. and Hank, F.K. (2003). " Small animal imaging with high resolution single photon emission tomography." Nucl. Med. Bio. 30, 889-895

Paul, R. L. et al (2000). " Prompt Gamma-ray Activation Analysis: Fundamental and Applications", J. Radioanal. Nucl. Chem. 243, 181-189

Pietrzyk, U. et al. (1996). " Clinical applications of registration and fusion of multimodality brain images from PET, SPECT, CT, and MRI." European Journal of Radiology 21, 174-182

Shaw, D. M. (1999). "Prompt Gamma Neutron Activation Analysis", J. Neutron Res. 7, 181-194

Shepp, L. A. and Vardi, Y. (1982). "Maximum Likelihood Reconstruction for Emission Tomography", IEEE Transactions on medical imaging, vol. MI-1, NO. 2, pp. 113-122

Shyu, C. M., Gardner, R. P., and Verghese, K. (1993), "Development of the Monte Carlo Library Least-Squares Method of Analysis for Neutron Capture Prompt Gamma Ray Analyzers." International Journal of Radiation Applications and Instrumentation. Part E, Nuclear Geophysics, 7(2), pp. 241-267

Smith, M. F. et al. (2003). "Optimizing Pinhole and Parallel Hole Collimation for Scintimammography With Compact Pixellated Detectors." IEEE Transactions on nuclear science, Vol. 50, No. 3, pp. 321-326

Spinks, T. J. and Bloomfield, P. M. (2002). "A comparison of count rate performance for ^{125}O blood flow studies in the CTI HR+ and Accel tomographs in 3D mode" IEEE, Nucl. Sci. Symp. Conf. 3, 1457-1460

Strul D, Santin G, Lazaro D, Breton V, Morel C. GATE (Geant4 Application for Tomographic Emission): a PET/SPECT general-purpose simulation platform. Nucl. Phys. B (Proc. Suppl.) 125 (2003) 75-79

Sutcliffe, J. F. et al. (1990). "In vivo measurement of total body carbon using 238Pu/Be neutron sources." Phys. Med. Biol. 35, 1089-1098

Tal, C. (2001). "Performance evaluation of the microPET P4: a PET system dedicated to animal imaging." Phys. Med. Biol. 46, 1845-1862

Turnbull, D.H. (1999). " In utero ultrasound backscatter microscopy of early stage mouse embryos." Computerized Med. Imaging Graphics 23, 25-31

Verbakel, W. F. A. R. et al (1997). "A r-ray telescope for on-line measurements of low boron concentrations in a head phantom for BNCT." Nuclear Instruments and Methods in Physics Research A 394, 163-172

Verbakel, W. F. A. R. et al. (2001). "Validation of the scanning r-ray telescope for in vivo dosimetry and boron measurements during BNCT." Phys. Med. Biol. 46, 3269-3285

Verbakel, W. F. A. R. et al. (2002). “Towards in vivo monitoring of neutron distributions for quality control of BNCT.” Phys. Med. Biol. 47, 1059-1072

Vontobel, P., Lehmann, W., and Carlson, W. D. (2000). “Comparison of X-ray and Neutron Tomography Investigations of Geological Materials,” IEEE Trans. Nucl. Sci. Vol. 42, No. 1

Wechalekar, K. et al. (2005). “PET/CT in oncology-a major advance.” Clinical Radiology 60, 1143-1155

Wehrli, F.W. (1998). “ New architectural parameters derived from micro-MRI for the prediction of trabecular bone strength.” Technol. Health Care 6, 307-320

Weisenberger, A. G. et al. (2003). “ SPECT-CT system for small animal imaging.” Nuclear Science, IEEE transactions 50, 74-79

Winkler, B., Knorr, K., Kahle, A., Vontobel, P., Lehmann, E., Hennion, B., and Bayon, G. (2002). “Neutron imaging and neutron tomography as nondestructive tools to study bulk-rock samples,” Eur. J. Mineral., vol. 14, pp. 349-354

Xia, Y. (1994). “Diffusion and relaxation mapping of cartilage bone plugs and ecised disks using microscopic magnetic resonance imaging.” Magn. Reson. Med. 31, 273-282